Vysoké učení technické v Brně
Brno University of Technology

Fakulta strojního inženýrství
Ústav konstruování / Odbor tribologie

Faculty of Mechanical Engineering
Institute of Machine and Industrial Design / Department of Tribology

Effects of non-Newtonian lubricants on surface roughness in point contacts

[Dizertační práce]
[PhD Thesis]

Autor práce: **Ing. Ildikó Ficza**
Author

Vedoucí práce: **prof. Ing. Martin Hartl, Ph.D.**
Supervisor

Brno 2015

ústav konstruování

STATEMENT

I hereby declare that I have written the PhD thesis *Effects of non-Newtonian lubricants on surface roughness in point contacts* on my own according to advice of my supervisor prof. Ing. Martin Hartl, Ph.D., and using the sources listed in references.

Brno, 01. 04. 2015

.....
Ildikó Ficza

BIBLIOGRAPHICAL REFERENCE

FICZA, I. *Effects of non-Newtonian lubricants on surface roughness in point contacts.* Brno, 2015. 154 p. PhD thesis. Brno University of Technology, Faculty of Mechanical Engineering, Institute of Machine and Industrial Design. Supervisor: prof. Ing. Martin Hartl, Ph.D.

ACKNOWLEDGEMENT

I would like to express my gratitude to my supervisor prof. Ing. Martin Hartl, Ph.D. for his advice during my PhD studies. Furthermore, I would like to express my gratitude to Ing. Petr Šperka, Ph.D. for his advice, useful comments and remarks, and for providing experimental results. I would like to thank my family and my close ones as well as my collegues who have supported me throughout my studies.

ABSTRACT

This PhD thesis focuses on the study of roughness deformation inside an elasto-hydrodynamically lubricated point contact. The passage of the roughness feature through the contact zone is modeled using numerical techniques. A single transverse ridge is assumed in the transient EHL model which presents a complex problem with a second order partial differential equation an integro-differential equation. Non-Newtonian fluid behavior is assumed in the model which further increases its complexity. In order to solve the system of equations the multigrid techniques are applied. The thesis contains the mathematical model describing the problem and a detailed description of the multigrid method. The results obtained by the simulations are compared to experimentally evaluated film thickness values. The roughness deformation is observed for a wide range of operating conditions as well as for different lubricant parameters. The effect of these lubricant parameters on the deformation is studied as well.

KEYWORDS:

tribology, elastohydrodynamic lubrication, EHL, numerical simulation, multigrid method, surface roughness, roughness deformation, non-Newtonian lubricants

ABSTRAKT

Tato dizertační práce je zaměřena na studium deformace nerovnosti uvnitř elastohydrodynamicky mazaného (EHD) kruhového kontaktu. Práce se zabývá studiem přechodu příčné nerovnosti přes kontaktní oblast, která je modelována pomocí numerických metod. Model dále uvažuje nenewtonské chování maziva. Použitý matematický model se skládá z parciální diferenciální rovnice druhého řádu pro řešení tlaku a integro-diferenciální rovnice pro řešení elastických deformací. Pro řešení tohoto modelu je použitá takzvaná multigrid (vícesíťová) metoda. Práce obsahuje popis matematického modelu EHD kontaktu a aplikované numeriké metody. Výsledky simulací jsou porovnány s experimentálně stanovenýma hodnotama tloušťky mazacího filmu. Deformace nerovnosti uvnitř kontaktní oblasti je studována pro různé provozní podmínky (střední rychlost, poměr proklzu) a různá vlastnosti maziva.

KLÍČOVÁ SLOVA:

tribologie, elastohydrodynamické mazání, EHD, numerická simulace, multigrid metoda, povrchové nerovnosti, deformace nerovností, nenewtonské chování maziva

CONTENTS

1 INTRODUCTION

Mathematical and numerical modeling of different physical processes forms an important part of every technical discipline. Tribology is not an exception. It is defined as the field of science studying friction, wear and lubrication of interacting surfaces in relative motion. The practical objective of tribology is to control wear and friction, while lubrication is an effective way to control wear and reduce friction [1]. We can distinguish between hydrodynamic, elastohydrodynamic, mixed and boundary lubrication.

Elastohydrodynamic lubrication (EHL) can be defined as a form of hydrodynamic lubrication where the elastic deformations of the contacting bodies and the changes of viscosity with pressure play fundamental roles [1]. EHL is mainly typical for non-conforming contacts of machine elements - rolling bearings, gears, cams and many others. The two main characteristics of the EHL problem, the elastic deformations and the piezo-viscous effects, create a complex problem requiring a detailed numerical solution.

Theoretical study of hydrodynamic lubrication goes back until 1886, when Osborne Reynolds [2] derived the equation describing the fluid flow in a narrow gap which was named later after Reynolds himself. From this moment, the research done in the area of hydrodynamic and elastohydrodynamic lubrication went on and several discoveries were done by different authors. Huge amount of research was done, both in theoretical and experimental fields. Although, the first numerical solutions used many assumptions, their importance could not be questioned. Modeling and simulations serve as tools for prediction or comparison with experimental observations.

The fast progress in computation techniques of the last decades enabled the detailed study of the EHL problem. The first numerical works focused on the basic parameters such as pressure and film thickness distribution in the contact. They had to work with many simplifying assumptions such as smooth surfaces or Newtonian lubricant flow. Due to the advances done in the area of numerical methods many of these simplifying assumptions can be omitted in today's models. The most of the recent numerical techniques are stable and accurate enabling to solve more complicated models, such as the passage of rough surfaces through the contact or thermal problems.

In a typical EHL contact, such as cams, rolling bearings, etc., the increasing performance and operating life results in decreasing lubricant film thickness. The scale of the film thickness in such contacts requires to consider the roughness components of the surfaces. The significance of their effect on the basic EHL parameters can not be neglected. The study of the roughness behavior inside an EHL contact is essential for the design, maintenance and life prediction of any machine element and it is closely related to stress prediction, contact fatigue, etc. This fact resulted in many published experimental and numerical works observing the behavior of rough surfaces in an EHL contact. Roughness can be incorporated into numerical models by assuming real or artificial surface features. While real roughness is hard to model, studies dealing with artificial roughness are more widespread. Different rapid prediction tools for the evaluation of roughness deformation were presented, but their

applicability is limited, and therefore full numerical solutions are required as well.

For many years, the numerical models assumed Newtonian fluid flow, however, compared to experiments it was revealed that this assumption is quite inaccurate. The dependence between the shear rate and shear stresses of a lubricant is not linear, especially when the contacting bodies operate under rolling-sliding conditions. There are several published non-Newtonian models among which the Ree-Eyring model became the most applied in the simulations for point contacts. Another examples are the generalized Newtonian model, or the limiting shear stress concept proposed by Bair and Winer. The drawback of these models is that they are mostly applicable for the line contact problems.

The current thesis aims to study the effect of non-Newtonian lubricant properties on the behavior of surface roughness inside the contact zone under rolling-sliding conditions. The main question to be addressed is that how the roughness inside a highly loaded EHL point contact behaves and which parameters control its behavior. Since this problem is non-linear and the inclusion of the roughness feature requires time-dependent solution, an accurate and stable numerical algorithm has to be developed.

2 STATE OF THE ART

The history of theoretical EHL goes back until the 19th century, when in 1886 Reynolds [2] derived from the Navier-Stokes equations and from the continuity equation the equation describing the fluid flow in a narrow gap assuming Newtonian viscous flow. His work formed the basis for hydrodynamic lubrication and confirmed Tower's experiments [3]. Later in 1916, Martin [4] and Gümbel [5] applied the Reynolds equation to non-conformal surfaces. Assuming this type of contacting bodies the elastic deformations of the surfaces can not be neglected. Grubin [6] was the first to include these deformations into his solution in 1949. Moreover, he assumed that the viscosity of the lubricant is pressure-dependent. In 1951 Petrusevich [7] published the first analytical-numerical solution of EHL confirming Grubin's assumptions. Later on, advances in computer techniques enabled full numerical solutions of the problem.

2.1 Governing equations

The EHL problem is governed by a complex set of equations. The basic mathematical model of the EHL problem is based on different simplifying assumptions which were summarized by Gohar [8]:

- body forces are negligible,
- pressure is constant through the lubricant film (z direction),
- no slip at the boundary surfaces,
- the lubricant flow is laminar (low Reynolds number),
- inertia and surface tension forces are negligible compared with viscous forces,
- shear stress and velocity gradients are only significant across the lubricant film (z direction),
- the lubricant is Newtonian,
- the lubricant viscosity is constant across the film (z direction),
- the lubricant boundary surfaces are parallel or at a small angle with respect to each other.

With these assumptions in mind the main equations necessary to describe the isothermal circular EHL problem - the Reynolds equation, the film thickness equation and the force balance equation - will be presented. Because of the high pressures in the lubricant film the variation of the lubricant properties (the density and the viscosity) with pressure have to be considered.

2.1.1 Reynolds equation

Assuming a narrow gap and a Newtonian lubricant behavior the Reynolds equation can be derived from the Navier-Stokes equations and the mass conservation equation.

The Navier-Stokes equation has the following form

$$\rho\frac{D\mathbf{U}}{Dt} = \rho\mathbf{F} - \nabla p - \frac{2}{3}\nabla\left[\eta\nabla\cdot\mathbf{U}\right] + 2\left[\nabla\cdot\left(\eta\nabla\right)\right]\mathbf{U} + \nabla\times\left[\eta\left(\nabla\times\mathbf{U}\right)\right] \tag{2.1}$$

with the hydrostatic pressure p, viscosity η, the velocity vector $\mathbf{U}$, density ρ and the external force field $\mathbf{F}$. Since the effect of the external forces, the inertia and surface tension forces are assumed to be negligible Equation (2.1) is reduced to

$$\nabla p = -\frac{2}{3}\nabla\left[\eta\nabla\cdot\mathbf{U}\right] + 2\left[\nabla\cdot\left(\eta\nabla\right)\right]\mathbf{U} + \nabla\times\left[\eta\left(\nabla\times\mathbf{U}\right)\right] \tag{2.2}$$

which can be expressed for the x, y and z direction of Cartesian system as

$$\begin{aligned}
\frac{\partial p}{\partial x} &= \frac{\partial}{\partial x}\left(\frac{4}{3}\eta\frac{\partial u}{\partial x} - \frac{2}{3}\eta\left(\frac{\partial v}{\partial y} + \frac{\partial w}{\partial z}\right)\right) + \frac{\partial}{\partial y}\left(\eta\frac{\partial u}{\partial y} + \eta\frac{\partial v}{\partial x}\right) + \frac{\partial}{\partial z}\left(\eta\frac{\partial u}{\partial z} + \eta\frac{\partial w}{\partial x}\right)\\
\frac{\partial p}{\partial y} &= \frac{\partial}{\partial x}\left(\eta\frac{\partial v}{\partial x} + \eta\frac{\partial u}{\partial y}\right) + \frac{\partial}{\partial y}\left(\frac{4}{3}\eta\frac{\partial v}{\partial y} - \frac{2}{3}\eta\left(\frac{\partial u}{\partial x} + \frac{\partial w}{\partial z}\right)\right) + \frac{\partial}{\partial z}\left(\eta\frac{\partial v}{\partial z} + \eta\frac{\partial w}{\partial y}\right)\\
\frac{\partial p}{\partial z} &= \frac{\partial}{\partial x}\left(\eta\frac{\partial w}{\partial x} + \eta\frac{\partial u}{\partial z}\right) + \frac{\partial}{\partial y}\left(\eta\frac{\partial w}{\partial y} + \eta\frac{\partial v}{\partial z}\right) + \frac{\partial}{\partial z}\left(\frac{4}{3}\eta\frac{\partial w}{\partial z} - \frac{2}{3}\eta\left(\frac{\partial u}{\partial x} + \frac{\partial v}{\partial y}\right)\right)
\end{aligned} \tag{2.3}$$

where u, v and w are the fluid velocities in x, y and z direction respectively. The assumption that in the most lubrication problems the gap is narrow simplifies Equations (2.3), i.e. if h is the characteristic size in the z direction and L in the x and y directions, it holds that $h/L << 1$ and hence all derivatives with respect to x and y will be much smaller than their equivalents in the z direction [9]

$$\begin{aligned}
\frac{\partial p}{\partial x} &= \frac{\partial}{\partial z}\left(\eta\frac{\partial u}{\partial z}\right)\\
\frac{\partial p}{\partial y} &= \frac{\partial}{\partial z}\left(\eta\frac{\partial v}{\partial z}\right)\\
\frac{\partial p}{\partial z} &= 0
\end{aligned} \tag{2.4}$$

We assume boundary conditions $\mathbf{U}_{z=z_1} = \mathbf{U}_1$ and $\mathbf{U}_{z=z_2} = \mathbf{U}_2$ which say that no slip occurs at the surfaces. As a result of the narrow gap, the pressure p is independent of z. Integrating Equations (2.4) and using the boundary conditions at $z = z_1$ and $z = z_2$ we obtain expressions for the velocities u and v

$$\begin{aligned}
u &= \frac{1}{2\eta}\frac{\partial p}{\partial x}\left(z^2 - \left(z_1 + z_2\right)z + z_1 z_2\right) + \frac{u_2 - u_1}{z_2 - z_1}\left(z - z_1\right) + u_1\\
v &= \frac{1}{2\eta}\frac{\partial p}{\partial y}\left(z^2 - \left(z_1 + z_2\right)z + z_1 z_2\right) + \frac{v_2 - v_1}{z_2 - z_1}\left(z - z_1\right) + v_1
\end{aligned} \tag{2.5}$$

Let $z' = z - z_1$, i.e. $0 \le z' \le h$, where $h = z_2 - z_1$ is the gap width, then

$$\begin{aligned}
u &= \frac{1}{2\eta}\frac{\partial p}{\partial x}\left(z'^2 - hz'\right) + \left(u_2 - u_1\right)\frac{z'}{h} + u_1\\
v &= \frac{1}{2\eta}\frac{\partial p}{\partial y}\left(z'^2 - hz'\right) + \left(v_2 - v_1\right)\frac{z'}{h} + v_1
\end{aligned} \tag{2.6}$$

The continuity equation for volume V enclosed by surface S entirely is

$$\frac{d}{dt}\int_V \rho dV = -\int_S \rho \mathbf{U}\cdot\mathbf{n}dS \tag{2.7}$$

with the outwards normal on surface $\mathbf{n}$. Let us consider the volume in the gap $z' = h(x,y,t)$, then

$$\frac{\partial}{\partial t}(\rho h) + \frac{\partial}{\partial x}\left(\int_0^h (\rho u)\, dz'\right) + \frac{\partial}{\partial y}\left(\int_0^h (\rho v)\, dz'\right) = 0 \tag{2.8}$$

Substituting Equations (2.6) to (2.8) gives

$$\frac{\partial}{\partial x}\left(\frac{\rho h^3}{12\eta}\frac{\partial p}{\partial x} - \rho h\left(u_1+u_2\right)/2\right) + \frac{\partial}{\partial y}\left(\frac{\rho h^3}{12\eta}\frac{\partial p}{\partial y} - \rho h\left(v_1+v_2\right)/2\right) - \frac{\partial(\rho h)}{\partial t} = 0 \tag{2.9}$$

The x direction is assumed to be equal with the direction of movement, hence $v_1 = v_2 = 0$. The final form of the Reynolds equation with the mean entrainment velocity defined as $u_m = (u_1+u_2)/2$ is

$$\frac{\partial}{\partial x}\left(\frac{\rho h^3}{12\eta}\frac{\partial p}{\partial x}\right) + \frac{\partial}{\partial y}\left(\frac{\rho h^3}{12\eta}\frac{\partial p}{\partial y}\right) - u_m\frac{\partial(\rho h)}{\partial x} - \frac{\partial(\rho h)}{\partial t} = 0 \tag{2.10}$$

The first two terms in (2.10) are called the Poiseuille terms describing the flow due to the pressure gradient. The third term, the so-called Couette or wedge term is responsible for the flow due to the mean velocity u_m. The last term, which is referred to as the squeeze term, represents the flow due to the squeeze effects. Equation (2.10) is an elliptical differential equation of second order defined on the domain

$$\left\{\Omega = (x,y) \in \mathbb{R}^2 : x_a \le x \le x_b \wedge y_a \le y \le y_b\right\}$$

It is completed with the following boundary conditions

$$\begin{aligned} p(x_a, y) &= p(x_b, y) = 0 \\ p(x, y_a) &= p(x, y_b) = 0 \end{aligned} \tag{2.11}$$

Cavitation condition

The cavitation conditions determines that if the pressure becomes smaller than the vapor pressure, the lubricant cavitates. In the cavitated region the pressure is constant and equal to the vapor pressure [10]. This condition is not included in the Reynolds equation (2.10), moreover it is assumed that the lubricant cavitates at zero pressure. By defining the cavitation condition the pressure is restricted to positive values only

$$p(x,y,t) \ge 0 \quad \forall (x,y,t) \in \Omega \tag{2.12}$$

2.1.2 Film thickness equation

The film thickness equation or the elastic deformation equation is introduced now. A major contribution was done in the area of elastic contacts by Hertz [11]. In order to approximate the elastic deformations of real bodies the following two hypotheses are considered [12]:

1. the contact dimensions are small compared to the size of the bodies allowing the approximation of the bodies by two semi-infinite half spaces [12],
2. the deformation is linear elastic, and the two contacting bodies have uniform and isotropic properties [12].

Considering the first hypothesis holds, the undeformed surfaces can be approximated as paraboloids (see Figure 2.1) defined by their radii of curvature in both x and y directions, i.e. by the values of R_{x1}, R_{y1} and R_{x2}, R_{y2} for solid 1 and 2 respectively. The reduced radii R_x and R_y are then

$$\begin{aligned} R_x^{-1} &= R_{x1}^{-1} + R_{x2}^{-1} \\ R_y^{-1} &= R_{y1}^{-1} + R_{y2}^{-1} \end{aligned} \tag{2.13}$$

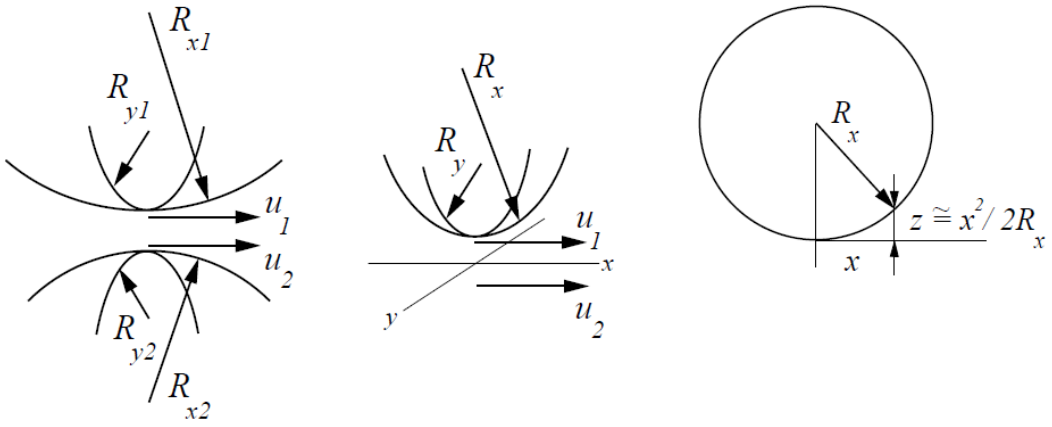

Fig. 2.1 Definition of the reduced radii of curvature and approximation of the undeformed surface by a paraboloid [10].

As described in Wijnant's work [10], the circular arc, based on Pythagoras's rule, given in Figure 2.1 is approximated by $z = R_x - R_x\sqrt{1-(x/R_x)^2}$. Taylor series around $x = 0$ yields $z \approx x^2/R_x$. The x and y coordinates are aligned to the principal directions of the gap, i.e. the cross-term xy cancels in the description. The directions of the surface velocities u_1 and u_2 are assumed to coincide and to be aligned to the x-direction. The y-coordinate is taken perpendicular to the x-coordinate [10].

The surface deformation δ in a point (x, y) caused by a load p in the origin is given by

$$\delta(x,y) = \frac{1-\nu^2}{\pi E_r}\frac{p}{\sqrt{x^2+y^2}} \tag{2.14}$$

The deformation $\delta(x, y)$ under a distributed normal load is obtained by integrating over the x and y coordinates

$$\delta(x,y) = \frac{1}{E_r}\int\int_A \frac{p(x',y')\,dx'dy'}{\sqrt{(x-x')^2+(y-y')^2}} \tag{2.15}$$

where the lubricant pressure p at (x', y') acts uniformly over an elementary area $dx'dy'$ of each body surface, δ is the sum of their two individual deflections at (x, y)

due to the distribution of p over the footprint area A of their surfaces and E_r is their reduced Young's modulus defined as

$$\frac{1}{E_r} = \frac{1}{\pi}\left(\frac{1-\nu_1^2}{E_1} + \frac{1-\nu_2^2}{E_2}\right) \tag{2.16}$$

Consequently, the film thickness equation is

$$\begin{aligned} h(x,y) = h_0(t) + \frac{x^2}{2R_x} - \mathcal{R}(x,y,t) + \\ + \frac{y^2}{2R_y} + \frac{2}{\pi E_r}\int_{-\infty}^{\infty}\int_{-\infty}^{\infty}\frac{p(x',y')\,dx'dy'}{\sqrt{(x-x')^2+(y-y')^2}} \end{aligned} \tag{2.17}$$

with the rigid body approach h_0. The geometry of the roughness is defined by the function $\mathcal{R}(x,y,t)$ which can be prescribed in many different ways.

2.1.3 Force balance equation

In order to have an equilibrium of forces, the integral of the pressure distribution obtained from the Reynolds equation should balance the externally applied load w

$$w = \int_{-\infty}^{\infty}\int_{-\infty}^{\infty} p(x,y)\,dxdy \tag{2.18}$$

2.1.4 Variation of viscosity with pressure

The viscosity of a lubricant can vary several orders of magnitude with the pressure. The next part summarizes the models describing the variations of viscosity with pressure.

Barus relation

The simplest pressure-viscosity relation is the so called Barus relation [13] which is an exponential expression

$$\eta(p) = \eta_0 \exp(\alpha p) \tag{2.19}$$

where η_0 is the atmospheric viscosity and α the pressure-viscosity coefficient. The Barus relation can accurately approximate the viscosity up to 0.1 GPa of pressure. Although it has a form including also the temperature dependence, here just its isothermal form is presented.

Roelands relation

A more complicated but more realistic pressure-viscosity relationship is the Roelands relation [14]

$$\eta(p) = \eta_0 \exp\left((\ln(\eta_0) + 9.67)\left(-1 + \left(1 + \frac{p}{p_0}\right)^z\right)\right) \tag{2.20}$$

where z is the pressure-viscosity index (its value is typically around 0.6) and $p_0 = 1.96 \cdot 10^8$ Pa is a constant. The parameters z, η_0 and α are mutually dependent. The Roelands relation is reported to be applicable up to values of pressure approximately 1 GPa. Figure 2.2 compares the Barus and Roelands equations' dependence on the pressure. It clearly shows that over 0.1 GPa the Barus relation might overestimate the viscosity.

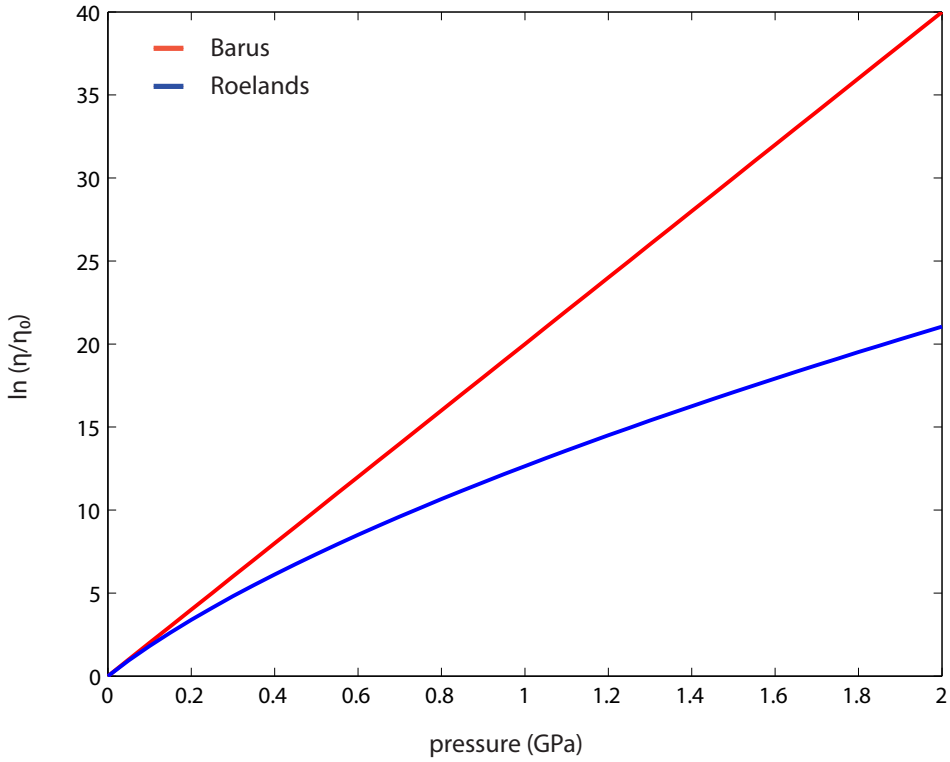

Fig. 2.2 The Barus [13] and Roelands [14] viscosity pressure relations.

Both the Barus and the Roelands models are strictly empirical without any physical relevance [15]. Two other viscosity relations of more physical relevance are

- the modified WLF model and
- the Doolittle model.

William, Landel and Ferry [16] proposed a model (WLF) based on the time - temperature equivalence principle specifying that it is possible to represent different rheological parameters of a fluid on one and only one "master curve" which is associated with a reference temperature corresponding to the glass transition temperature of the fluid [15]. A modified version of the WLF model proposed by Yasutomi et al. [17] enabled to extend the model to wider temperature and pressure domains. Definition of the model is e.g. in [15]. The Doolittle relationship [18] is based on the free volume principle and is valid over a wide range of pressures and temperatures, see e.g. [15] for its definition. These relations are more accurate especially at high pressure values. However, their complex mathematical formulation and their dependence on several parameters resulted in their rare application in current EHL models [15].

2.1.5 Variation of density with pressure

Somewhat less spectacular is the dependence of the density on pressure. Two models of the density variation will be mentioned.

Dowson-Higginson relation

The most widespread density-pressure relation is due to Dowson and Higginson [19]. Its isothermal form is

$$\rho\left(p\right) = \rho_0 \frac{5.9 \cdot 10^8 + 1.34p}{5.9 \cdot 10^8 + p} \tag{2.21}$$

where ρ_0 is the atmospheric density.

Tait equation of state

Another density-pressure relation is the Tait equation of state believed to be of more physical relevance. It is also more complicated and requires specific characterization and data [15]. Its definition can be found e.g. in [20] or [21].

2.2 Rheology models

In the previous section the basic EHL problem with a Newtonian lubricant behavior assumption was introduced. By "Newtonian" it is meant that the dependence between the shear stress τ and the shear rate $\dot{\gamma}$ is linear

$$\tau = \eta\dot{\gamma} \tag{2.22}$$

Although the Newtonian fluid model was used extensively in the early numerical works, especially for the smooth EHL problem and even for transient models, it failed to explain the non-linear shape of the experimentally measured traction curves under rolling-sliding conditions [22]. It was shown that the lubricant exhibits non-linear behavior when the values of the shear rate are high [1]. After reaching a certain limit, usually indicated by the shear stress value τ_0, the Newtonian response of the lubricant is lost and its behavior becomes non-linear.

Several attempts were made in order to incorporate the non-linear behavior of the lubricant into the EHL models. Johnson and Tevaawerk [23] applied the non-linear Maxwell model [24] in which the lubricant response was described by the Eyring theoretical sinh law [25] which was able to reproduce the experimentally measured traction curves

$$\dot{\gamma} = \frac{1}{G}\frac{d\tau}{dt} + \frac{\tau_0}{\eta}\sinh\left(\frac{\tau}{\tau_0}\right) \tag{2.23}$$

The first term on the right hand side of Equation (2.23) represents the fluid viscoelasticity which is often omitted in EHL models since its value is small when the shear rate is large [26]. The parameter η is the viscosity at low shear rate, and τ_0 is the characteristic parameter beyond which the lubricant starts to behave non-linearly. The Eyring model has a physical meaning based on the thermal activation theory of viscous flow [27].

Evans and Johnson [28] carried out experiments giving further support for the Eyring model, however, they indicated that the lubricant should have a limiting shear strength which is not described by the Eyring sinh law and so it has to be extended. Bair and Winer [29] proposed a non-linear constitutive equation assuming a limiting shear stress. Their non-linear model was based on laboratory tests using constant pressure stress strain apparatuses and high shear viscometers [30]. The limiting shear stress can be considered as a fluid property and it is representative of the material shear strength [26]. The model (including the measured limiting shear strength [22]) has the following form

$$\dot{\gamma} = -\frac{\tau_L}{\eta} \ln\left(1 - \frac{\tau}{\tau_L}\right) \tag{2.24}$$

with the limiting shear stress τ_L which is assumed to depend linearly on pressure

$$\tau_L = \tau_{L0} + \gamma p \tag{2.25}$$

where τ_{L0} is small (of order $O(1)$ MPa) and the value of the shear stress proportionality coefficient γ ranges between $0.03 \leq \gamma \leq 0.12$ [30]. It can be obtained independently from traction tests using a constant pressure stress-strain apparatus [30]. Gecim and Winer [31] presented a simplified form of Equation (2.24)

$$\dot{\gamma} = \frac{\tau_L}{\eta} \tanh^{-1}(\tau) \tag{2.26}$$

Several variations of the limiting shear stress model exist, e.g. the linear [32] or the circular [33] models. Elsharkawy and Hamrock [34] generalized these models as

$$\dot{\gamma} = \frac{\tau}{\eta}\left(1 - \left(\frac{\tau}{\tau_L}\right)^n\right)^{-1/n} \tag{2.27}$$

where $n = 1$ for the linear model, $n = 2$ for the circular model, and approximately $n = 2.8$ for the Gecim and Winer model. Figure 2.3 shows the dependence between the shear strain rate and shear stress described by the above mentioned models.

Another approach is the one referred to as the generalized Newtonian model. This model considers only the shear thinning aspect and neglects other aspects of non-Newtonian behavior, see for details [35]. Bair and Qureshi [36] pointed out that the nature of real shear-thinning in EHL contacts involves power-law response and a second Newtonian response respectively. The most general power-law model is the Carreau-Yasuda equation [37]

$$\eta = \mu_2 + (\mu_1 - \mu_2)\left(1 + (\lambda\dot{\gamma})^a\right)^{(n-1)/a} \tag{2.28}$$

where μ_1 is the viscosity at low shear rate, μ_2 denotes the second Newtonian viscosity, λ is a time constant generally expressed as a Maxwell time constant, for details see e.g. [35]. Parameter a controls the breadth of the transition from Newtonian to power law regimes [36]. The power law exponent n can only be obtained through experiments or by non-equilibrium molecular dynamics simulation [36]. Figure 2.4 shows the behavior of a shear thinning lubricant described by the generalized Newtonian model.

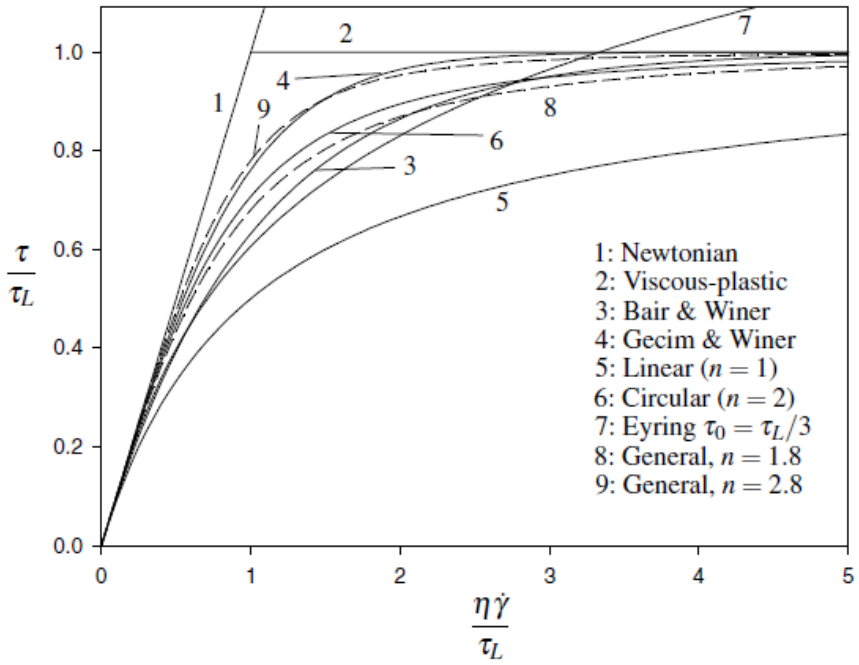

Fig. 2.3 The non-Newtonian rheological models [27].

Setting $\mu_2 = 0$ and the power law exponent to $n = 1/3$ we obtain a special case of the Carreau model (2.28), the Rabinowitsch model [38]

$$\eta(\tau) = \frac{\mu_1}{1 + (\tau/G)^2} \tag{2.29}$$

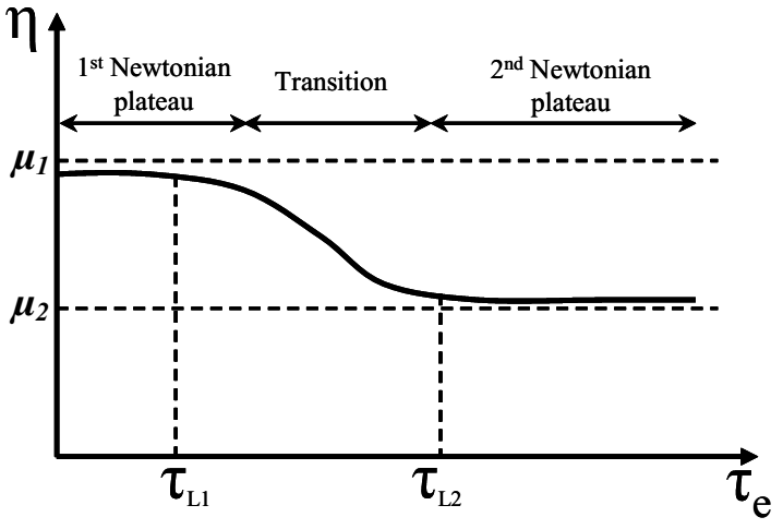

Fig. 2.4 Behavior of a shear thinning lubricant described by the generalized Newtonian model [15].

2.2.1 Mathematical formulation of the non-Newtonian Reynolds equation

The incorporation of the non-Newtonian effects into the EHL model is not straightforward. The complexity of these expressions depends on the rheological model. For line contacts its derivation is relatively simple, full numerical solutions were done with the linear model ($n = 1$) by Wang [32] and Iivonen and Hamrock [39], with circular model ($n = 2$) by Lee [33] and Hsiao and Hamrock [40]. Solution of the Eyring model for the one-dimensional case was given e.g. by Sui and Sadeghi [41].

The derivation of the Reynolds equation and non-Newtonian expressions for the two-dimensional model are in general complicated. The first attempt to present the two-dimensional case resulted in a modified non-Newtonian Reynolds equation provided by Kim and Sadeghi [42]. Its dimensionless form is the following

$$\begin{aligned}\frac{\partial}{\partial X}\left(\frac{\rho}{\eta}\frac{\partial P}{\partial X}H^3\left(G_1-G_2\right)\right)+\frac{\partial}{\partial Y}\left(\frac{\rho}{\eta}\frac{\partial P}{\partial Y}H^3\left(G_1-G_2\right)\right)-\\ \left(\lambda_2-\lambda_1\right)\frac{\partial}{\partial X}\left(\rho H G_3\right)+\lambda_1\frac{\partial}{\partial X}\left(\rho H\right)=0\end{aligned} \tag{2.30}$$

where

$$\begin{aligned}G_1 =& \int_0^1\int_0^Z f\left(\tau_e\right)\tilde{Z}d\tilde{Z}dZ\\ G_2 =& \frac{\int_0^1 f\left(\tau_e\right)\tilde{Z}d\tilde{Z}}{\int_0^1 f\left(\tau_e\right)d\tilde{Z}}\int_0^1\int_0^Z f\left(\tau_e\right)\tilde{Z}d\tilde{Z}dZ\\ G_3 =& \frac{\int_0^1\int_0^Z f\left(\tau_e\right)d\tilde{Z}dZ}{\int_0^1 f\left(\tau_e\right)d\tilde{Z}}\end{aligned} \tag{2.31}$$

Analytical expressions of the integrals in Equation (2.31) are not available. In order to solve Equation (2.30) the integrals have to be solved numerically across the film thickness Z, however, this task can be very time-consuming.

Another choice is to simplify the expression of the rhelogical function (2.23) allowing direct integration as was proposed by Ehret [43] or Holt [44]. Greenwood [45] showed that this approach yields good approximation for the point contact model. Jacod [30] presented the derivation of the effective viscosities based on the perturbation approach for the two-dimensional point contact for the Eyring and the circular limiting shear stress model. The non-Newtonian effects are included in the Reynolds equation (2.10) by means of effective viscosities η_x and η_y

$$\frac{\partial}{\partial x}\left(\frac{\rho h^3\eta_x}{12\eta}\frac{\partial p}{\partial x}\right)+\frac{\partial}{\partial y}\left(\frac{\rho h^3\eta_y}{12\eta}\frac{\partial p}{\partial y}\right)-u_m\frac{\partial\left(\rho h\right)}{\partial x}-\frac{\partial\left(\rho h\right)}{\partial t}=0 \tag{2.32}$$

Chapkov [46] (and before Greenwood [45]) presented the derivation of the Rabinowitsch model in which case the integrations are longer but can be done analytically. Charles [47] also used the Rabinowitsch model for both line and point contacts.

The derivation of the generalized Reynolds equation can be used with any model provided that the latter is written as a function of the generalized Newtonian viscosity (2.28) [15]. Bair [48] presented different forms of the one-dimensional Reynolds equation for various generalized Newtonian models.

2.3 Smooth EHL

Advances in the computational technology enabled to solve a wide variety of lubrication problems. The current section outlines some of the main characteristics of the pressure and film thickness distributions revealed by the early numerical solutions of the smooth EHL problem.

The first attempts to solve the EHL model numerically considered only the one-dimensional line contact case. Major simplifications had to be made, see Section 2.1, including the assumption of perfectly smooth contacting surfaces which enabled stationary solutions. Petrusevich [7] came with the first analytical-numerical solution of the pressure and film thickness distribution discovering a second local maximum, the so-called pressure spike - see Figure 2.5.

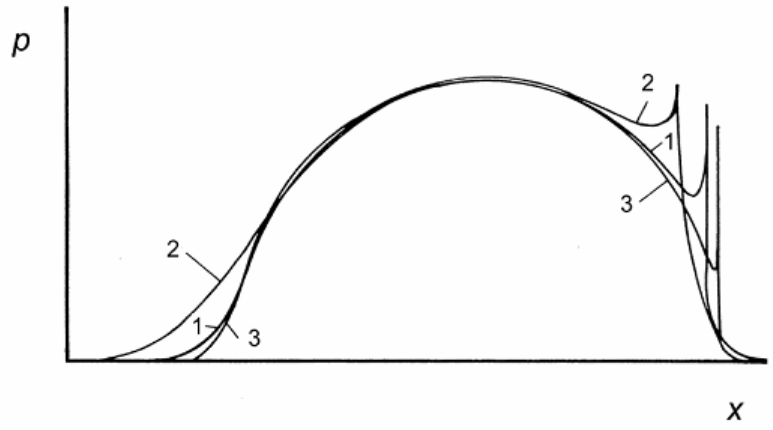

Fig. 2.5 Pressure distributions with the pressure spike presented by Petrusevich [7].

Dowson and Higginson [49] presented in 1959 a fully numerical study of the line contact including an empirical minimum film thickness formula. Works dealing with the two-dimensional point contact were less widespread due to its higher complexity. Publications of point contact approaches worth mentioning are e.g. Cameron and Gohar [50], Wedeven [51] or Cheng [52]. Cameron and Gohar [50] and Wedeven [51] solved the 2-D problem based on Grubin's assumptions [6] of the line contact combined with the Hertzian theory. Cheng's study [52] was the first generalized work in which it was pointed out that the pressure and the parameter describing the lubricant side-flow depend on the ellipticity ratio. The first fully numerical solution of the point contact was presented by Ranger et al. [53]. Their model was able to find the values of the central and minimum film thicknesses and they presented general formulas for calculating these values. A common feature of these works was that they could handle only lightly loaded cases, e.g. the point contact

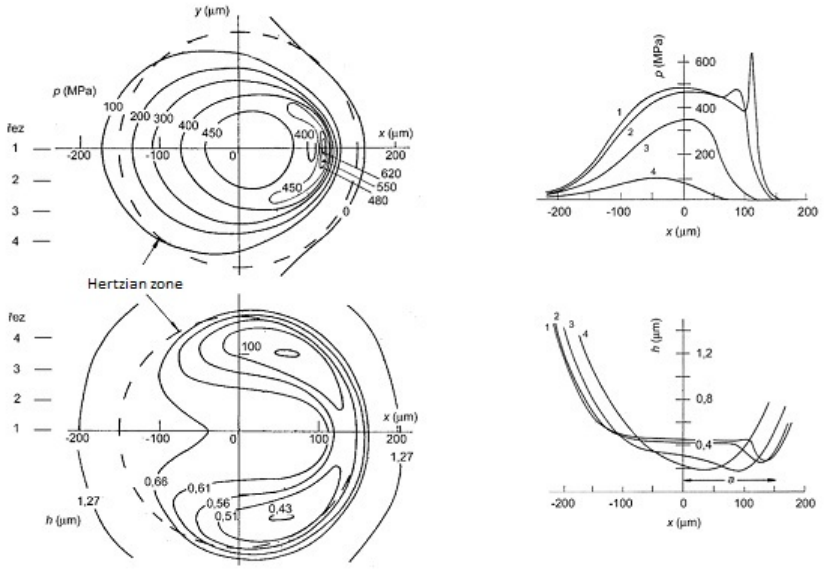

Fig. 2.6 Film thickness and pressure distribution in an EHL point contact for a load 22.2 N and entrianment velocity 0.33 m/s presented by Ranger [53].

solutions were limited to 0.5 GPa. An example of Ranger's [53] work is shown in Figure 2.6.

Hamrock and Dowson [54]-[55] designed empirical central and minimum film thickness formulas based on 34 simulations carried out for different combinations of load, material properties and speed. They introduced these formulas in terms of the ellipticity ratio k and the dimensionless parameters W, U and G which simplified the number of mutually dependent input parameters. Their definitions are the following:

- parameter of load

$$W = \frac{w}{E_r R_x^2} \tag{2.33}$$

- parameter of speed

$$U = \frac{\eta_0 u_m}{E_r R_x} \tag{2.34}$$

- parameter of material

$$G = \alpha E_r \tag{2.35}$$

- the ellipticity ratio

$$k = \frac{a}{b} \tag{2.36}$$

The central film thickness formula for the point contact is

$$H_c = 2.69 \cdot U^{0.67} \cdot G^{0.53} \cdot W^{-0.067} \cdot \left(1 - 0.61 \exp^{-0.73k}\right) \tag{2.37}$$

and the minimum film thickness formula is

$$H_{min} = 3.63 \cdot U^{0.68} \cdot G^{0.49} \cdot W^{-0.073} \cdot \left(1 - \exp^{-0.68k}\right) \tag{2.38}$$

The formulas were constructed using the least mean square method, their accuracy is reported to be within ±5%. They are widely used up to recently as reference values, however, their validity is limited rather to lightly loaded cases.

The experimental investigation of EHL was ahead of the simulations, however, for the lightly loaded cases these simulations confirmed the experimentally observed film thickness characteristics, such as its horseshoe shaped distribution.

The first solution enabling the study of more realistic conditions in the contacts was presented by Houpert and Hamrock [56] who reported solutions of the line contact up to 4.8 GPa. They observed a local film constriction at the outlet of the contact related to the pressure spike. Introduction of the multigrid [57] and multilevel multi-integration [9] techniques was a major step forward in the theoretical EHL research enabling the simulation of highly loaded point contacts (up to 3.3 GPa) as well as transient problems.

Lubrecht investigated not only the scope of Hamrock and Dowson's empirical formulas but he studied the ratio of the central H_c and minimum H_{min} film thickness is constant for the line contacts [58]. Lubrecht ran simulations for a wide range of operating conditions and proved that for point contacts this ratio is no longer constant. In his work the Hamrock-Dowson dimensionless parameters were replaced by the Moes parameters [59] of load M and material L, further reducing the number of mutually dependent inputs. The Moes parameters can be expressed in terms of the Hamrock and Dowson's parameters as:

- parameter of load

$$M = W\,(2U)^{-\frac{3}{4}} \tag{2.39}$$

- parameter of material

$$L = G\,(2U)^{\frac{1}{4}} \tag{2.40}$$

Further work [60]-[61] included the study of the effect of these parameters on the film thickness and the pressure distribution. It was shown that with increasing M, a horseshoe shaped region (i.e. sidelobes) forms in the film thickness distribution. These sidelobes become smaller with increasing load parameter and move in the outward direction until for large M the minimum film thickness is practically found at the side of the contact, i.e. at $X = 0$, $Y = \pm 1$ [61].

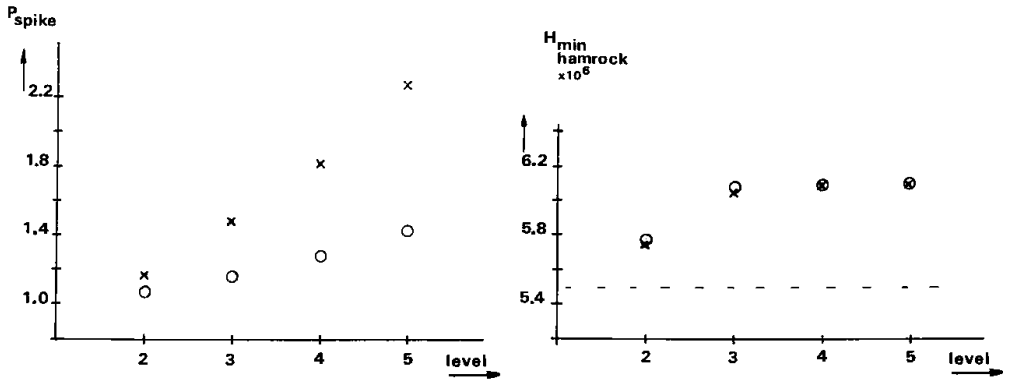

Fig. 2.7 The height of the pressure spike and the minimum film thickness as a function of grid points for a compressible (∘) and an incompressible (×) fluid presented by Lubrecht [58].

The pressure distribution approaches the Hertzian dry contact pressure distribution with increasing load parameter M, while the height of the pressure spike is

reduced. For a given M and increasing L, however, the pressure spike gradually develops from a small ridge into a real spike. Lubrecht [58] and Venner [62] investigated the pressure spike in detail. It is believed to be a numerical effect caused by the exponential relation between the viscosity and the pressure and represents a logarithmic singularity. They compared its height for both the Barus and Roelands viscosity relations and also checked the effect of lubricant compressibility. The use of the Roelands relation lowered its height, as well as the assumption of a compressible fluid. On the other hand, the compressibility affected the minimum film thickness only slightly. Lubrecht showed that the height of the spike depends on the number of grid points too, see Figure 2.7.

Moes et al.[63] presented a new central film thickness formula in terms of parameters M and L based on the parametrical study of Venner [60]-[61]

$$H_c^M = \left\{ \left[1.7 \cdot M^{-1/9} \cdot L^{3/4} \cdot t \right]^r + \left(47.3 \cdot M^{-2} \right)^s \right\}^{1/s} \tag{2.41}$$

with

$$r = e^{1-\frac{6}{L+8}}, \quad s = 12 - 10e^{M^{-2}} \quad \text{and} \quad t = 1 - e^{-0.9\frac{M^{1/6}}{L^{1/6}}}$$

Figure 2.8 shows comparison of central film thickness values predicted by Equation (2.41) and numerical calculation by Venner [9].

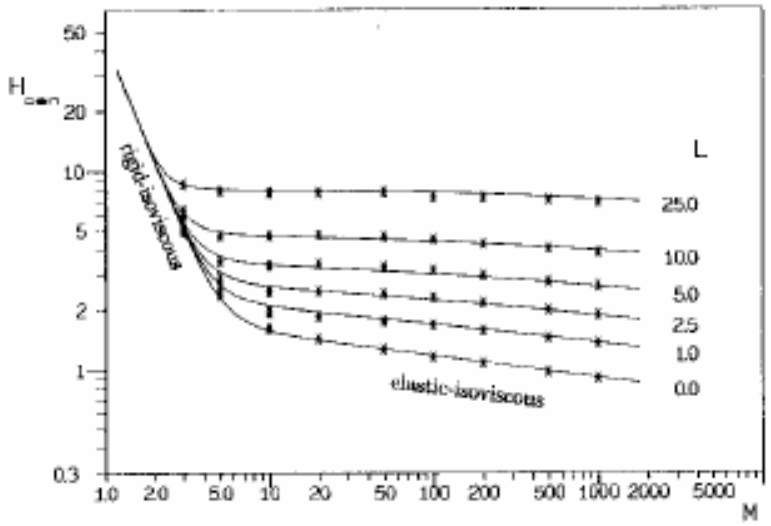

Fig. 2.8 Calculated values of the dimensionless central film thickness parameter H_c as a function of M and L, the drawn line give the predictions of Equation (2.41) [9].

In another paper Venner [64] discussed the effects of compressibility on the film thickness: "*It was shown that, although compressibility is not one of the predominant effects accounting for film formation, it does determine to a great extent the shape of the lubricant film in the central region of the contact*". Furthermore, an analysis of the Reynolds equation resulted in an accurate formula predicting the compressibility effect on the central film thickness in moderately to highly loaded contacts assuming the incompressible result is known. Due to strongly increasing ratio between the

central and minimum film thicknesses in circular contacts it is very unlikely that the minimum film thickness occurs on the center of the contact (unlike the line contact case).

The influence of the non-Newtonian effects on the pressure and film thickness was examined e.g. by Kim [42], Holt [44] or Lee [65]. The numerical research concentrated primarily on one-dimensional contacts due to the complexity of the rheological functions. Lee compared the rheological models of Bair-Winer (2.24), Gecim-Winer (2.26) and Carreau (2.28) for the line contact. He studied the effects of various conditions (loads, speeds, temperatures, limiting shear stress, SRR) on the film thickness concluding that the minimum film thickness increases with decreasing temperature, decreasing average pressure and increasing rolling speed. The influence of SRR and limiting shear stress on the minimum film thickness is not significant, but the values of the minimum and central film thickness decrease with increasing SRR [65]. The differences between the rheological models is small as well, the largest film thickness was obtained with the Carreau model.

Under usual operating conditions in a smooth EHL contact the non-Newtonian effects do not cause significant differences compared to the Newtonian model. The same conclusions were confirmed by several other authors e.g. [26] or [66]. Similar results were obtained for the two-dimensional non-Newtonian Eyring model. The results indicate that the effect of SRR on the minimum film thickness is negligible [42]. Under pure rolling and low sliding conditions there is little difference between the Newtonian and non-Newtonian model. At higher degree of sliding the film thickness at the central area is lowered by up to 10% [44]. Under sliding conditions the pressure spike is reduced [42].

2.4 EHL of non-smooth surfaces

Once the smooth surface EHL model was solved, attention of the researchers has turned towards surface roughness problems. The idea of perfectly smooth contact surfaces is a very crude assumption which does not reflect the conditions in real machine components. These machine elements usually encounter some surface roughness.

2.4.1 Statistical approach

In the end of 1970's surface roughness was incorporated to the EHL model by means of stochastic approaches. Such an approach was used by Tzeng [67], Christensen [68] or Elrod [69]. The main feature of the approach was the use of an averaged Reynolds equation, based on the characterization of the roughness by statistical numbers like the root mean square value of the roughness R_q, the average orientation or the auto-correlation length of the roughness [27]. These models were limited to two specific types of roughness structures: one-dimensional transverse or longitudinal ridges [70]. The most well-known and widely used method was the average flow method introduced by Patir and Cheng [70]-[71]. Their average Reynolds equation was defined for rough surfaces in terms of pressure and shear flow factors which were obtained by numerical flow simulation. The empirical relations for the flow factors

were defined as functions of the surface roughness characteristics. The advantage of the approach is that it can be applied to any 3-D roughness. It was shown that the film forming capability increases as the surface roughness pattern changes from longitudinal to isotropic and then to transversely orientated feature [71]. Patir [71] observed that sliding may increase or decrease the film thickness depending on the roughness of the two surfaces. Patir's flow model was widely applied to the line contact case by e.g. Majumdar [72], Jeng [73], Zhu [74] or Sadeghi [75]. The flow factor method has some serious limitations. One of these is that the model is based on the statistical averages of the surface topography described by only three parameters, though different surface profiles can have the same statistical properties and so the flow factor model gives the same average pressure even though the profiles may cause completely different effects [27]. Another limitation is the neglect of the elastic deformation of the asperities. Since the flow factors are obtained based on a hydrodynamic analysis, only the elastic deformation of the global geometry is assumed.

2.4.2 Deterministic approach

Advances in the computational techniques enabled simulations with deterministic models. Lubrecht [58] studied the influence of different surface features (e.g. longitudinal and transverse roughness, isotropic bump, longitudinal furrow or scratch) on the basic EHL parameters of a line contact. His solution was assuming that the surface with the roughness feature is stationary. A "rule of thumb" was defined stating that the influence of an asperity on the film thickness and maximum pressure is proportional to its amplitude and inversely proportional to its radius (or width) [58]. Furthermore, he observed that for high loads the asperities are flattened due to the Couette flow and they have small influence on film thickness (can not flow around it). For low loads, an opposite process is typical showing considerable changes in film thickness accompanied by less dramatic pressure changes.

Venner continued the work with stationary rough models, however, he stated that only relatively shallow dents and waviness can be simulated and the model does not correctly model the pressure generation from a cavitated region [9]. The method was also applied to real measured surface roughness data. Moreover, he revealed the importance of time-dependent simulations. Since in an EHL contact generally both surfaces move, the Reynolds equation should contain the squeeze term as well. Previous examples of works dealing with the transient EHL line contact are Lee and Hamrock [76], Chang [77] or Oh [78]. They presented solutions for lightly loaded cases with only few time steps and spatial points. Venner ran simulations of the over-rolling of different surface features (indentations, bumps and waviness) in line contacts.

Venner [9] compared stationary and transient solutions with a dent placed at a given position. Several effects of the squeeze term were discovered. A steady-state solution, with a dent placed in the contact center, was completely flattened out resulting in a nearly uniform film thickness. This fact was explained by the

reduction of the Reynolds equation to

$$\frac{d(\rho h)}{dx} \approx 0 \tag{2.42}$$

In the transient model, on the contrary, the dent being at the same location shows up in the film thickness. The Reynolds equation reduces in this case to

$$-\frac{\partial(\rho h)}{\partial x} - \frac{\partial(\rho h)}{\partial t} \approx 0 \tag{2.43}$$

Equation (2.43) states that at high loads the film thickness h will be the function of $(x-t)$, the density ρ is limited. This would imply that there is a tendency to preserve the geometry of the feature during the time it moves through the contact zone [9]. Nevertheless, according to Venner this fact still does not explain the smaller change in the geometry, and to satisfy Equation (2.43) the wedge term has to change accordingly resulting in non-uniform film thickness. Explained in physical terms, he states that due to the high viscosities the pressure induced flow is almost absent in the contact zone resulting in a shear flow dominated solution.

Venner further investigated the differences between pure rolling and rolling-sliding condition proving that the differences between the stationary and transient simulations are even more accentual for sliding contacts. While for pure rolling once the feature is inside the Hertzian zone, it tends to undergo only slight changes, but when sliding is assumed (i.e. surfaces move at different velocities) some interesting observations were revealed. Equation (2.43) says that the change in film thickness caused by the feature travels with the average velocity, however, it does not state anything about the velocity of the feature itself and the film thickness variation is independent of the feature's velocity. Venner argues that in order to avoid the violation of the mass conservation in the flow, the system has to move the trapped fluid through the contact zone by means of the Couette flow, i.e. film thickness variations [9].

Differences can be observed between the line and point contact models. The additional spatial dimension of the point contact model enables the fluid to flow around the feature and consequently it may affect the film thickness even more.

Several papers further investigated the influence of different surface features on the film thickness and pressure distribution under pure rolling and rolling-sliding conditions: [9], [79] - [86]. The different surface features can be characterized as local (e.g. dent, bump), or global (e.g. waviness). A third group is formed of ridges and scratches which are local in one dimension but global in the second dimension [86]. Unless the feature is longitudinally orientated, transient two-dimensional calculations are necessary.

Dents (large scale features)

For the local types of features, such as a dent or bump, amplitudes much larger than the film thickness are typical. It was shown by experiments that indentations, significantly reduce the surface fatigue life [9]. Venner defined the shape of the dent for the one-dimensional model as

$$R(X,T) = A10^{-10\left(\frac{X-X_d}{W}\right)^2} \cos\left(2\pi\frac{X-X_d}{W}\right) \tag{2.44}$$

in order to avoid the sharp corners at the edges. In Equation 2.44 A is the dimensionless amplitude of the dent, W its dimensionless wavelength and X_d denotes the location of the dent. Both stationary (for a fixed location X_d) and transient calculations were done. Comparing the two models, the effect of the squeeze term is apparent. For the case when $X_d = 0$ the stationary model predicts almost symmetrical pressure rise at the trailing and leading edges of the dent, unlike the transient model, which shows an asymmetry - see Figure 2.9.

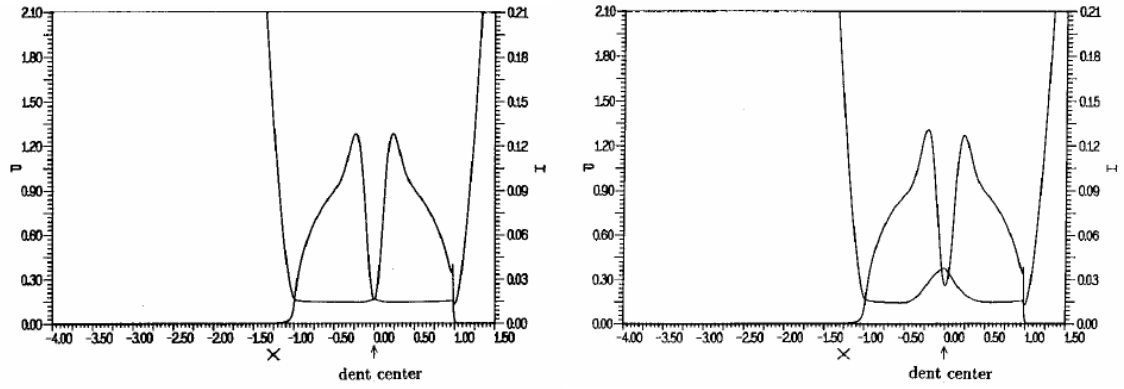

Fig. 2.9 Stationary (left) and transient (right) solution of pressure and film thickness distributions with a dent located at $X_d = 0.0$ [9].

As described above the pressure flow will be absent inside the contact resulting in a dominating shear flow. This causes that an additional amount of fluid is trapped in the dent upon its entrance, and just shifted through the contact region [9]. Similar investigations were carried out for bumps and waviness where again the effect of squeeze term is visible causing more obvious differences in the film thickness.

In case of slip, Venner observed that the film thickness variations caused by the roughness feature traveled through the Hertzian zone with the average velocity independent of the surface feature's velocity itself. Figures 2.10 show the asynchronism between the film thickness variations and pressure disturbance.

Similar observations to Venner's were presented by Ai [79] who also reported an "induced image" traveling at the average speed when the surface irregularity moves through the contact region. For pure rolling this image is synchronized with the original profile of the irregularity accompanied by mild pressure fluctuations. Later, studying a moving dent, Ai [80] further investigated the effect of sliding on the pressure and film thickness. When sliding is significant the pressure is higher at the leading edge of the dent if the dent is on the slower surface. For the opposite case, the pressure is higher on the trailing edge. The pressure fluctuations increase with increasing slide to roll ratio and dent depth and decreasing dent width.

Lubrecht [86] presented a hypothesis stating that the dry contact model is a good approximation for features with much larger amplitudes than the film thickness - e.g. dent. The disadvantage of the dry contact approach is the lack of prediction of the failure position. Venner observed that the failure position is to be appear on the trailing edge of the dent [9]. The life reduction of a contact as a function of the maximum smooth surface contact pressure, the dent size and the slope of the dent,

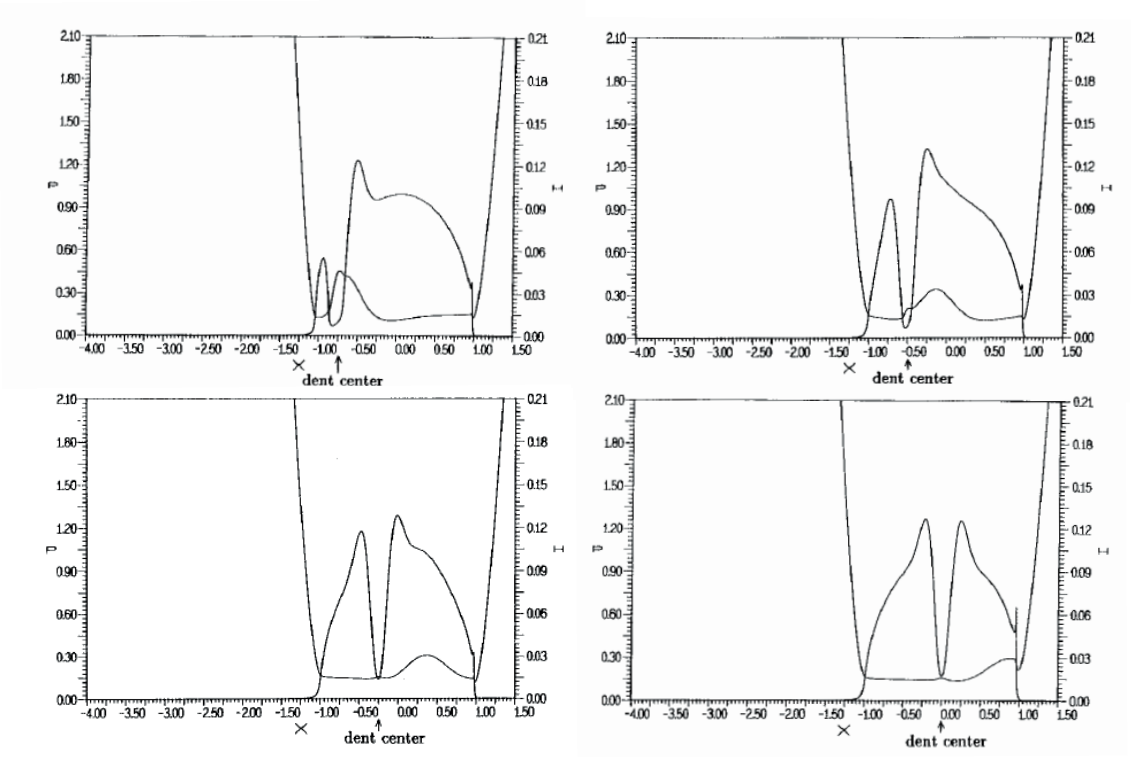

Fig. 2.10 Transient solution of a dent assuming slip for different positions of the dent [9].

was shown revealing that with increasing dent size and slope the life is reduced more and more [86].

Transverse ridge

A harmonic function was used in order to describe the transverse ridge defined again by the amplitude A, wavelength W and ridge location X_d

$$R(X,Y,T) = A10^{-10\left(\frac{X-X_d}{W}\right)} \cos\left(2\pi\frac{X-X_d}{W}\right) \tag{2.45}$$

Stationary simulations of the ridge showed that the ridge completely deforms in the center of the contact affecting the film thickness only near the edge of the contact, in the side lobe area [81]. Under pure rolling it can be observed that the restricted area which is formed when the ridge enters the contact remains localized around the ridge, both travel at the average surface velocity [81]. Moreover, there is an asymmetry in the film thickness showing a larger increase before the ridge than behind it.

When the rough surface is slower than the average velocity (slide to roll ratio, SRR=1) the film thickness modulation moves ahead the ridge itself. The authors [81] pointed out that the main changes in the film thickness occurred when the ridge passed a given location. A half-moon shaped restriction formed in the film thickness is due to the different behavior in the shear flow dominated and pressure flow dominated regions. In the high pressure zone the ridge itself is completely flattened as it progresses through the contact, just as in the simple sliding case,

creating a similar increase in pressure over the ridge. The width of the restriction (or its apparent wavelength) is larger than that of the original ridge $W^*/W = u_s(2u_2) = 2$.

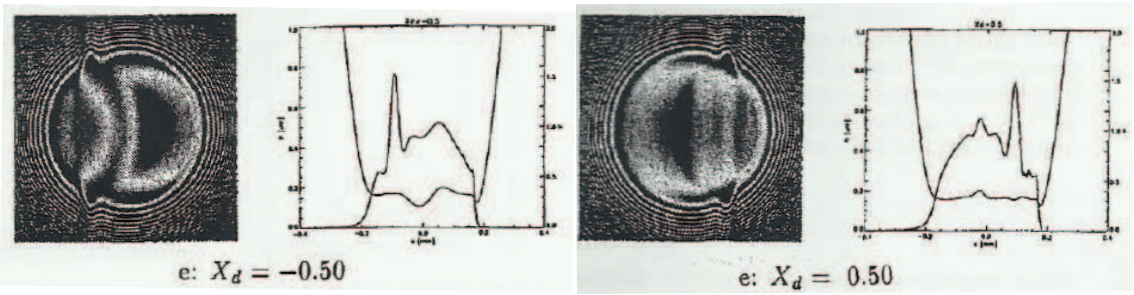

Fig. 2.11 Transient pseudo-interference plots and centerline film thickness and pressure for two cases: positive (on the left) and negative (on the right) SRR at given locations X_d [81].

In opposite case, i.e. when the surface with roughness is faster, a half-moon shaped restriction of film thickness occurs as well, but in the reverse direction with respect to the entrainment velocity [81]. Figure 2.11 illustrates pressure and film thickness variations for positive and negative slide to roll ratios at certain location of the ridge. The half-moon shape restrictions are clearly visible in the figure.

The simulations were compared with the experimental results of Kaneta [87] showing good agreement in case of the transverse ridge. Differences particularly around the ridge can stem from the discretization order or from the assumption of Newtonian iso-thermal model [81].

Greenwood and Morales-Espejel [85] provided a different approach proposing an analytical solution of a linearized Reynolds equation for any two-dimensional transverse roughness. This analysis was carried out also for the transient Reynolds equation which was enabled due to negligible viscosity effects in the contact region. The theory of the linearized solution is based on previous investigations suggesting to replace the finite parallel film of the Hertzian region in an EHL contact by an infinite parallel channel of the same width and with constant pressure equal to the maximum Hertzian pressure [85]. With this assumptions simplified expressions for the pressure and deformations are obtained. A criterion relating the amplitudes of the undeformed and deformed roughness to the wavelength was defined which suggested that long wavelength (or ratio λ/h) roughness is ironed out while short wavelength roughness is likely to persist after deformation. The authors also confirmed the assumption that sinusoidal pressures can be correctly regarded as induced by sinusoidal roughness [85]. Further, they investigated the previously observed phenomena of the moving surface irregularities under rolling-sliding by e.g. [9] or [81].

The authors found that the complete solution is made of two separate parts which they named as the particular integral (moving steady state solution) and the complementary function due to the inlet modulation of film. They emphasize the importance of the understanding of this kinematic behavior of the moving roughness, as well as the role of the contact inlet which cannot be neglected in the modulation of the amplitude and wavelength of the final shape [85]. The behavior of the above mentioned components is demonstrated by an example in Figure 2.12 of a rough surface moving with velocity u_2 and a smooth surface moving with u_1. The left part

of the figure refers to the steady state solution where in order to deform the original roughness a pressure distribution has to build up traveling with velocity of the rough surface u_2. The middle of the figure illustrates the effect of the flow variation due to the entering of partially deformed roughness at the inlet producing film thickness variations and pressure disturbances. The two components add up and create a final shape shown on the right part of figure.

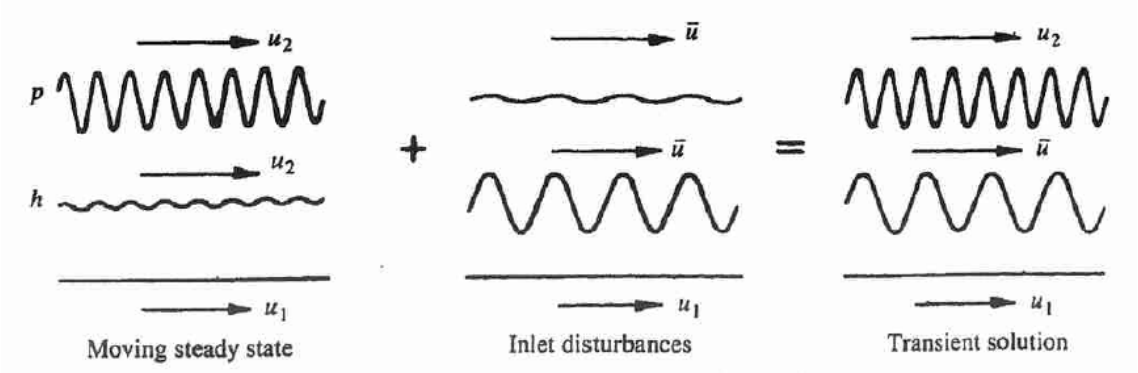

Fig. 2.12 Behavior of the two components: moving steady state solutions and inlet disturbances [85].

Waviness

Similarly to the ridge, the waviness can be described by harmonic functions. The transverse, respectively the longitudinal waviness are

$$R_t(X,Y,T) = \begin{cases} 0, & X \geq X_d \\ A\sin\left(2\pi\frac{X_d - X}{W}\right) & X < X_d \end{cases} \tag{2.46}$$

respectively

$$R_l(X,Y,T) = A\cos(2\pi\frac{Y}{W}) \tag{2.47}$$

where again X_d denotes the location of the feature. In both cases the feature is defined by its amplitude A and wavelength W. Stationary simulations were carried out to compare the behavior of longitudinal and transverse waviness. Since in this case the flow is dominated by the Couette term, the transverse waviness is almost completely deformed in the high pressure region accompanied by large pressure ripples [82], while the longitudinal waviness hardly sustained any deformation and the pressure fluctuations were small - see Figure 2.13.

Moving towards the transient results, the case of pure rolling is described first. Considering a waviness both the pressure and film thickness variations are in phase. Pressure fluctuations are smaller than in the stationary case unlike the film thickness variations which are larger [83].

When the rough surface is slower than the average velocity (the slide to roll ratio is SRR=1) the waviness influence traveling with the average velocity progresses in front of the waviness itself causing an important film thickness variations and small pressure disturbance [82]. The two waves are the most distinguishable in this case. In

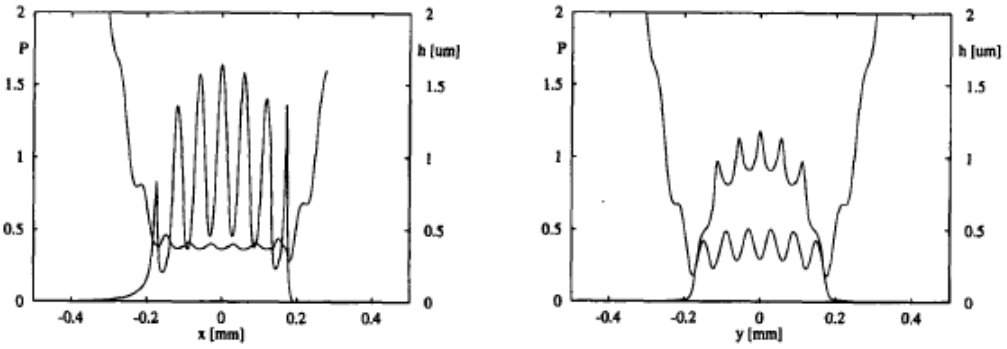

Fig. 2.13 Pressure and film thickness variations for transverse and longitudinal stationary waviness [82].

the opposite case, i.e. when the surface with the roughness is faster (i.e. SRR= -1) the film thickness disturbances trail behind the location of the waviness.

The authors studied the values of the central and minimum film thicknesses as a function of time. Their observations are summarized in Table 2.1 where the values of the decrease, resp. increase compared to smooth values are presented.

Tab. 2.1 Central and minimum film thicknesses as function of time and their dependence on slide to roll ratio according to the numerical simulations in [83].

	Pure rolling $u_{smooth} = u_{rough}$	SRR = 1 $u_{rough} < u_{smooth}$	SRR = -1 $u_{rough} > u_{smooth}$
H_c	$\approx 10\%$ increase	$\approx$ same	$\approx 30\%$ decrease
H_{min}	$\approx 30\%$ decrease	$\approx 20\%$ decrease	$\approx 20\%$ decrease

The authors concluded that for transverse waviness contact between the two surfaces is expected first in the side lobe regions. Failure initiation is therefore the most likely to start at the extreme ends (Y) of the contact circle [83].

Ehret et al. [84] investigated the effect of various surface textures with different shapes on the minimum film thickness and the maximum pressure in an EHL point contact. Three roughness types were defined in the study as following: either a waviness (at some orientation angle, 0° for transverse waviness, 90° for longitudinal waviness), or a uniform distribution of asperities. It was shown that the minimum film thickness slightly increases with the orientation of the waviness in the conjunction for the pure rolling case. In case of pure sliding (steady surface with waviness, located in the center of the contact) the minimum film thickness exhibits a completely opposite trend. Here, the maximum value of film thickness is obtained for the transversely orientated waviness and declines as the orientation angle increases. The maximum pressure slightly increases with the orientation angle, and its value tends towards that obtained, in pure sliding conditions, for the longitudinal waviness. The values of maximum pressure under pure rolling conditions for the transverse and orientated waviness remain close to that of the smooth surface problem.

Under pure rolling conditions the minimum film thickness and maximum pressure are not very sensitive to the orientation of the waviness or the pattern of the surfaces. The minimum film thickness is governed by the lubricant flow for the waviness, it also

depends on the deformation of the ridges as they enter the contact. The magnitude of the deformation is mainly related to the wavelength of the ridge [84].

2.5 Roughness deformation

Surface features deform inside the contact as they pass through it. The magnitude of this deformation and the consequences it causes inside the contact and to the pressure and film thickness distributions were studied by several authors. Two different approaches are presented below, both are aimed to provide a systematic study of the roughness behavior inside the contact.

2.5.1 Amplitude reduction model

Lubrecht and Venner studied the roughness behavior extensively. Their efforts resulted in the so-called amplitude reduction model which enables to describe the deformation of a surface feature by a single dimensionless parameter. They pointed out that in order to understand the deformation of a real rough surface, the detailed knowledge of the amplitude reduction of harmonic features is necessary [88].

Formulas were derived for both line and point contact models describing the deformed amplitude of the roughness A_d as a function of the initial amplitude A_i, the wavelength λ and the operating conditions in terms of the Moes dimensionless parameters of load and material. These parameters were combined into a single parameter ∇.

First, the one-dimensional line contact under pure rolling conditions was studied, which resulted in the following expression for the amplitude reduction

$$\frac{A_d}{A_i} = \frac{1}{1 + 0.125\nabla_1 + 0.04\nabla_1^2} \tag{2.48}$$

with the single dimensionless parameter $\nabla_1 = (\lambda/b)\,(M_1^{3/4} L^{1/2})$ and the one-dimensional Moes parameters of load M_1 [88] and material L. A waviness defined as in Equation (2.46) was studied in [89]. For the situation when the initial amplitude A_i is much smaller than the smooth film thickness H_c a linear dependence between the deformed and initial amplitudes was observed. Equation (2.48) expresses that long wavelengths are almost completely deformed, while short wavelengths deform only very little. Although expected otherwise, the linear behavior between the amplitudes still remains for a waviness comparable to or much larger than the central film thickness. Figure 2.14a presents the amplitude reduction curve (2.48) for line contacts under pure rolling conditions clearly showing the differences observed in the behavior of features with long and short wavelengths.

The shape of the amplitude reduction curve is influenced by the specific operating conditions, among others by the mean velocity u_m. For its increasing values the curve tends to shift to the right, which can be counteracted by introducing a new parameter $\lambda/b/\sqrt{u_m}$. The range can be kept similar to the ones used before by scaling all velocities to the velocity u_m [89].

The shape of the curve is influenced by the slide to roll ratio too. Under rolling-sliding the film thickness variations have different wavelengths inside and outside the

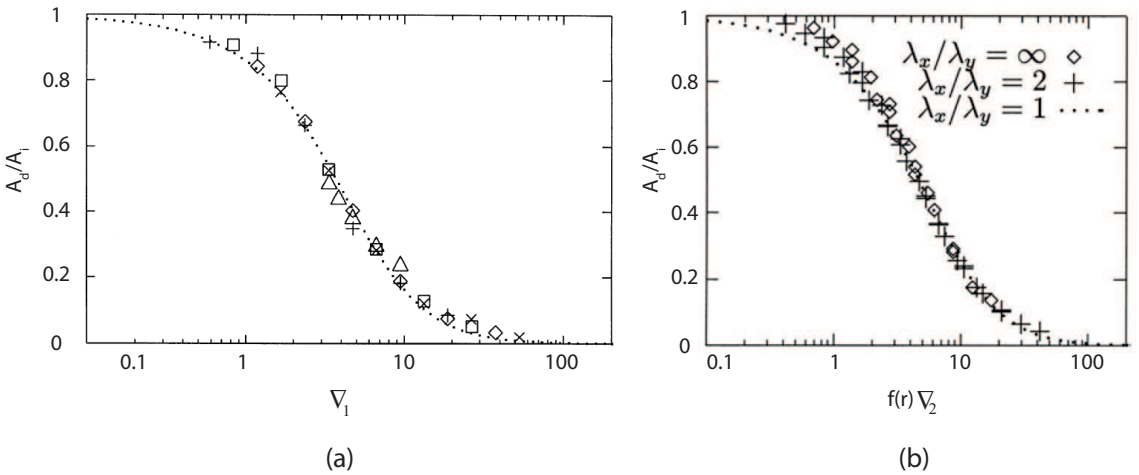

Fig. 2.14 (a) Amplitude reduction of a line contact under pure rolling conditions described by Equation (2.48) [88]. (b) Amplitude reduction of point contacts for different roughness orientations [91].

contact. In the high pressure zone the film thickness variation travels through the contact with the average velocity u_m. The dimensionless parameter ∇_1 in Equation (2.48) is replaced by $\overline{\nabla}_1 = \nabla_1/\sqrt{S}$, where S is the slide to roll ratio defined as $S = u_2/u_m$ (for pure rolling $S = 1$) [88].

The point contact problem is somewhat more complicated, the additional dimension requires an additional parameter: the wavelength of the waviness λ_y in the y direction. The harmonic patterns can be classified based on the values of their wavelengths in x and y directions, λ_x and λ_y. It is possible to create a single curve for all types of harmonic patterns, for the isotropic feature, and for the longitudinal and transverse waviness [91]

$$\frac{A_d}{A_i} = \frac{1}{1 + 0.15\overline{f}\,(r)\,\nabla_2 + 0.015\left(\overline{f}\,(r)\,\nabla_2\right)^2} \tag{2.49}$$

where

$$\bar{f}\,(r) = \begin{cases} e^{1-\frac{1}{r}} & \text{if } r > 1 \\ 1, & \text{otherwise} \end{cases} \tag{2.50}$$

and $r = \lambda_x/\lambda_y$. For the two-dimensional problem the parameter ∇_1 changes to

$$\nabla_2 = (\lambda/b)\left(M_2^{1/2}/L^{1/2}\right) \tag{2.51}$$

with $\lambda = \min(\lambda_x, \lambda_y)$ and M_2 the two-dimensional Moes parameter of load (2.39). Figure 2.14b shows that the amplitude reduction curve for point contacts behaves similarly as in the line contact case. The effect of ellipticity was studied as well [91]. Figure 2.15a illustrates that for all types of surface features with decreasing value of the ellipticity parameter the curve tends to shift to the right with respect to ∇_2.

Based on their observations Hooke and Venner [92] indicated that both line and point contacts follow similar behavior: the amplitude reduction depends on the operating conditions and on the orientation of the roughness pattern. The results suggests that there is a single mechanism controlling the behavior in all contacts depending primarily on the wavelength of the feature [92]. Hooke pointed out that the roughness behavior is controlled by the ratio of the roughness wavelength λ and the length of the inlet pressure sweep L. Comparison of the lubrication conditions at the inlet of a heavily loaded piezoviscous line contact and on the center-line of a heavily loaded piezoviscous point contact shows that it is possible to relate the lengths of these two pressure sweeps [92]. The ratio of the wavelength λ and length of pressure sweep L is

$$\frac{\lambda}{L} = \frac{1}{\overline{L}} \left(\frac{128}{27} \right)^{0.5} q \frac{\lambda}{a} P^{1.5} S^{-2} \tag{2.52}$$

with the Hertzian parameter a and q determined by the type of contact (for line contact its value is 1, for point contacts it varies from 1 until 0.89). The parameters P and S are the so-called Greenwood's parameters of pressure and speed [92]. The ratio of the attenuation is proportional to $q(\lambda/a)P^{1.5}S^{-2}$ and it can be seen in Figure 2.15b that the amplitude reduction exhibits similar behavior for given operating conditions for both types of contacts. Small differences are due to the side flow effects in point contact. The agreement between the results is better for transverse and in-line roughnesses if q is omitted, for iso-tropic features the agreement is slightly worse [92].

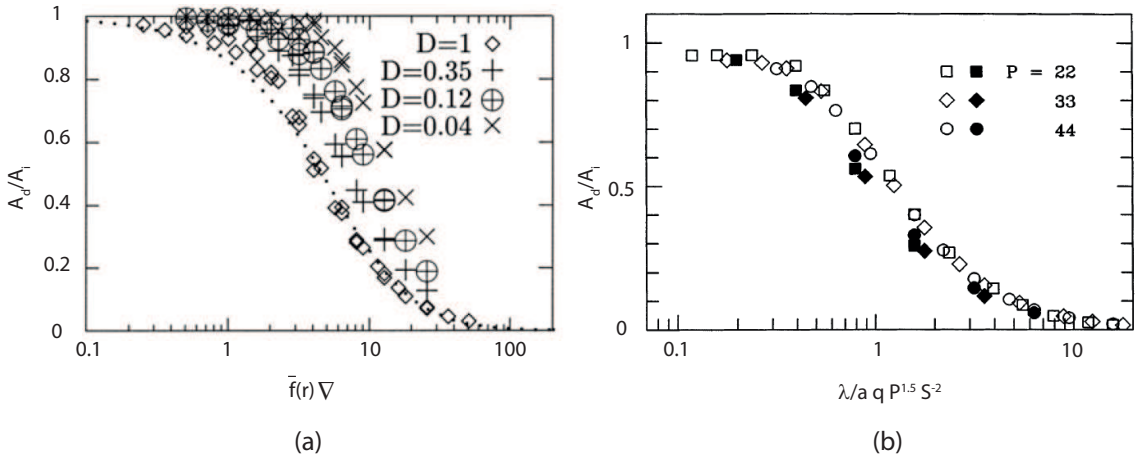

Fig. 2.15 (a) Amplitude reduction model and the effect of ellipticity on the behavior of a transverse surface pattern [91]. (b) Analysis demonstrating the similar roughness behavior in line and point contacts [92].

Jacod [93] extended the amplitude reduction model to the non-Newtonian line contact problem where a one-sided waviness was studied as a function of the slide to roll ratio (SRR). Under rolling-sliding conditions the wavelengths are different inside and outside the contact zone. For negative SRR (the wavy surface is slower) the curves are similar for both the Newtonian and Eyring models, however, this is not the case when SRR is positive. For the Eyring model there is an increase in deformation, while for the Newtonian the opposite trend can be observed. Increasing the shear stress value in the Eyring model the shape of the amplitude reduction curve

reverts gradually into the Newtonian curve. Authors showed that Non-Newtonian effects may change significantly the velocity profile.

Figure 2.16 shows the amplitude reduction curve as a function of the SRR for fluids with different shear stress values and also for the Newtonian model.

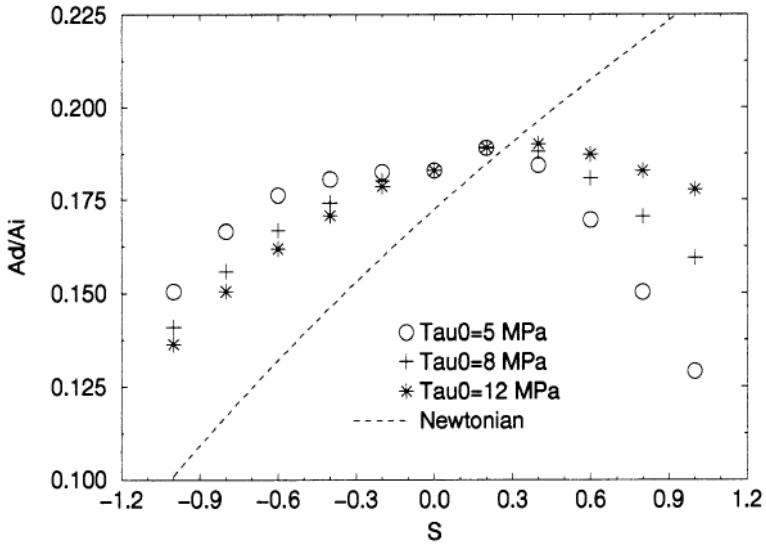

Fig. 2.16 Amplitude reduction curve as a function of the SRR for fluids with different shear stress values and also for the Newtonian model [93].

Chapkov [94] presented a derived amplitude reduction formula under non-Newtonian conditions. He observed that for heavily loaded contacts, the variations of the roughness wavelengths are more important. With increasing SRR the pressure induced flow is larger, therefore the roughness amplitude increases inside the contact. With increasing limiting shear stress value a linear relation between the shear rate and the stress value is obtained. The existing Newtonian amplitude reduction model can be extended to a non-Newtonian model.

2.5.2 Perturbation approach

Hooke [95] analyzed the behavior of low amplitude roughness. The passage of such a feature would cause several effects inside the conjunction. Hooke [95] names the following effects: "*the amplitude of the roughness itself may be reduced by hydrodynamic pressures accompanied by a phase difference between the original and the reduced roughness. Further, the roughness changes the conditions in the inlet generating a complementary wave traveling with the entrainment velocity. This complementary wave may decay as it passes through the conjunction.*" The third effect mentioned by Hooke are the pressure ripples associated with the roughness and the complementary wave. In Figure 2.17 the above mentioned characteristics are demonstrated.

The roughness behavior for different non-Newtonian fluids was studied and compared to the Newtonian model in [96]. For smooth contacts (Figure 2.18) there is little difference between the Newtonian and Eyring model. The values of the central

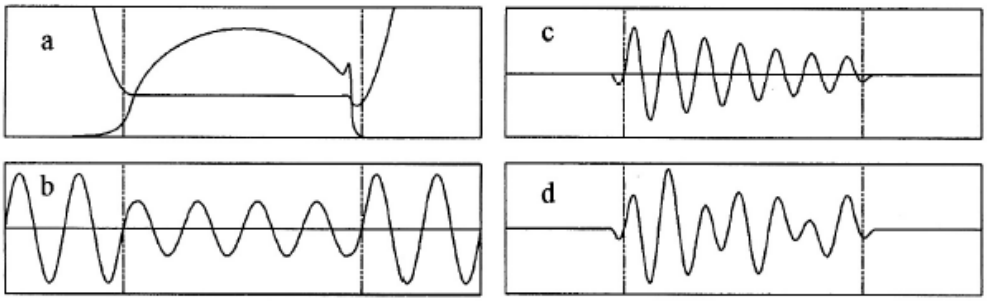

Fig. 2.17 Behaviour of roughness in an EHL contact under rolling-sliding conditions: (a) smooth pressures and clearances; (b) attenuation of surface roughness; (c) generation of complementary wave in the inlet; and (d)pressure perturbation at the inlet [95].

H_c and minimum H_{min} film thickness are reduced only slightly by the shear effects, the pressure spike is eliminated.

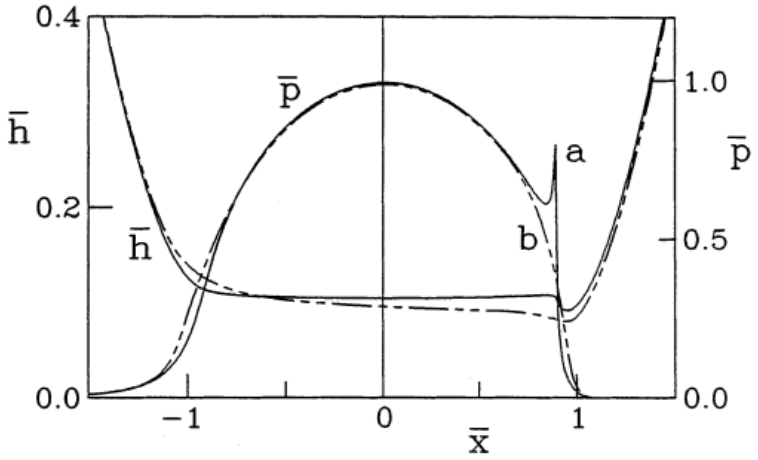

Fig. 2.18 Comparison of the Newtonian and Eyring model for a smooth contact [96].

Shear rate effects are relatively unimportant for pure rolling conditions but have a major influence when sliding is present. The formation of the complementary wave is largely eliminated and at short wavelengths the roughness passes through the contact unchanged. Under sliding conditions and assuming a Newtonian fluid large flattening is predicted for all the wavelengths. Figure 2.19 demonstrates that major differences appear between the two models when roughness is present.

Under non-Newtonian conditions, the amplitude of the clearance perturbation is small for wavelengths that are long compared to the entrainment pressure sweep. As the wavelength is reduced, the amplitude ratio increases and at short wavelengths the rough surface passes unchanged through the conjunction. Hooke compared the Eyring and the limiting shear stress models, concluding that the roughness behavior is not very sensitive to the exact nature of the non-Newtonian characteristics. There is a broad similarity between the results for a wide range of Eyring shear stresses in Eyring fluids and between the Eyring and limiting shear stress fluids. The amplitude reduction curve is presented for the different fluid models in Figure 2.20.

The perturbation approach aims to serve as a predictive model. Hooke assumes linear response of the contact to the low amplitude roughness which enables to

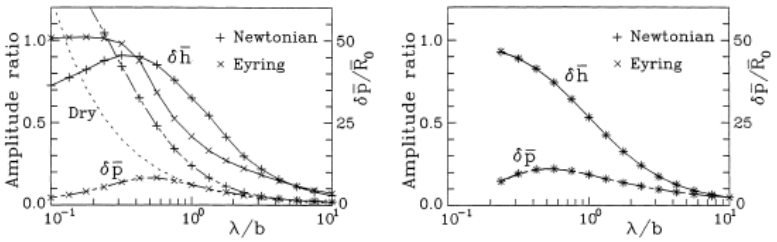

Fig. 2.19 Variation of the clearance and pressure perturbations with wavelength: rough surface sliding (left); and pure rolling (right) [96].

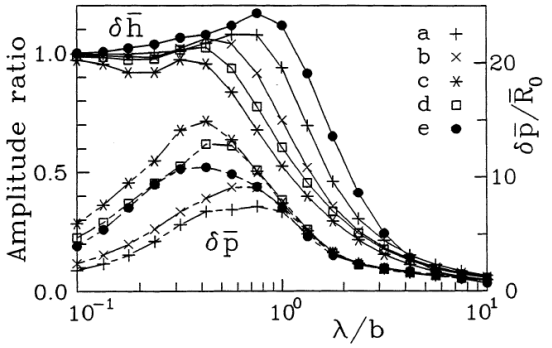

Fig. 2.20 Effect of the non-Newtonian characteristic: (a) Eyring $\tau_0 = 1$ MPa, (b) Eyring $\tau_0 = 2.9$ MPa, (c) Eyring $\tau_0 = 9$ MPa, (d) Eyring $\tau_0 = 0.0053p + 1.1 \times 10^6$ Pa, (e) limiting shear stress $\tau_L = 9$ MPa [96].

describe each roughness component separately. A single roughness component can be expressed in a complex form. The undeformed surface roughness would produce a sinusoidally varying clearance variation. The perturbation approach was described by Hooke e.g. in [97] where the attenuation of the roughness and the decay and the amplitude of the complementary wave were studied separately. The low-amplitude roughness is defined as

$$\delta r = A\cos\left(\omega(x - vt)\right)\cos(\xi y) \tag{2.53}$$

or in complex form as

$$\delta r = A\exp i\omega x \exp i\left(\xi y - v\omega t\right)) \tag{2.54}$$

with the velocity of the rough surface v. The roughness produces pressure perturbations

$$\delta P = P(x)\exp i\left(\xi y - v\omega t\right) \tag{2.55}$$

which will deform the surfaces

$$\delta w = W(x)\exp i\left(\xi y - v\omega t\right) \tag{2.56}$$

The deformation δw will modify the original profile giving rise to a residual roughness

$$\delta h = H(x)\exp i\left(\xi y - v\omega t\right) \tag{2.57}$$

where $H(x) = R(x) + W(x)$.

The magnitude of the roughness reduction caused by the pressure variations is given as

$$\frac{h_a}{A} = \frac{1 - iCQ}{1 - iQ - iCQ} \tag{2.58}$$

with $C = hE_r\kappa/4B$ representing the effect of compressibility. The attenuation parameter Q is given as

$$Q = \frac{6}{\pi^2}\frac{\eta\Delta u\lambda^2}{E_r h^3}\frac{\cos(\phi)}{\cos^2(\phi) + V\sin^2(\phi)} \tag{2.59}$$

The real part of equations represents the in-phase component, while the imaginary part the out-of-phase component. Parameter B stands for the bulk modulus of the fluid at the operating pressure, h is the film thickness and Δu the velocity difference between the surfaces [97]. The non-Newtonian Eyring model is used in the analysis, V expresses in Equation (2.59) the ratio of the effective viscosities, which are given by Ehret's analysis [43].
The decay of the complementary wave has the form

$$\delta h_c = h_c \exp i(\psi x + \xi y - \omega v t) \tag{2.60}$$

where $\psi = \omega_d + i\alpha$ with the wavenumber of the complementary wave ω_d and the rate α at which it decays [97]. An equation for the complex wavenumber ψ can be obtained after substituting into the Reynolds equation.

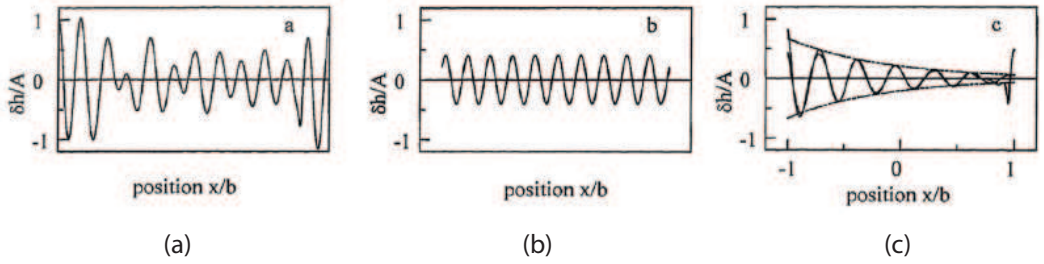

Fig. 2.21 Calculation of the amplitude of the complementary wave: (a) clearance variations obtained from the perturbation analysis, (b) attenuated clearance, and (c) full line - residual clearance variation after subtracting (a) from (b) [97].

The evaluation of the wavenumber and the decay rate of the complementary wave can be done by a simplified analysis. This is not the case when the amplitude of the complementary wave has to be obtained. The calculation of the complementary wave amplitude is illustrated in Figure 2.21. At an instant of time the amplitude of the complementary wave is obtained by subtracting the attenuated clearance (in the middle of the figure) from the clearance variations obtained from the perturbation analysis (top of the figure) [97].

Hooke stated that the low amplitude analysis appeared to give a good approximation both under pure rolling and rolling-sliding conditions. For pure rolling there is no roughness attenuation by sliding and the behavior of the roughness is determined by the conditions generated at the inlet. Under rolling-sliding the roughness

attenuation by sliding is important and the overall behavior is influenced by the complementary wave too. Under these conditions the non-Newtonian characteristics of the fluid control the roughness behavior [97].

2.5.3 Simulations with non-Newtonian models

Examples of full numerical simulations of a roughness feature passing through the contact zone were already given in Section 2.4. The majority of early works assumed Newtonian fluid behavior concluding that it gives sufficiently accurate results, differences were explained by the neglect of thermal effects and by the error caused by discretization.

In [98] full numerical solution of a mixed lubrication point contact model was published. The authors developed a novel method which is capable of treating measured rough surfaces. They applied the Eyring model, and for the low viscosity values the Barus relation. Several cases were tested for a wide range of mean velocities in order to cover all the lubrication regions. Film thickness distributions were compared under pure rolling and simple sliding conditions. For each speed the λ-ratio was smaller under simple sliding conditions. This is due to the shear-thinning effect of the non-Newtonian lubricant model.

Under pure rolling conditions the authors believe the squeeze term to play an important role. The roughness enhances the squeeze term and this results in higher film thickness values compared to the smooth case. Further, it is noted that due to shear thinning, sliding would provide another negative impact on the film thickness causing larger deformation, and consequently more surface failure.

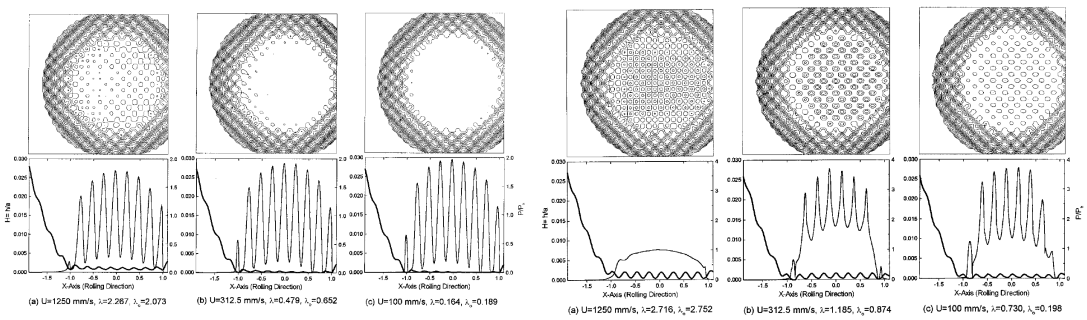

Fig. 2.22 Film thickness under simple sliding and pure rolling [98].

Figure 2.22 illustrates film thickness distributions assuming isotropic features under simple sliding (first three figures on the left) and pure rolling conditions (last three figures on the right).

Felix-Quiñonez et al. [99] compared the experimentally observed behavior of a single flat-top transverse ridge with full numerical simulations under rolling-sliding conditions. Three cases of simulations (pure rolling, negative, resp. positive sliding) were carried out and compared with the experiments. During experiments additional deformation of the ridge in the high-pressure region under sliding conditions was observed. The ridge was accompanied by an entrapped amount of lubricant during its passage through the conjunction. Simulations showed that under pure rolling the Newtonian model is sufficiently accurate - see the left part of Figure 2.23. However,

the introduction of negative, or positive sliding resulted in more complex situation. The effect of the lubricant rheology can be clearly observed for the sliding cases. The Eyring model yields better agreement with the experiments. It is able to reproduce the magnitude and shape of the film thickness variations. The Newtonian, on the other hand, predicts a more deformed ridge for positive sliding (middle part of Figure 2.23).

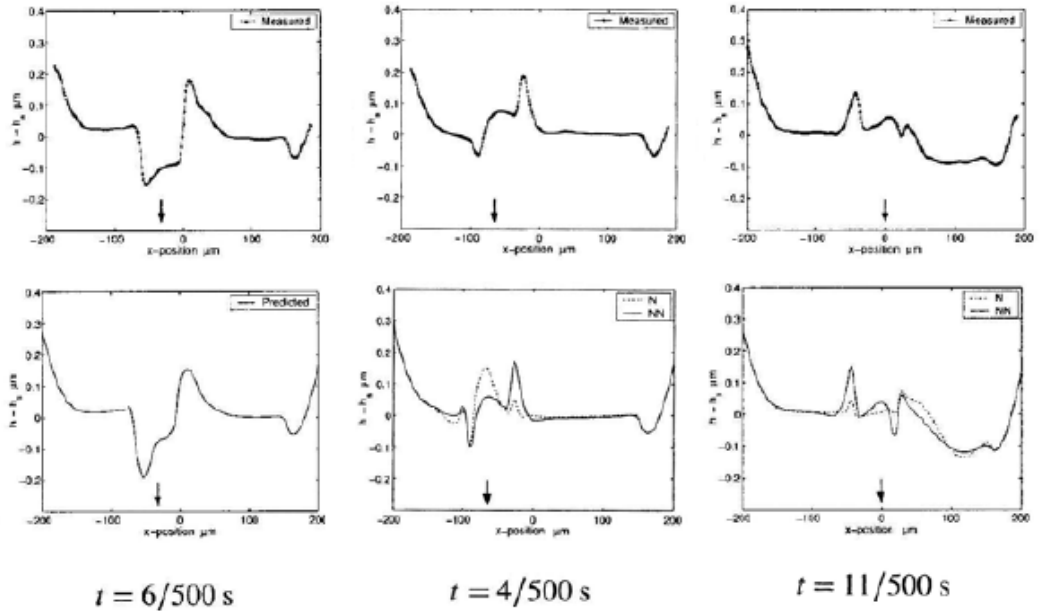

Fig. 2.23 Ridge deformation under pure rolling (left), negative SRR (middle) and positive SRR (right) [99].

While for positive sliding the ridge produces a forward-tilted shape, for negative sliding the opposite shape can be seen. Again, the Newtonian model is unable to reproduce the enhanced amount of lubricant just behind the ridge - see the right part of Figure 2.23. The pressure gradients are higher for the Newtonian model for both sliding conditions - see Figure 2.24. The study further indicates that the shape of the ridge plays an important role in the lubricant accumulation. In contrast to a Gaussian shaped ridge [100], a sharp-edged flat-top roughness produces larger pressure gradients and hence higher lubricant accumulation.

Another comparison of the rheology models and their effect on the roughness deformation is given in [101]. The effect of temperature was studied as well. Four models were considered in the simulations: the isothermal and thermal Newtonian, resp. the isothermal and thermal Eyring model. The results indicate that for small wavelength waviness the film thickness depends strongly on the lubricant rheology. The thermal Eyring model predicts larger pressure fluctuation and roughness deformation than its isothermal counterpart. The choice of the fluid model influences strongly the magnitude of pressure fluctuation. A big difference can be observed in the amplitude reduction of small wavelength roughness between the four models - see Figure 2.25. It can be seen in the figure that for the isothermal Eyring model the reduction is small and increases with increasing wavelength contrary to the other three models which predict opposite trends. The authors conclude that

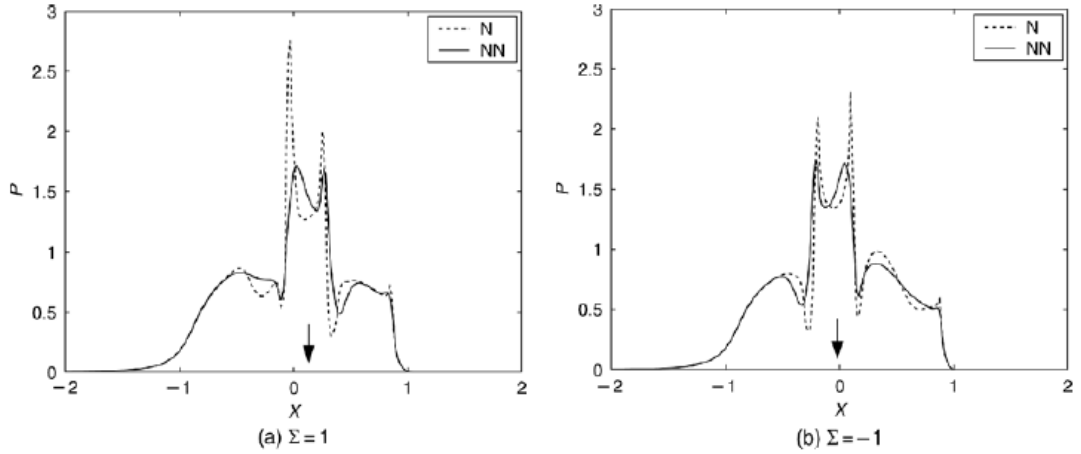

Fig. 2.24 Pressure distributions for different SRR - comparison between the Newtonian and non-Newtonian models [99].

with increasing roughness wavelength its deformation is hardly dependent on the fluid flow model and its amplitude.

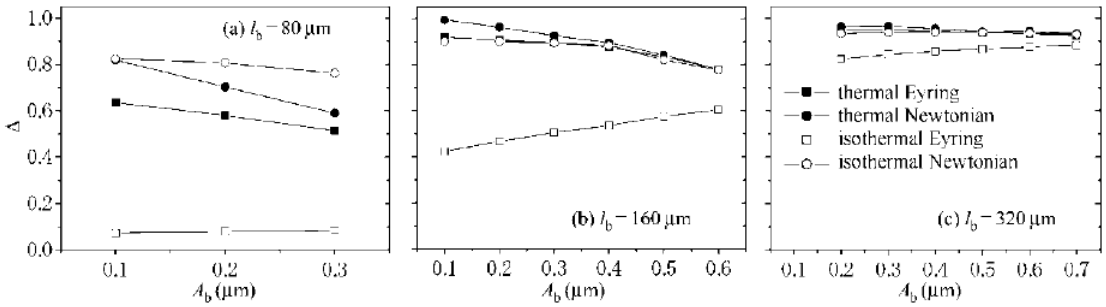

Fig. 2.25 Amplitude reduction of small wavelength roughness between four models (isothermal and thermal Newtonian, isothermal and thermal Eyring) [101].

In [102] the effect of different discretization schemes, viscosity and shear thinning models on the rough point contact model was studied. The authors found that the Yasutomi model predicts the best numerical results. The comparison of the rheology models (Newtonian vs. Eyring) led to the same conclusions as stated previously in the current section. Figure 2.26 shows that the agreement with the experiments is better with the Eyring model. Furthermore, the need of second order discretization scheme is emphasized.

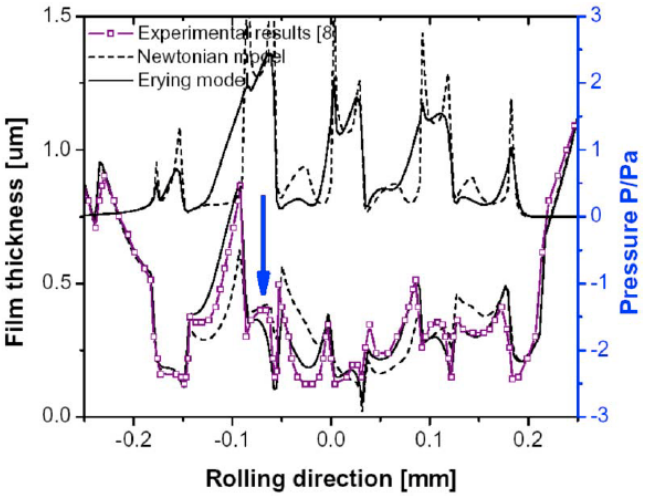

Fig. 2.26 Effect of rheological model on the film thickness [102].

2.6 Numerical methods

In what follows, a review of the numerical methods used for modeling the EHL problem is given. The first full numerical solutions were presented at the end of 1950's. Solutions were available first for the one-dimensional line contact problem, later for the more complex two-dimensional point contact (resp. elliptical) problem as well.

As first the direct and the inverse methods are presented. The difference between the two approaches is in the treatment of the Reynolds equation. Mutual feature of the methods is that they both have to solve simultaneously the Reynolds, the film thickness and the force balance equations.

2.6.1 Inverse method

The iterative scheme of the inverse approach is summarized by Venner [9]: "*For a given approximation of the pressure profile both the hydrodynamic film thickness and the film thickness based on the elastic deflections are calculated. Subsequently, the differences between those two results are used to adjust the pressure profile. This sequence is repeated until the hydrodynamic film thickness deviates less than some prescribed convergence criterion from the elastic deflection film thickness.*"

The first to use this scheme was Ertel [103]. Dowson and Higginson [49] solved the line contact problem by the inverse method in 1959, while Evans [104] extended the solution for point contacts.

The approach has several disadvantages, e.g. it is suitable just for highly loaded cases. Evans [104] used the inverse method for the Hertzian region, for the solution in the inlet region they used a direct method. Lubrecht [58] named another drawbacks such as the fact that the film thickness equation is rather insensitive to local variations in pressure. Finally, the Reynolds equation can not be integrated for the two-dimensional case, so the inverse method can hardly be adopted for the point contact problem.

2.6.2 Direct method

Lubrecht [58] described the direct method as the following: "*In the direct method, the Reynolds equation is solved for the pressure, for a given film thickness. The resulting pressure distribution is then used to calculate a new film shape, through the elastic equation, and so on, until a convergence is obtained.*" This approach was used for example by Hamrock and Dowson [54], Chittenden et al. [105] or Hamrock and Jacobson [106].

The Gauss-Seidel relaxation method is one of the direct algorithms used by e.g. [54] or [106]. The advantages of this method were the straightforward cavitation condition implementation and the small storage capacity. On the other hand, it has several disadvantages like the slow process of asymptotic convergence, or the overall complexity requiring $\mathcal{O}(n^3)$ operations assuming n nodes. Furthermore, it is not suitable for highly loaded cases, and in order to stabilize the process, underrelaxation factors are necessary which decrease the convergence speed [9].

Okamura [107] presented his solution using the Newton-Raphson technique. This method involves linearization, followed by a matrix inversion, generally performed by an accurate standard routine [58] (such as the Gaussian elimination method). The method has the following advantages: small number of iterations, fast convergence in the neighborhood of the solution and small computing times when assuming small number of grid points. The method was applied e.g. by Houpert et al. [56]. Although the advantages in the case of line contact are evident, the method cannot be implemented for the point contact. The reasons are the following: the inversion of the Jacobian matrix is very time consuming since the members of the matrix are non-zero due to the elastic deformations. The treatment of the cavitation condition is also troublesome, see [9] for more details.

The above discussed methods have their limitations, it is not possible to solve highly loaded or more complex problems accurately. These facts resulted in a diametrically different approach which will be presented in the next section.

2.6.3 Multilevel techniques

The concept of multilevel (multigrid) fast solvers is based on a certain understanding of the nature of errors in slowly converging iterative schemes [58]. The multigrid methods developed among others by Brandt [108], were first applied to the stationary EHL line and point contact problem by Lubrecht [58]. He solved the Reynolds equation using the Gauss-Seidel relaxation algorithm and increased the convergence rate applying the multigrid technique. The multigrid method is based on the understanding of the convergence behaviour of the Gauss-Seidel relaxation process. It can be shown that error components with a wavelength of the order of the mesh size, i.e. high frequency components, are efficiently reduced by the relaxation process [9]. Contrary to this, the error components with wavelengths much larger than the mesh size are hardly reduced and consequently, after a few iterations convergence slows down and the asymptotic convergence rate becomes very small [9]. The remaining error can be sufficiently solved on a coarser grid on which its size is comparable to the coarse mesh size. Instead of continuing the iterative relaxation process, the solution is moved to a coarser grid. After obtaining an acceptable approximation of

the error on the coarse grid, the error is transferred back to the fine grid to correct the solution on the fine grid. By applying the multigrid method the computational cost of iterations and the work needed for the solutions of the error is reduced due to the fewer nodal points on the coarse grids. The iterative process converges faster on the coarse grids. Although, the solution of the Reynolds equation was faster with the multigrid method, the complexity of the whole EHL problem was still $\mathcal{O}(n^2)$ due to the elastic deformation integrals. Moreover, Lubrecht's algorithm was applicable only to stationary and lightly to moderately loaded contact problems.

Brandt and Lubrecht [109] developed the so-called multilevel multi-integration (MLMI) in order to reduce the computational time evaluating the elastic deformations. MLMI was incorporated to the EHL problem by Venner [9] reducing the complexity from $\mathcal{O}(n^2)$ to $\mathcal{O}(n \ln n)$ operations where n is the number of nodal points. Venner also introduced the distributive relaxation schemes in EHL allowing to solve highly loaded contact problems as well as the transient line contact case. More details about the multilevel techniques can be found in [108], [110], [111] and in [12] focusing on the smooth EHL problem.

The multigrid approach became very popular for solving EHL related problems. It is widely applied for different problems, such as the modeling of the passage of different types of surface features, thermal problems or starvation.

2.6.4 Finite element based solutions

The following part presents some of the finite element based solutions of recent years. Piccigallo [112] developed a method for thermal EHL line contact under non-Newtonian conditions. The Reynolds equation was solved applying the Galerkin method with a linear-interpolation finite element technique. Lu [113] provided the first solution of the EHL line contact by the discontinuous Galerkin method easily obtaining stability. Fatu [114] solved the thermo-elastohydrodynamic problem for dynamically loaded bearings. In the paper the two problems necessary to define the finite element method (FEM) formulation for the EHD problem are given: the first problem states that the film thickness is known and the active-nonactive film-zone separation boundaries are sought. The first problem is solved applying a modified Reynolds equation. The second problem says that the active and nonactive film position is known, and the film thickness and pressure (which verify the Reynolds equation) and the elastic equations are sought. This problem is solved by the classical Reynolds equation and the relation between the film thickness and hydrodynamic pressure. Both problems have to be solved at each time step. The Newton-Raphson method is used to solve the discrete equations. A heat flux conservation algorithm is proposed in the paper to solve the temperature. Transient calculation using a FEM formulation can be found e.g. in [115] concluding that the precise analysis shows better accuracy for the boundary definition of the cavitation zone.

Habchi [116]-[117] presented an adaptation of classical algorithms for solving the EHD point contact problem. He used FEM to solve the Reynolds equation allowing him to drastically reduce the number of degrees of freedom compared with the classical finite difference discretization of the Reynolds equation. The problem was coupled with the use of the Boussinesq's theory to evaluate the elastic deformations.

In [117] three different FEM formulations were compared in order to analyze their stability properties.

Analyses based on commercial software (e.g. ANSYS) are also available, see e.g. [118] where a finite element implementation by the software ABAQUS is shown for the computation of mixed lubrication effects in soft EHL contacts.

2.6.5 Finite volume based methods

Čermák [120] employed the control volume approach to obtain an appropriate discretization scheme for the two-dimensional Reynolds equation. The calculation domain was divided into a number of non-overlapping control volumes and the flow-field variables were calculated at grid points within the control volumes integrating the differential equation over each control volume. Čermák reported decreased dependence of results on the grid density compared to the results obtained with the finite difference formula. Lu [121] provided a comparison of two different diffusion schemes used for solving the Reynolds equation through the control volume method in which only one scheme proved to be useful for the smooth EHL line contact problem.

Commercial computational fluid dynamics (CFD) softwares are applied to the EHL problems too. Almqvist [122] replaced the Reynolds equation by the Navier-Stokes (N-S) equations and employed a forward-iterative coupling between the flow and deflection. Solutions were obtained for the smooth thermal EHL line contact problem up to a pressure of approximately 0.7 GPa. Almqvist claimed that by solving EHL problems on the basis of N-S equations offers the possibility of expanding the computational domain in both the inlet and the outlet regions of the contact meaning that no thin film approximations have to be performed and the inertia terms are also retained. Almqvist described a different well working treatment of the cavitation condition by modification of the density. Since the pressure is not an independent equation in the N-S approach, the pressure gradients contribute to the three momentum equations, and the contact problem becomes a very computer-intensive task. Another shortcoming of the commercial CFD software is the use of very small under-relaxation factors resulting in a slow convergence rate. A comparison of Reynolds and CFD approaches of transverse non-Newtonian EHL line contact model is given in [123] showing small deviations between the two approaches assuming that the amplitude to wavelength ratios are small as well. Another comparison of the two above mentioned approaches is made by Hartinger et al. [124]. They used a finite volume based commercial software defining the EHL problem as a combination fluid and solid models. Hartinger states that the advantage of CFD is the ability to resolve all the velocity, viscosity and pressure gradients across the film compared to the Reynolds approach where these gradients are simplified or missing. Furthermore, the CFD can model the entire fluid system compared to the limited near-parallel region of the Reynolds approach. A third advantage of the CFD is the implementation of complex fluid properties, so that any kind of dependency on pressure, temperature, shear-rate, or any other variable can be studied [124]. Despite their advantages the CFD models are limited to the lightly or moderately loaded problems and the computational time is too long as well.

2.6.6 Other approaches

This section gives a summary of the rest of the numerical techniques providing solutions to different EHL problems. Several approaches were designed in order to increase the calculation speed of the elastic deformations or in order to incorporate real rough surface data to the computational models. Some of the presented solutions use the combination of different numerical methods.

Polonsky et al. [125] proposed an alternative numerical method for solving contact problems for real rough surfaces. Their algorithm combines the conjugate gradient method (CGM) to determine the real contact area and pressure distribution with the MLMI to calculate the deformation. The use of CGM for rough contact problems is based on rigorous convergence theorems and is described in detail in the paper. The presented method converges for arbitrary rough surfaces and allows to simulate surface samples with $\mathcal{O}(10^5)$ - $\mathcal{O}(10^6)$ data points in a few hours.

Hu et al. [126] presented in their work full numerical solution for the contact of elastic bodies with a general geometry and three-dimensional roughness. They defined the elastic contact as a linear complementarity problem and solved it by the conjugate gradient method which resulted in a very stable and robust solution.

The Fourier transformation of the elastic equations by means of its discrete numerical form serves as alternative to MLMI. These two approaches were compared in [127] stating that when the problem is periodic the inverse Fourier transform must be used yielding a solution up to machine precision. However, if the problem is not periodic the MLMI provides a solution with the same accuracy. The advantage of the MLMI is its uniform convergence behavior over the complete calculation domain. The fast Fourier transform (FFT) can have the same convergence behavior but a larger calculation domain is required and thus it results in longer computing times [127]. On the other hand, the implementation of FFT can be very simple and short, while the MLMI requires much longer routines. Another comparison of the FFT and MLMI came to similar conclusions, namely that the MLMI technique is more advantageous than FFT for solving three-dimensional concentrated contact problems, both when the maximum possible accuracy is desired and when a moderate accuracy goal is specified [128].

Polonsky and Keer [129] showed an attempt to overcome the periodicity problem of the FFT by introducing a special correction procedure based on the MLMI. This procedure combined with the conjugate gradient method allowed to solve concentrated contact problems for layered solids with real rough surfaces as well as it enabled to study the effect of protective coatings on contact fatigue and other failure modes of engineering surfaces.

Hu et al. [130] applied the FFT in their model in order to reduce the computing times encountered in full numerical deterministic models of rough EHL problems. They work with the assumption that any three-dimensional surface roughness can be decomposed into a series of sinusoidal waves with different wavelengths and orientation angles. Following another assumption saying that each elemental wave causes a sinusoidal pressure fluctuation with the same frequency and orientation angle, authors derived and EHL system model and an input-output relationship consisting of five constants determined through fitting numerical results for 50 cases. The model can then be solved by means of FFT resulting in an estimation of pressure for full

EHL or mixed lubrication within a few seconds [130]. Unfortunately, the results show that this type of pressure estimation is in agreement with the full numerical solutions only for few cases.

Liu et al. [131] developed a model for coated EHL point contacts in which they combine the elastic deformation formulation for coated surfaces with the EHL model. They use the inverse fast Fourier transform to obtain the influence coefficients from a frequency response function and subsequently the elastic deformation is calculated by an efficient algorithm combining discrete convolution and fast Fourier transformation. Another examples of the FFT based solutions are e.g. [132] or [133], where the subsurface stress and contact pressures are analyzed.

A fully coupled iterative solution of the transient point contact was presented by Holmes et al. [134]. The full coupling was achieved by the use of a novel differential deflection formulation. The authors compared several discretization schemes among which the finite element based spatial discretization together with the standard Crank-Nicholson discretization of the time-dependent term proved to be the most effective. Their paper describes in detail the above mentioned method and a second part [135] presents results of a non-Newtonian rough EHL point contact model obtained by this approach.

3 ANALYSIS AND CONCLUSION OF LITERATURE REVIEW

The study of the effects of roughness inside an EHL point contact can be divided into theoretical and experimental works. The previous chapter focused on theoretical works and reviewed the most important publications dealing with full numerical simulations and analytical predictions of roughness behavior and deformation under different operating conditions and fluid properties.

The early numerical simulations considered stationary models of the smooth EHL contacts revealing several characteristics such as the horse-shoe shaped film thickness distribution confirming the experimental observations, the empirical central and minimum film thickness formulas, or the pressure distribution with its shape similar to the Hertzian dry contact pressure distribution and the second local maximum, the so-called pressure spike. The empirical formulas [54] are still widely used and serve as a reference value although their applicability is rather suitable for lightly loaded contact problems. It was shown that the phenomena of the pressure spike is an issue related to the numerical solution [58], it's magnitude depends on the load and on the choice of the pressure-viscosity relation.

The progress in computational techniques gave rise to more advanced calculations. The use of novel numerical methods yielded stable, fast and accurate solvers for the EHL problems. The introduction of the multilevel techniques greatly reduced the computational complexity of the EHL model and enabled to solve time-dependent problems as well. The multigrid method was applied to solve the Reynolds equation together with the multilevel multi-integration to calculate the elastic deformations. For n grid points the overall complexity was reduced from $\mathcal{O}(n^3)$ to $\mathcal{O}(n \ln n)$ operations [12]. Other alternatives are finite element [116] or finite volume [123] based models (commercial software as well) or the combination of several numerical methods. For example, the fast Fourier transformation enables to calculate the pressure and film thickness for arbitrary rough surfaces [130]. The choice of the discretization scheme and order plays an important role in the modeling. For the transient problem all members of the Reynolds equation should be discretized by second order manner so accurate results can be obtained [125].

The assumption of smooth surfaces in an EHL contact is rather theoretical. Real machine components encounter surface roughness which is defined by statistical parameters. The complexity and uniqueness of each surface profile causes that it is hard to incorporate them to the theoretical models and deduce a generalized method. The statistical approach [70] introduced in the 1970's seems to be inaccurate since it did not assume the elastic deformation of the asperities. On the contrary, the deterministic approach is able to handle different surface features. Studying the models with surface roughness we can conclude the following:

- The roughness can be incorporated into the numerical model by assuming artificial surface features or real surface roughness.
- Contact problems with real rough surfaces are hard to model due to the uniqueness of each rough surface, solutions were given e.g. by [128]-[129]. In [125] surface samples with $\mathcal{O}\left(10^5\right)$ - $\mathcal{O}\left(10^6\right)$ data points were modeled with the conjugate gradient method. Another approach used to model real surfaces is the

fast Fourier transform [130].

- Artificial surface features can be classified as local (dent, bump) or global (waviness) or the combination of these two which are local in one dimension, but global in the second one (such as a ridge, scratch, furrow) [86]. The majority of works uses harmonic functions to describe these features.
- The first deterministic models assumed stationary problems, i.e. the asperity was fixed at a certain location. Lubrecht [58] showed that the influence of the asperity on the pressure and film thickness is proportional to its amplitude and wavelength. For high loads the asperities are flattened out due to the Couette flow causing only small changes in the film thickness, while for low loads the opposite process can be observed. This fact was explained by the reduction of the Reynolds equation to the transport equation.
- Since in an EHL contact generally both surfaces move, time-dependent models are necessary to consider. The role of the squeeze term in the Reynolds equation can not be neglected [9]. The pressure flow will be absent inside the contact resulting in a shear flow dominated solution. Both stationary (the feature is fixed at a given location) and transient simulations were carried out for a dent revealing the differences caused by the squeeze term: the pressure rise is not symmetrical for the transient case at the leading and trailing edges of the dent, and an additional amount of fluid is entrapped in the dent shifting through the contact zone. The presence of the squeeze term implies that the geometry of the feature will be preserved during the time it moves through the contact zone.
- Unless the feature is longitudinally orientated, time-dependent simulations are necessary.

Major differences can be seen in the behavior of the roughness feature under pure rolling (the two surfaces have the same velocities) and under rolling-sliding conditions (different velocities of the surfaces):

- Differences between the stationary and transient simulations are more distinct for sliding contacts.
- It was shown that for pure rolling once the feature is inside the Hertzian zone, it tends to undergo only slight changes, however, under sliding the film thickness variation (Equation (2.43) states that it travels with the mean velocity) is independent of the feature's velocity. Venner argued [9] that in order to keep the mass conversation in the flow, the system has to move the trapped fluid through the contact by means of the Couette flow, i.e. film thickness variations.
- An asynchronism can be observed between the film thickness and pressure variations under rolling-sliding, the two components of the solution can be distinguished [80]-[83].
- Greenwood and Morales-Espejel [85] defined these two separate parts as the particular integral (moving steady state solution) and the complementary function. The first one generates large pressure and small film thickness variations traveling with the velocity of the surface roughness. The second one is caused due to the inlet modulations of the film resulting in large film thickness and small pressure variations traveling with the mean entrainment velocity.

Surface features deform inside the contact as they pass through it. The magnitude

of this deformation depends on several factors:

- Besides the full numerical simulations, different (predictive) analytical approaches such as the amplitude reduction model [88] or the perturbation analysis [95] were presented in order to study the deformation.
- The deformation is expressed as the ratio of the undeformed (initial) roughness amplitude to the deformed amplitude, it depends on the operating conditions and on the wavelength of the roughness. A single parameter can be derived relating the above mentioned parameters to each other.
- The results indicate that features with long wavelengths are almost completely flattened out, while short wavelength components hardly sustain any deformation [88].
- The slide to roll ratio (SRR) influences the shape of the amplitude reduction curve too, the parameter expressing the deformation has to be modified so the the effect of SRR is included [88].
- The point contact case is somewhat more complicated compared to the one-dimensional case, however, it is possible to create a single curve for all types of harmonic features (defined by their wavelengths in both directions) [91].
- It was shown that the roughness follows similar behavior for both types of contacts (line and point contacts).
- Hooke [97] studied not only the magnitude of the deformation, but also the characteristics of the complementary function (its amplitude and decay).

The fluid properties, especially the rheology model plays an important role in the simulation of roughness behavior. The early numerical works assumed Newtonian fluid behavior, although this assumption was questioned later for several reasons:

- Under pure rolling conditions and for smooth surfaces the differences between the Newtonian and non-Newtonian behavior are negligible.
- Under rolling-sliding conditions the Newtonian fluid model failed to explain the experimentally measured traction curves [30], and a non-linear dependence between the shear stress and shear rate of the fluid is expected.
- The incorporation of the different rheological functions (2.23)-(2.29) into the two-dimensional Reynolds equation is in general complicated. For line contact problem the expressions for the effective viscosities can be derived relatively simply and full numerical solutions are available [42]-[47]. On the other hand the derivation of the effective viscosities for the point contact problem is not straightforward. The generalized Newtonian approach might serve as an alternative [48].
- The time-consuming integrations of (2.31) across the film thickness can be replaced by simplifying the expression of the rheological function (Eyring law) for the point contact problem. The exact derivation of these expressions can be found e.g. in [30] or [43]-[45].
- The amplitude reduction model can be extended to the non-Newtonian model as well [93]-[94]. It shows that for a faster wavy surface the deformation of the feature increases with the Eyring model, while for the opposite case the two fluid models behave similarly. Increasing the Eyring stress value τ_0 the curve gradually reverts into the Newtonian curve.
- Hooke's analysis [96] proved that major differences between the Newtonian and

non-Newtonian models can be seen under sliding conditions. With the Newtonian fluid large deformations are predicted for all the wavelengths. Moreover, Hooke stated that the roughness behavior is not very sensitive to the exact nature of the non-Newtonian characteristics.

- Full simulations [99]-[102] also indicate the differences between the Newtonian and non-Newtonian models. Again, for pure rolling the Newtonian model is sufficiently accurate. Under rolling-sliding conditions the non-Newtonian model yields better agreement with the experiments.
- The Eyring sinh law (2.23) is applied in the majority of simulations with point contacts.
- The Newtonian model predicts a more deformed ridge and is unable to reproduce the entrapped amount of lubricant behind or in front of the ridge.
- It was shown in [101] that for small wavelength roughness the film thickness depends strongly on the lubricant properties, with increasing roughness wavelength its deformation is hardly dependent on its amplitude and the fluid flow model.
- Although, the Eyring model is very widespread in the two-dimensional simulations of rough problems, e.g. its validity or the shear-thinning behavior was questioned by several authors, e.g. [35], [36], [48].
- The generalized Newtonian model represents an alternative approach to the accurate modeling of the EHL problem, however, this approach is derived only for the line contact case [48]. Further work needs to be done in order to extend it to two-dimensional time-dependent models.

4 AIMS OF THE THESIS

The aim of the dissertation is to study the effect of non-Newtonian lubricant properties on the behavior of surface roughness inside the contact zone under rolling-sliding conditions by means of numerical simulations. The problem solved in this work is very complex requiring time-dependent solution. Therefore, an accurate, fast and stable numerical method has to be chosen. The solution of the work has two stages, the first requires the development of the numerical solver. The second part consists of the simulations of the defined problem for different cases and its comparison and verification by experiments.

First part:

- development of the stationary EHL solver assuming Newtonian fluid model and smooth surfaces
- extension of the solver to time-dependent problems assuming the passage of surface features through the contact zone
- inclusion of the non-Newtonian fluid model into the solver

Second part:

- simulation and verification of the smooth contact EHL problem considering both Newtonian, and non-Newtonian fluid rheology
- simulation of the passage of surface feature under pure rolling, and rolling-sliding conditions assuming Newtonian and non-Newtonian fluid rheology models
- comparison with the results of experimental measurements

5 METHODS

The main governing equations describing the EHL point contact problem were presented in Section 2.1. The two-dimensional EHL model is very complex consisting of a partial differential equation of second order (the Reynolds equation (2.10)) and an integro-differential equation (the film thickness equation (2.17)). This model can not be solved analytically, it has to be transferred from a continuous form to a discrete one enabling its numerical solution. As it was outlined in Chapter 2, the solution of the model can be very time consuming, especially when assuming a transient model. A proper numerical method has to be chosen.

We can divide the current problem into two parts: the solution of the transient Reynolds equation and the solution of the elastic deformations. These include many computational operations in each time step. Brandt [108] states that: "*the amount of computational work should be proportional to the amount of real physical changes in the computed system.*" Bearing this in mind, the multigrid method in combination with the multilevel multi-integration are applied in the current thesis to solve the presented mathematical model.

The current chapter presents the mathematical model of the EHL problem and outlines the numerical method used to solve this problem. The governing equations and their dimensionless and discrete forms are described. At the end of the chapter implementation details are given.

5.1 Multigrid method

The multigrid method was first applied to the EHL problem by Brandt and Lubrecht [58]. The general principle behind the multigrid (MG) method is the use of several computational grids and the transfer of the relaxation problem between them.

Assuming a discrete problem of an elliptic differential equation on a given grid (such as the Reynolds equation) the relaxation process may exhibit a very characteristic behavior, i.e. high frequency components are reduced effectively whereas the low frequency components converge only slowly. The high frequency components are defined as those whose wavelength is of the order of the grid's mesh size. Assuming an arbitrary first approximation, the relaxation process might slow down after few iterations. In other words, after a relatively large error reduction of the high frequency components, the low frequency (smooth) components remain and cause the error reduction per relaxation to be very slow. The error is dominated by components with a wavelength that is large compared to the mesh size of the grid, i.e. the error is smooth on the scale of the mesh size [12]. This smooth error can be represented on a coarser grid with little loss of accuracy. Instead of continuing the relaxation process on the initial (*target*) grid, the MG method enables to solve it on a coarser grid where the remaining error can be smoothed. After the error is solved on the coarse grid it is interpolated back to the target grid. The equations for the coarse grid are derived from the fine grid equations and solved on the coarse grid. The process can be repeated until such a coarse grid is reached where a sufficiently accurate approximation of the problem is obtained.

The algorithm for the MG method can differ depending on the properties of the problem (linear or non-linear). For the linear problem the correction scheme is used (see [12]), the non-linear problem is more complicated and the full approximation scheme has to be applied. More about the multigrid techniques is available in [12], [108], [110] and [111].
The following section outlines the basic concept of the MG algorithm. Since the Reynolds equation (2.10) is non-linear the full approximation scheme (FAS) is presented and described. The description and notation of variables is based on the book [12].

5.1.1 Full approximation scheme

We can generally define a differential equation as

$$\mathcal{L}\left\langle u\right\rangle = f \tag{5.1}$$

with the continuous differential operator $\mathcal{L}$, the continuous unknown u and the continuous right hand side function f. The symbol $\mathcal{L}\left\langle u\right\rangle$ indicates that the operator $\mathcal{L}$ depends on the solution u and works on u [12]. The discrete equivalent of problem (5.1) defined on grid h is

$$\mathcal{L}^h\left\langle \underline{u}^h\right\rangle = \underline{f}^h \tag{5.2}$$

where the actual grid on which the problem is defined for n discrete points has a mesh size $h = 1/(n-1)$. The superscript in Equation (5.2) denotes the grid on which it is solved. An initial solution $\widehat{\underline{u}}^h$ of the unknown vector $\underline{u}^h$ is assumed. Problem (5.2) is relaxed on grid h and after a certain number of iterations an approximate solution $\widetilde{\underline{u}}^h$ is obtained. The numerical error $\underline{v}^h$ is obtained from the residual which is defined as

$$\underline{r}^h = \underline{f}^h - \mathcal{L}^h\left\langle \widehat{\underline{u}}^h\right\rangle \tag{5.3}$$

where $\underline{r}^h = \underline{0} \iff \underline{v}^h = \underline{0} \iff \widetilde{\underline{u}}^h = \underline{u}^h$.
The numerical error $\underline{v}^h$ is

$$\underline{v}^h = \underline{u}^h - \widetilde{\underline{u}}^h \tag{5.4}$$

Equation (5.4) is substituted into Equation (5.3)

$$\underline{r}^h = \underline{f}^h - \mathcal{L}^h\left\langle \underline{u}^h - \underline{v}^h\right\rangle \tag{5.5}$$

Since the operator $\mathcal{L}^h$ is non-linear the error cannot be treated separately from the solution and the full equation has to be used. Substitution of (5.3) and (5.4) into Equation (5.2) gives

$$\mathcal{L}^h\left\langle \widetilde{\underline{u}}^h + \underline{v}^h\right\rangle = \mathcal{L}^h\left\langle \widetilde{\underline{u}}^h\right\rangle + \underline{r}^h \tag{5.6}$$

Equation (5.6) is used to approximate the error on the coarse grid H. The coarse grid discrete problem is defined for the unknown $\widehat{\underline{u}}^H$ as

$$\mathcal{L}^H\left\langle \widehat{\underline{u}}^H\right\rangle = \underline{f}^H \tag{5.7}$$

where

$$\widehat{\underline{u}}^H = I_h^H\left(\widetilde{\underline{u}}^h + \underline{v}^h\right) = I_h^H\widetilde{\underline{u}}^h + \underline{v}^H \tag{5.8}$$

The intergrid transfer operators I_h^H and I_H^h will be defined in the following section. The coarse grid right hand side vector is

$$\underline{\widehat{f}}^H = \mathcal{L}^H \left\langle I_h^H \underline{\widetilde{u}}^h \right\rangle + I_h^H \underline{r}^h \tag{5.9}$$

for $\underline{r}^H = I_h^H \underline{r}^h = \underline{0} \iff \underline{v}^H = \underline{0}$. After the coarse grid problem is solved for a prescribed accuracy yielding a sufficient approximation $\underline{\widetilde{u}}^H$ of the problem $\underline{\widehat{u}}^H$, it is transferred back to the fine grid h. The previous approximation $\underline{\widetilde{u}}^h$ is then corrected

$$\underline{\overline{u}}^h = \underline{\widetilde{u}}^h + I_H^h \left(\underline{\widetilde{u}}^H - I_h^H \underline{\widetilde{u}}^h \right) \tag{5.10}$$

5.1.2 Intergrid transfers

In order to transfer the discrete problem to coarser grids and back, the operators of restriction and interpolation have to be defined:

- the restriction operator I_h^H ensures the transfer of the fine grid residual $\underline{r}^h$ to the coarse grid H,
- the interpolation operator I_H^h ensures the transfer of the coarse grid error $\underline{v}^H$ to the fine grid h.

It has to be noted, that throughout the solution, assuming a fine grid h with $n_x \times n_y$ grid points, a coarse grid mesh size will be $H = 2h$ with $(n_x/2) \times (n_y/2)$ grid points.

Restriction

We define the transfer of the residual from a fine grid h to the coarse grid H as

$$\underline{r}^H = I_h^H \underline{r}^h \tag{5.11}$$

The simplest type of restriction of an arbitrary vector in grid point (I, J) from a fine grid to a coarse grid is injection in which case the coarse grid point is taken as the value of the coinciding fine grid point. The injection operator can be expressed in a stencil notation as

$$I_h^H = \begin{bmatrix} 0 & 0 & 0 \\ 0 & 1 & 0 \\ 0 & 0 & 0 \end{bmatrix} \tag{5.12}$$

The coarse grid residual will be then

$$r_{I,J}^H = r_{2I,2J}^h \tag{5.13}$$

The so-called full weighting operator gives the coarse grid value as the weighted average of the values in the coinciding fine grid points and its neighbors (as shown on the left of Figure 5.1) and its stencil is denoted as

$$I_h^H = \frac{1}{4} \begin{bmatrix} 1 \\ 2 \\ 1 \end{bmatrix} \frac{1}{4} \begin{bmatrix} 1 & 2 & 1 \end{bmatrix} = \frac{1}{16} \begin{bmatrix} 1 & 2 & 1 \\ 2 & 4 & 2 \\ 1 & 2 & 1 \end{bmatrix} \tag{5.14}$$

Equation (5.13) becomes with the full weighting operator (5.14)

$$\begin{aligned} r_{I,J}^H = \big(& 4 r_{2I,2J}^h + 2 \left(r_{2I-1,2J}^h + r_{2I+1,2J}^h + r_{2I,2J-1}^h + r_{2I,2J+1}^h \right) \\ & + \left(r_{2I-1,2J-1}^h + r_{2I+1,2J-1}^h + r_{2I+1,2J+1}^h + r_{2I-1,2J+1}^h \right) \big) / 16 \end{aligned} \tag{5.15}$$

More about the restriction operators and their properties can be found in [12].

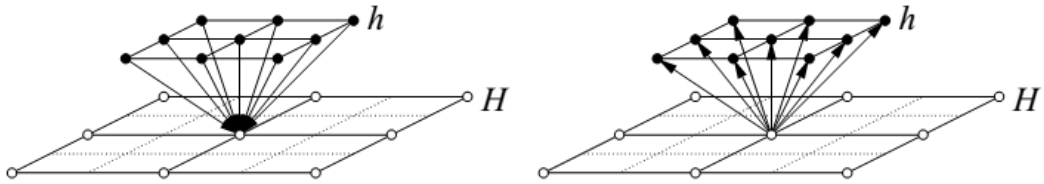

Fig. 5.1 The intergrid operators: restriction I_h^H (left) and interpolation I_H^h (right) operators [10].

Interpolation

The transfer of the coarse grid error to the fine grid is written as

$$\underline{v}^h = I_H^h \underline{v}^H \tag{5.16}$$

The interpolation operator for the two-dimensional problem is defined as (on the right of Figure 5.1)

$$I_H^h = \frac{1}{2}\begin{bmatrix}1\\2\\1\end{bmatrix}\frac{1}{2}\begin{bmatrix}1 & 2 & 1\end{bmatrix} = \frac{1}{4}\begin{bmatrix}1 & 2 & 1\\2 & 4 & 2\\1 & 2 & 1\end{bmatrix} \tag{5.17}$$

To interpolate the coarse grid error linear interpolation is sufficient because of the smoothness of the error, however, it is possible to derive higher order interpolations using the Langrange interpolation formula. Higher order interpolations require extra work due to the different non-central stencils needed close to the boundaries [12]. Using a pointwise description the stencil (5.17) becomes:

$$\begin{aligned} v^h_{2I,2J} &= v^H_{I,J} \\ v^h_{2I+1,2J} &= \left(v^H_{I,J} + v^H_{I+1,J}\right)/2 \\ v^h_{2I,2J+1} &= \left(v^H_{I,J} + v^H_{I,J+1}\right)/2 \\ v^h_{2I+1,2J+1} &= \left(v^H_{I,J} + v^H_{I,J+1} + v^H_{I+1,J} + v^H_{I+1,J+1}\right)/4 \end{aligned} \tag{5.18}$$

More details about the interpolation operators are in [12].

5.1.3 Multigrid cycles

The multigrid cycle is the combination of the above described tools (FAS, intergrid operators). Usually, the same relaxation procedure can be applied to the coarse grid equations as to the original fine grid equations. The fine grid is used to smooth the high frequency errors, while the coarse grids smooth the errors of low frequency until a grid is reached were the solution by relaxation becomes cheap, i.e. a very coarse grid with a small number of nodes, and the relaxation converges rapidly [12]. Venner and Lubrecht [12] refer to the grids as *levels* with the coarsest grid being level 1 and the finest grid being level k. A multigrid cycle is determined by three main parameters: ν_1, ν_2 and γ. The ν_1 relaxations serve to pre-smooth the error before coarsening, ν_2 relaxations are used for post-smoothing in order to remove the errors introduced by interpolation of the correction. The parameter γ defines how

accurately each coarse grid problem is solved before returning to the fine grid [12]. An additional parameter ν_0 is defined as the number of relaxations on the coarsest level 1. The following recursive description defines the coarse grid correction cycle for a given level k - taken from [12].

Multi-level cycle (k,ν_1,ν_2,γ)

If $k > 1$:

- perform ν_1 relaxations on equation
$$L^k \underline{u}^k = \underline{f}^k \tag{5.19}$$
yielding $\widetilde{\underline{u}}^k$.
- coarsen to grid $k-1$ to define the level $k-1$ grid problem
$$L^{k-1} \underline{u}^{k-1} = \underline{f}^{k-1} \tag{5.20}$$
where
$$\underline{f}^{k-1} = L^{k-1}\left(I_k^{k-1} \widetilde{\underline{u}}^k\right) + I_k^{k-1} \underline{r}^k \tag{5.21}$$
with
$$\underline{r}^k = \underline{f}^k - L^k \widetilde{\underline{u}}^k \tag{5.22}$$
- perform γ times **Multi-level cycle** ($k-1$,ν_1,ν_2,γ) yielding an approximation $\widetilde{u}^{k-1}$ to the solution of the coarse grid problem defined by Equation (5.21)
- correct the grid k approximation $\widetilde{\underline{u}}^k$
$$\overline{\underline{u}}^k = \widetilde{\underline{u}}^k + I_{k-1}^k \left(\widetilde{\underline{u}}^{k-1} - I_k^{k-1} \widetilde{\underline{u}}^k\right) \tag{5.23}$$
- perform ν_2 relaxations on grid k

Else

- perform ν_0 relaxations on the problem
$$L^k \underline{u}^k = \underline{f}^k \tag{5.24}$$

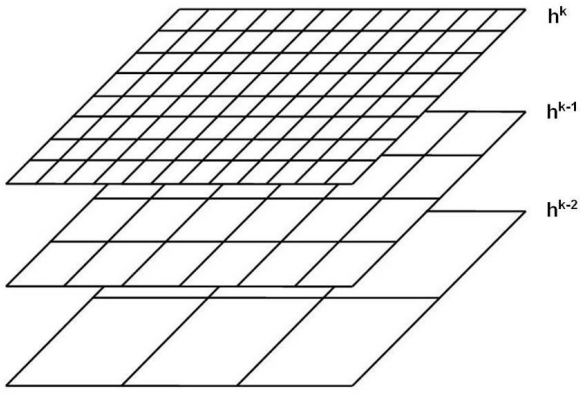

Fig. 5.2 Example of multiple grids [136].

The above described coarse grid correction cycle is known as V-cycle with $\gamma = 1$. The V-cycle usually defined as $V(\nu_1, \nu_2)$ is the simplest multigrid cycle. An alternative cycle is the $W(\nu_1, \nu_2)$-cycle, with $\gamma = 2$, where there are two coarse grid cycles on each level. Figures 5.3 and 5.4 illustrate the V- and W-cycles.

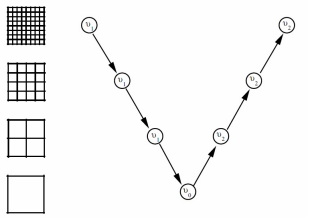

Fig. 5.3 V-cycle [139].

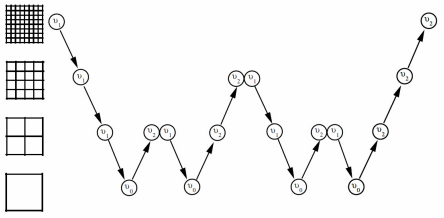

Fig. 5.4 W-cycle [139].

Computational work and cycle performance

The advantage of the multigrid cycles lies in their efficiency. Venner [9] demonstrated the power of the MG method compared to a single grid solution procedure by the following analysis. An estimation of the error reduction per cycle is given as a function of the cycle parameters which results in a parameter defined as the number of cycles required to obtain a solution up to the level of the discretization error. The local mode or smoothing rate analysis defines the asymptotic reduction factor $\overline{\mu}$ expressing how well high-frequency components, which can not be represented on a coarser grid, are reduced by a single relaxation sweep. Hence, high-frequency error components are at least reduced by a factor $\overline{\mu}^{\nu}$ where $\nu = \nu_1 + \nu_2$ is the total number of relaxations on the grid [10]. $\overline{\mu}$ is defined as the maximum amplification factor for the error components that can not be described on a coarse grid

$$\overline{\mu} = \max_{\pi/2 \leq |\theta| \leq \pi} \tag{5.25}$$

The local mode analysis is presented in [12] in detail.

Venner and Lubrecht [12] defined the amount of work of a coarse grid correction cycle in terms of a so-called 'work unit' (WU). One WU is equivalent to one relaxation on the finest grid and is defined as the following for a d-dimensional problem

$$W_{cycle} \leq \frac{\nu_1 + \nu_2}{1 - \gamma \left(h/H\right)^d} WU \qquad \text{for} \quad \gamma \left(h/H\right)^d < 1 \tag{5.26}$$

Assuming an arbitrary initial approximation the number of cycles needed to solve the problem up to the level of discretization error is defined as

$$M \geq \frac{s \ln \left(n\right)}{\ln \left(1/\overline{\mu}^{\nu_1+\nu_2}\right)} \tag{5.27}$$

where s is the order of the discretization and n the number of grid points. It follows from Equation (5.27) that to converge below the discretization error $M = \mathcal{O}(\ln n)$ cycles are needed. The total amount of work assuming that the work required for one cycle is $\mathcal{O}(n)$ will be $\mathcal{O}(n \ln n)$.

Full multigrid

The poor initial approximation dictates that $\mathcal{O}(\ln n)$ coarse grid correction cycles are required to converge below the discretization error. The number of cycles can

be reduced to $\mathcal{O}(1)$ by improving the initial approximation [10]. The process of full multigrid (FMG) is designed to eliminate the large errors which would exist on the fine grid, before it is first used [12]. A solution from a coarser grid can be used as a starting solution. Figure 5.5 illustrates the FMG scheme starting on level 1.

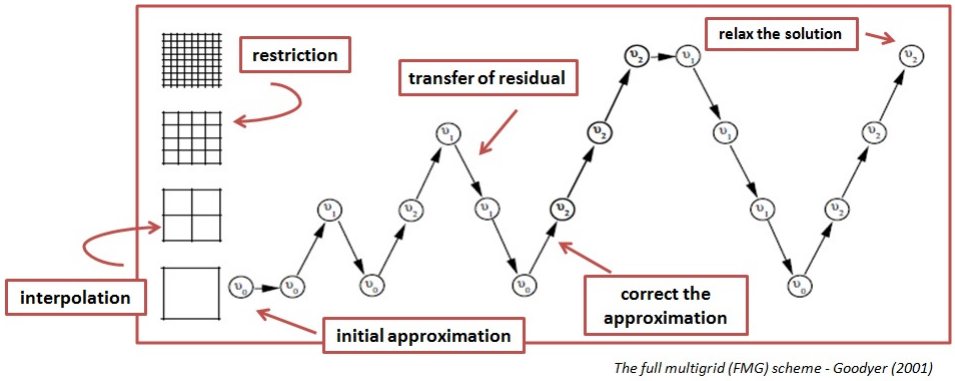

Fig. 5.5 Full multigrid (FMG) scheme [139].

In case of an FMG cycle the number of cycles needed to solve the problem up to the level of discretization error will be

$$M \geq \frac{s \ln(2)}{\ln\left(1/\overline{\mu}^{\nu_1+\nu_2}\right)} \tag{5.28}$$

and the total amount of work

$$W_{FMG} \leq M \frac{\nu_1+\nu_2}{\left(1-2^{-d}\right)^2} WU \qquad \text{for} \quad \gamma\left(h/H\right)^d < 1 \tag{5.29}$$

With an FMG cycle the total amount of work will be $\mathcal{O}(n)$.

Convergence

For an FMG procedure yielding solutions on different grids, it is easy to check the order of the discretization error. A difference norm $ERR(k, k-1)$ for a converged solution $\widetilde{\underline{u}}^k$ on grid k (in order to verify the order of convergence) is defined in [9]

$$ERR(k, k-1) = H^d \sum \left| \widetilde{\underline{u}}^{k-1} - I_h^H \widetilde{\underline{u}}^k \right| \tag{5.30}$$

The difference norm is made up of several parts: the discretization errors on grids k and $k-1$

$$h^d \sum \left| \underline{u} - \underline{u}^k \right| \qquad \text{and} \qquad H^d \sum \left| \underline{u} - \underline{u}^{k-1} \right| \tag{5.31}$$

and the algebraic errors on grids k and $k-1$

$$h^d \sum \left| \widetilde{\underline{u}}^k - \underline{u}^k \right| \qquad \text{and} \qquad H^d \sum \left| \widetilde{\underline{u}}^{k-1} - \underline{u}^{k-1} \right| \tag{5.32}$$

Transient problems - F cycle

An alternative cycle called the F-cycle is applied to solve time-dependent problems. Venner and Lubrecht [12] give a short description of it as: "*an F-cycle is a kind of FMG cycle, preceded by a series of restrictions to the coarsest grid, after doing the time increment. The solution process starts at the coarsest grid to allow the low frequency errors induced by the time increment to converge before going to a finer grid*". Figure 5.6 shows an F-cycle for a given time step.

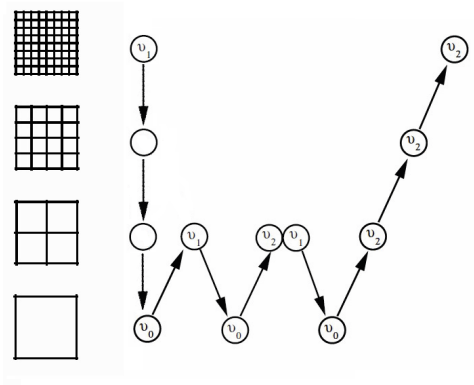

Fig. 5.6 Multigrid F-cycle.

5.2 Multilevel multi-integration

The multilevel multi-integration (MLMI) was introduced by Brandt [108] and applied to the EHL model by Brandt and Lubrecht [109] and Venner [9]. The description of the MLMI given here is based on [12]. It was shown that the complexity of the FMG algorithm is $\mathcal{O}(n)$. However, assuming the EHL problem, only the elastic deformation integrals require $\mathcal{O}(n^2)$ operations. A reduction in the complexity of the film thickness equation can be achieved by the application of MLMI.

A general notation of an integral problem $w(x)$ to be solved by MLMI is

$$w(x) = \int_{\Omega} K(x,y)\, u(y)\, dy, \qquad x \in \Omega \subseteq \mathbb{R}^d \tag{5.33}$$

where function $u(y)$ and kernel $K(x,y)$ are known, $x = (x_1, \ldots, x_d)$ and $y = (y_1, \ldots, y_d)$, and d denotes the dimension of the problem. Equation (5.33) can be rewritten in terms for the integral of elastic deformations introduced in Equation (2.17) as

$$w(x) = \frac{2}{\pi E_r} \int_{-\infty}^{\infty} \int_{-\infty}^{\infty} \frac{p(x',y')\, dx'dy'}{\sqrt{(x-x')^2 + (y-y')^2}} \tag{5.34}$$

or in its dimensionless form as

$$w(x) = \frac{2}{\pi^2} \int_{-\infty}^{\infty} \int_{-\infty}^{\infty} \frac{P(X',Y')\, dX'dY'}{\sqrt{(X-X')^2 + (Y-Y')^2}} \tag{5.35}$$

with $x = (x_1, x_2) = (X, Y)$ and $y = (y_1, y_2) = (X', Y')$.

The problem (5.33) states that an integral over all points of the integration domain Ω is to be calculated in all points of the domain Ω [12]. We refer to this problem as multi-integral or integral transfer. The discrete form of Equation (5.33) considering a grid h is

$$\underline{w}^h = K^{hh}\underline{u}^h \tag{5.36}$$

where K^{hh} is a dense matrix and $\underline{u}^h$ and $\underline{w}^h$ are vectors. This type of equation appears in many physical problems in which the kernel K^{hh} has some special properties. These properties enable to reduce the cost of the multi-summation $K^{hh}\underline{u}^h$ [12]. The advantage of the approach lies in the use of the smoothness properties of the discrete kernel. As already mentioned, the work count required for a problem such as (5.36) with N grid points is $\mathcal{O}(N^2)$. However, the number of computational operations can be reduced assuming an accuracy ϵ and with a smooth kernel to $\mathcal{O}(N\ln(1/\epsilon)/\ln\ln(1/\epsilon))$, or with an asymptotically smooth kernel to $\mathcal{O}(N\ln(1/\epsilon))$.

In [109] the author's aim was to apply coarser grids to reduce the computational time and at the same time not to lose significantly on the accuracy of the integral problem. As explained in Section 5.1 the smooth error components can be solved on coarser grids. A function which can be represented approximately on a coarser grid has to be found. Since u^h may be very non-smooth, the kernel K has to be investigated. In [12] by *smooth* it is meant that "*at a given point the value of* K^{hh} *can be obtained accurately from the value of* K^{hh} *in a number of points in its vicinity by means of a sufficiently high order interpolation.*" A smooth kernel satisfies this statement over the entire domain, while a singular smooth kernel is smooth except for a small region around a singularity [12]. For the EHL problem a potential-type kernel will be used which belongs to the latter group.

5.2.1 Discrete multi-integral

The problem (5.33) will be discretized on domain Ω assuming a uniform grid h in each dimension. The grid x is referred to as the evaluation grid and grid y as the integration grid, these two grids coincide [12]

$$w^h\left(w_i^h\right) = w_i^h \equiv \int_\Omega K\left(x_i^h, y\right)\widehat{u}^h\left(y\right)dy = h^d\sum_j K_{i,j}^{hh}u_j^h \tag{5.37}$$

where $\widehat{u}^h$ is a piecewise polynomial function of degree $2s-1$ and $\widehat{u}^h\left(y_j^h\right) = u_j^h$ [12]. The factor h^d of a d-dimensional problem has to ensure that the kernel K^{hh} and vector $\widehat{u}^h$ are of comparable magnitude on grids with different mesh sizes [12]. The discretization error (the truncation error of the discrete integral) introduced by each x in w^h will be $\left|\tau^h\right| < h^{2s}\left|K\right|\left\|u^{(2s)}\right\|$ with the $2s^{th}$ derivative of u, $\left\|u^{(2s)}\right\|$, and the average $|K|$ of the absolute values of K^{hh} over the domain.

The mesh size of the coarse grid will be $H = 2h$ and the evaluation and integration grids' points will be $x_{2I}^h = x_I^H$ and $y_{2J}^h = y_J^H$ respectively. As in the case of the multigrid method, the grids will be referred to as levels, with level 1 being the coarsest grid. Furthermore, similar transfer operators will be defined. Interpolation yielding the fine grid values of w_i^h from a number of values of the coarse grid variable

w^H is [12]

$$w_i^h = \left[\mathbb{I}_H^h w_\cdot^H\right]_i \tag{5.38}$$

where $\mathbb{I}_H^h$ is the interpolation operator of higher order which is $2p$ and the dot indicates that the interpolation is done with respect to index I [12]. The other operator (the anterpolation operator) ensuring the transfer from fine to coarse grid will be the transpose of the interpolation operator denoted as $\left(\mathbb{I}_H^h\right)^T$.

5.2.2 Smooth kernel

If the kernel is smooth as a function of both x and y, than the task of calculating Equation (5.37) for all points i, summing over all points j can be replaced by [12]:

- the transfer of u^h to the coarse grid

$$u_J^H \equiv 2^{-d}\left[\left(\mathbb{I}_H^h\right)^T u_\cdot^h\right]_J \tag{5.39}$$

- the calculation of a coarse grid multi-summation

$$w_I^H \equiv \widetilde{w}_{2I}^h = H^d \sum_H K_{I,J}^{HH} u_J^H \tag{5.40}$$

  where $K_{I,J}^{HH} = K_{2I,2J}^{hh}$
- the interpolation of the result from the coarse grid to the fine grid

$$\begin{aligned} w_i^h \cong \widetilde{w}_i^h \equiv h^d \sum_j \widetilde{K}_{i,j}^{hh} u_j^h = h^d \sum_d \left[\mathbb{I}_H^h K_{i,\cdot}^{hH}\right]_j u_j^h \\ = h^d \sum_J K_{i,J}^{hH}\left[\left(\mathbb{I}_H^h\right)^T u_\cdot^h\right]_J = H^d \sum_J K_{i,J}^{hH} u_J^H \end{aligned} \tag{5.41}$$

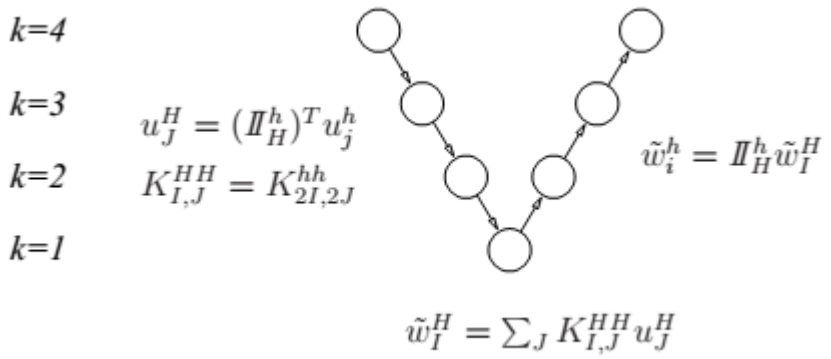

Fig. 5.7 The scheme of multilevel multi-integration cycle [10].

The kernel $\widetilde{K}_{i,j}^{hh}$ is an approximation of the discrete kernel itself, using only coarse grid points. The anterpolation and interpolation both require $\mathcal{O}(2pN)$ operations if N is the number of total grid points and $2p$ the order of interpolation. It is valid also for a d-dimensional problem provided that the transfers are carried out for one dimension at the time. The summation on the coarse grid requires $\mathcal{O}(2^{-2d}N^2)$ operations. This number might still be large, thus more coarser grids can be used until a grid is reached with $\mathcal{O}(\sqrt{N})$ points on which $\mathcal{O}(N)$ operations are required [12]. The order of interpolation has to be chosen carefully, with increasing mesh size

the order of interpolation should be increased as well. However, it is pointed out in [12] that the use of the same high order operator on each level causes only little loss. A condition determining the transfer order is defined by the error $\left|e^H\right|$ introduced in the fast evaluation on grid H and the error $\left|\tau^h\right|$ made anyway by discretizing the equation which is the function of the fine grid h

$$\left|e^H\right| < \left|\tau^h\right| \tag{5.42}$$

Figure 5.7 illustrates a cycle of multilevel multi-integration.

5.2.3 Singular smooth kernel

The situation is more complicated for an asymptotically smooth kernel. Many physical applications (like the problem of elastic deformations) use potential-type kernels, such as $K(x,y) = \ln|x-y|$ or $K(x,y) = |x-y|^{-1}$ which are singular in the neighborhood of $x = y$ [12]. Their smoothness property increases with increasing $|x-y|$ causing that the kernel will be smooth in a large part of the domain. This enables to use the same approach as outlined in the previous section, however, completed with some additional work in the neighborhood of the singularity in order to keep the additional error below a required level [12].

For a singular kernel Equation (5.41) for all fine grid points i coinciding with the coarse grid points $i = 2I$, i.e. the even points, changes to

$$\begin{aligned} w_i^h =& h^d \sum_j K_{i,j}^{hh} u_j^h = h^d \sum_j \widetilde{K}_{i,j}^{hh} u_j^h + h^d \sum_j \left(K_{i,j}^{hh} - \widetilde{K}_{i,j}^{hh}\right) u_j^h \\ =& h^d \sum_j \left[\mathbb{I}_H^h K_{i,\cdot}^{hH}\right]_j u_j^h + h^d \sum_j \left(K_{i,j}^{hh} - \widetilde{K}_{i,j}^{hh}\right) u_j^h \\ =& w_I^H + h^d \sum_J \left(K_{i,j}^{hh} - \widetilde{K}_{i,j}^{hh}\right) u_j^h \end{aligned} \tag{5.43}$$

with an additional correction term $K_{i,j}^{hh} - \widehat{K}_{i,j}^{hh}$ where $\widehat{K}_{i,j}^{hh}$ is obtained by interpolation from K^{hh} itself and which becomes smoother with increasing $|x-y|$: as $|x-y| \to \infty$ the correction term approaches $K_{i,j}^{hh} - \widehat{K}_{i,j}^{hh} \to 0$ [12].

Assuming a coarse grid with $H = 2h$ and transfer operators of the order $2p$

$$\left(K_{i,j}^{hh} - \widetilde{K}_{i,j}^{hh}\right) = \begin{cases} 0 & \text{if} \quad j = 2J \\ O\left(h^{2p} K^{(2p)}(\psi)\right) & \text{otherwise} \end{cases} \tag{5.44}$$

with the $2p^{th}$ derivative of K, $K^{(2p)}(\psi)$ at some intermediate point [12]. When the value of the derivative $K^{(2p)}(\psi)$ is small, the correction term will be negligible except for the neighborhood of the singularity. A number of so-called correction points m can be defined in which the corrections will be carried out around the singularity $i = j$. This simplification changes Equation (5.43) to

$$w_i^h \cong w_I^H + h^d \sum_{|j-i| \le m} \left(K_{i,j}^{hh} - \widetilde{K}_{i,j}^{hh}\right) u_j^h \tag{5.45}$$

For those points i of the fine grid h which do not belong to the coarse grid H, i.e. the odd points $i = 2I + 1$, the values of w^h are obtained by interpolation from the coarse grid values using an approximate kernel $\widehat{K}^{hh}_{i,j}$

$$\begin{aligned} w^h_i = h^d \sum_j K^{hh}_{i,j} u^h_j = h^d \sum_j \widetilde{K}^{hh}_{i,j} u^h_j + h^d \sum_j \left(K^{hh}_{i,j} - \widetilde{K}^{hh}_{i,j} \right) u^h_j \\ h^d \sum_j \left[\mathbb{I}^h_H K^{Hh}_{\cdot,j} \right]_i u^h_j + h^d \sum_J \left(K^{hh}_{i,j} - \widehat{K}^{hh}_{i,j} \right) u^h_j \\ \cong \left[\mathbb{I}^h_H w^H_{\cdot} \right]_i + h^d \sum_j \left(K^{hh}_{i,j} - \widehat{K}^{hh}_{i,j} \right) u^h_j \end{aligned} \tag{5.46}$$

Again, as in the case of the even points, the correction term will be applied just for a certain number of neighboring points m

$$w^h_i \cong \left[\mathbb{I}^h_H w^H_{\cdot} \right]_i + h^d \sum_{|j-i| \le m} \left(K^{hh}_{i,j} - \widehat{K}^{hh}_{i,j} \right) u^h_j \tag{5.47}$$

The correction term in (5.47) is similar to the one in (5.44) except that in this case it will be non-zero for all values of j

$$\left(K^{hh}_{i,j} - \widehat{K}^{hh}_{i,j} \right) = O\left(h^{2p} K^{(2p)}(\psi) \right) \qquad (\forall j, i = 2I + 1) \tag{5.48}$$

The total work required for the algorithm will be $\mathcal{O}((2p + \overline{m})N)$ with $\overline{m}$ being the total number of correction points. Assuming a problem with total number of grid points N the algorithm needs a total number of $\mathcal{O}(N \ln(N))$ computational operations.

To sum up, the algorithm of the multi-integration for two grids with a singular smooth kernel is presented below. The equations are identical to those in [12].

Multi-Integration: two grids

- Anterpolation
  For each point J compute u^H_J according to

$$u^H_J \equiv 2^{-d} \left[\left(\mathbb{I}^h_H \right)^T u^h_{\cdot} \right]_J \tag{5.49}$$

- Coarse grid summation
  For each point I compute w^H_I according to

$$w^H_I = H^d \sum_J K^{HH}_{I,J} u^H_J \tag{5.50}$$

- Coarse grid correction
  For each point I add a correction

$$w^H_I \leftarrow w^H_I + h^d \sum_{|2I-j| \le m} \left(K^{hh}_{2I,j} - \widetilde{K}^{hh}_{2I,j} \right) u^h_j \tag{5.51}$$

- Interpolation
  For each point i compute u_i^h using

$$w_i^h = \left[\mathbb{I}_H^h w_\cdot^H\right]_i \tag{5.52}$$

- Fine grid correction
  For each point i add a correction

$$w_i^h \leftarrow \left[\mathbb{I}_H^h w_\cdot^H\right]_i + h^d \sum_{|i-j|\leq m} \left(K_{i,j}^{hh} - \widetilde{K}_{i,j}^{hh}\right) u_j^h \tag{5.53}$$

5.3 Mathematical model

The following form of the Reynolds equation defined on the domain $\Omega = \{(x,y) \in \mathbb{R}^2 : x_a \leq x \leq x_b \wedge y_a \leq y \leq y_b\}$ is assumed

$$\underbrace{\frac{\partial}{\partial x}\left(\frac{\rho h^3 \eta_x}{12\eta}\frac{\partial p}{\partial x}\right) + \frac{\partial}{\partial y}\left(\frac{\rho h^3 \eta_y}{12\eta}\frac{\partial p}{\partial y}\right)}_{\text{Poiseuille terms}} - \underbrace{u_m \frac{\partial(\rho h)}{\partial x}}_{\text{wedge term}} - \underbrace{\frac{\partial(\rho h)}{\partial t}}_{\text{squeeze term}} = 0, \tag{5.54}$$

it is completed with boundary conditions

$$\begin{aligned} p(x_a, y) = p(x_b, y) = 0 \\ p(x, y_a) = p(x, y_b) = 0 \end{aligned} \tag{5.55}$$

and the cavitation condition

$$p(x,y,t) \geq 0 \quad \forall (x,y,t) \in \Omega \tag{5.56}$$

For the Newtonian case the effective viscosities in Equation (5.54) are

$$\eta_x = 1 \quad \text{and} \quad \eta_y = 1 \tag{5.57}$$

In the model the Eyring sinh law [25] is applied. The derivation of the effective viscosities is based on the perturbation approach presented by Ehret [43], and adapted by e.g. Jacod [30] or Chapkov [46]. The shear stresses in both direction are given by

$$\tau_x = \tau_a + z\frac{\partial p}{\partial x} \quad \text{and} \quad \tau_y = \tau_b + z\frac{\partial p}{\partial y} \tag{5.58}$$

with the average shear stress values τ_a and τ_b along x and y directions. The equivalent shear stress is

$$\tau_e = \sqrt{\tau_x^2 + \tau_y^2} \tag{5.59}$$

Greenwood [45] described that when a linear approximation of the rheological function is used then the mean shear stress along y direction is negligible and so τ_y reduces to $\tau_y = z\partial p/\partial y$, and consequently the equivalent shear stress is $\tau_e^2 = \tau_x^2$. The mean shear stress will be denoted as $\tau_e = \tau_m$ in the further parts.
The shear stress - shear rate relations are

$$\eta\frac{\partial u}{\partial z} = \tau_x f(\tau_m/\tau_0) \quad \text{and} \quad \eta\frac{\partial v}{\partial z} = \tau_y f(\tau_m/\tau_0) \tag{5.60}$$

where the rheological function $f(\tau_m/\tau_0)$ describes the Eyring sinh law [25]

$$f(\tau_m/\tau_0) = \frac{\tau_0}{\tau_m} \sinh\left(\frac{\tau_m}{\tau_0}\right) \tag{5.61}$$

By substituting Equation (5.58) into (5.60) we obtain

$$\begin{aligned} \eta\frac{\partial u}{\partial z} &= \left(\tau_a + z\frac{\partial p}{\partial x}\right) f\left(\frac{\tau_a}{\tau_0} + \frac{z}{\tau_0}\frac{\partial p}{\partial x}\right) \\ \eta\frac{\partial v}{\partial z} &= z\frac{\partial p}{\partial y} f\left(\frac{\tau_a}{\tau_0} + \frac{z}{\tau_0}\frac{\partial p}{\partial x}\right) \end{aligned} \tag{5.62}$$

First order Taylor expansion of $f(\tau_a/\tau_0 + z/\tau_0\,(\partial p/\partial x))$ with respect to z is applied

$$f\left(\frac{\tau_a}{\tau_0} + \frac{z}{\tau_0}\frac{\partial p}{\partial x}\right) = f(\tau_a/\tau_0) + \frac{z}{\tau_0}\frac{\partial p}{\partial x} f'(\tau_a/\tau_0) \tag{5.63}$$

Integration of (5.63) with respect to z results in the velocity distributions across the film

$$\begin{aligned} \eta u(z) &= \left(\frac{z^2}{2} - \frac{h^2}{8}\right)\frac{\partial p}{\partial x}\left(\frac{\tau_a}{\tau_0} f'(\tau_a/\tau_0)\right) + f(\tau_a/\tau_0) + \eta\frac{z}{h}(u_2 - u_1) + \eta u \\ \eta v(z) &= \left(\frac{z^2}{2} - \frac{h^2}{8}\right)\frac{\partial p}{\partial y} f(\tau_a/\tau_0) \end{aligned} \tag{5.64}$$

with boundary conditions $u = u_1$, $v = 0$ at $z = -h/2$ and $u = u_2$, $v = 0$ at $z = h/2$. The mean shear stress for the Eyring model is

$$\tau_m f(\tau_m/\tau_0) = \tau_0 \sinh\left(\frac{\tau_m}{\tau_0}\right) = \frac{\eta(u_2 - u_1)}{h} \tag{5.65}$$

Equations (5.64) are integrated once more with respect to z and the flow volumes are obtained. The use of the mass conversation yields the modified Reynolds equation (5.54) with the effective viscosities

$$\eta_x = \cosh\left(\frac{\tau_m}{\tau_0}\right) \quad \text{and} \quad \eta_y = \frac{\tau_0}{\tau_m}\sinh\left(\frac{\tau_m}{\tau_0}\right) \tag{5.66}$$

The lubricant is assumed to be compressible and the Dowson-Higginson pressure-density relation is used

$$\rho(p) = \rho_0 \frac{5.9 \cdot 10^8 + 1.34p}{5.9 \cdot 10^8 + p} \tag{5.67}$$

The Roelands pressure-viscosity relation is used to model the viscosity η

$$\eta(p) = \eta_0 \exp\left((\ln(\eta_0) + 9.67)\left(-1 + \left(1 + \frac{p}{p_0}\right)^z\right)\right) \tag{5.68}$$

The film thickness equation consists of the mutual approach of the contacting surface h_0, the terms describing the geometry of the undeformed surfaces, the geometry of

the surface feature and the elastic deformation

$$h(x,y,t) = h_0(t) + \frac{x^2}{2R_x} + \frac{y^2}{2R_y} - \mathcal{R}(x,y,t)$$

$$+ \frac{2}{\pi E_r}\int_{-\infty}^{\infty}\int_{-\infty}^{\infty}\frac{p(x',y')\,dx'dy'}{\sqrt{(x-x')^2+(y-y')^2}}$$

The force balance equation is

$$w = \int_{-\infty}^{\infty}\int_{-\infty}^{\infty} p(x,y)\,dxdy \tag{5.69}$$

Roughness geometry

The geometry of the roughness is defined as the following. A single transverse flat-top ridge is assumed defined by its height H_d and base and top widths, W_1 and W_2 respectively. The feature $R(x,y,t)$ is on surface with velocity u_1. The other the surface with velocity u_2 is assumed to be smooth. Figure 5.8 shows the geometry of the ridge.

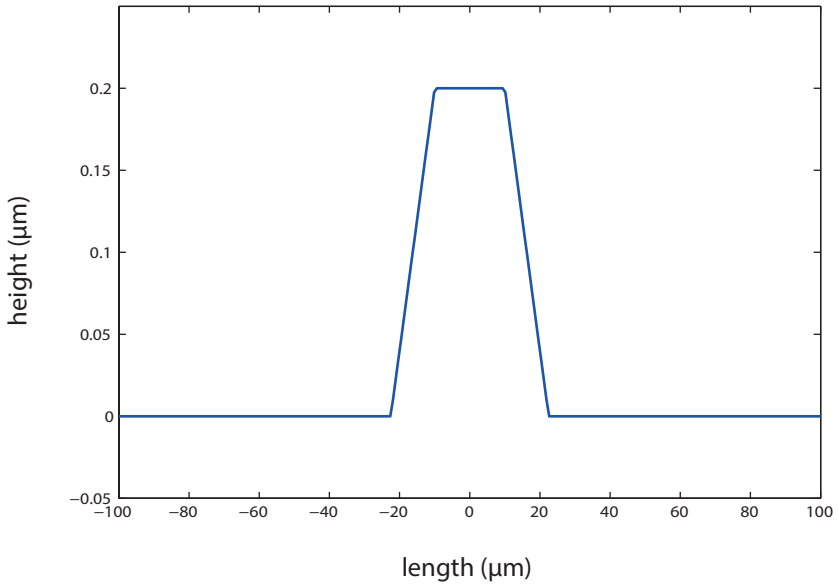

Fig. 5.8 Transverse flat-top ridge.

5.3.1 Dimensionless equations

The following dimensionless parameters are introduced and substituted into Equations (5.54)-(5.69)

$$\begin{aligned} X &= x/a & Y &= y/a \\ P &= p/p_h & H &= hR_x/a^2 \\ \bar{\eta} &= \eta/\eta_0 & \bar{\rho} &= \rho/\rho_0 \\ T &= u_m t/a & \bar{\tau_m} &= \tau_m/\tau_0 \end{aligned} \tag{5.70}$$

with the Hertzian contact radius $a = \sqrt[3]{(3wR_x)/(2E_r)}$, the Hertzian pressure $p_H = \sqrt[3]{(3wE_r^2)/(2\pi^3 R_x^2)}$ and the mean velocity of the surfaces $u_m = (u_1 + u_2)/2$.

The dimensionless Reynolds equation is

$$\frac{\partial}{\partial X}\left(\xi_X \frac{\partial P}{\partial X}\right) + \frac{\partial}{\partial Y}\left(\xi_Y \frac{\partial P}{\partial Y}\right) - \frac{\partial(\bar{\rho}H)}{\partial X} - \frac{\partial(\bar{\rho}H)}{\partial T} = 0 \tag{5.71}$$

where

$$\xi_X = \frac{\bar{\rho}H^3}{\bar{\eta}_X \bar{\lambda}} \qquad \text{and} \qquad \xi_Y = \frac{\bar{\rho}H^3}{\bar{\eta}_Y \bar{\lambda}} \tag{5.72}$$

with

$$\bar{\lambda} = \frac{12 u_m \eta_0 R_x^2}{a^3 p_h} \tag{5.73}$$

The boundary conditions are

$$P(X_a, Y) = P(X_b, Y) = P(X, Y_a) = P(X, Y_b) = 0$$

The cavitation condition is $P(X, Y, T) \geq 0$.

The film thickness equation becomes

$$\begin{aligned} H(X,Y,T) = H_0(T) + \frac{X^2}{2} + \frac{Y^2}{2} - R(X,Y,T) \\ + \frac{2}{\pi^2}\int_{-\infty}^{\infty}\int_{-\infty}^{\infty} \frac{P(X',Y',T)\,dX'dY'}{\sqrt{(X-X')^2 + (Y-Y')^2}} \end{aligned} \tag{5.74}$$

The force balance equation is

$$\int_{-\infty}^{\infty}\int_{-\infty}^{\infty} P(X,Y,T)\,dXdY = \frac{2\pi}{3} \tag{5.75}$$

5.4 Discretization

Equations (5.71)-(5.75) are discretized on a uniform grid in X and Y directions consisting of $n_x \times n_y$ grid points on a rectangular domain $X_a \leq X \leq X_b$, $Y_a \leq Y \leq Y_b$. For a grid point (i, j), where $0 \leq i \leq n_x$, $0 \leq j \leq n_y$ the coordinates are given as

$$X_i = X_a + (i-1)\,h_X \qquad \text{and} \qquad Y_j = Y_a + (j-1)\,h_Y \tag{5.76}$$

The mesh size is equal in both directions, so $h = h_X = h_Y$. Since the problem is time-dependent, the time step h_T is introduced and calculated as

$$h_T = |X_a - X_b|/(n_x - 1)$$

All terms of the Reynolds equation should be discretized by a second order manner. For the smooth EHL Reynolds equation (i.e. without the squeeze term) a second order central discretization of Poiseuille terms and a second order backward

discretization of the wedge term is applied, see e.g. [12]. The transient Reynolds equation requires a very accurate approximation. Venner and Lubrecht pointed out that the wedge and squeeze terms form together the so-called advection operator describing a propagation mechanism in the solution along the characteristic $X = T$ [12]. In case of a too large discretization error this would end in artificial amplitude decay effects. There exist two options in order to discretize the wedge and squeeze terms: the standard second order upstream discretization (SU2) requiring equal spatial and time steps, or the second order narrow upstream discretization (NU2) resulting in a combined discretization scheme of the two terms. Wijnant [10] proposed in his solution the NU2 scheme for the fully flooded conditions and the SU2 scheme for the starved lubrication problem. The current model will use the NU2 scheme.

Reynolds equation

We rewrite Equation (5.71) as

$$Q_X + Q_Y - H_X - H_T = 0 \tag{5.77}$$

The discrete Poiseuille terms in X and Y directions are

$$\begin{aligned} Q_X =& \frac{\xi_{X,i-1/2,j} P_{i-1,j} - \left(\xi_{X,i-1/2,j} + \xi_{X,i+1/2,j}\right) P_{i,j} + \xi_{X,i+1/2,j} P_{i+1,j}}{h_X^2} \\ Q_Y =& \frac{\xi_{Y,i,j-1/2} P_{i,j-1} - \left(\xi_{Y,i,j-1/2} + \xi_{Y,i,j+1/2}\right) P_{i,j} + \xi_{Y,i,j+1/2} P_{i,j+1}}{h_Y^2} \end{aligned} \tag{5.78}$$

The parameters $\xi_{X,i,j}$ and $\xi_{Y,i,j}$ were defined before in Equation (5.72). In a point (i, j) they are

$$\xi_{X,i,j} = \frac{\bar{\rho_{i,j}} H_{i,j}^3}{\eta_{\bar{X},i,j} \bar{\lambda}} \qquad \text{and} \qquad \xi_{Y,i,j} = \frac{\bar{\rho_{i,j}} H_{i,j}^3}{\eta_{\bar{Y},i,j} \bar{\lambda}} \tag{5.79}$$

In points $i \pm 1/2$ and $j \pm 1/2$ they are expressed as

$$\begin{aligned} \xi_{X,i+1/2,j} &\equiv \left(\xi_{X,i,j} + \xi_{X,i+1,j}\right)/2 \\ \xi_{X,i-1/2,j} &\equiv \left(\xi_{X,i,j} + \xi_{X,i-1,j}\right)/2 \\ \xi_{Y,i,j+1/2} &\equiv \left(\xi_{Y,i,j} + \xi_{Y,i,j+1}\right)/2 \\ \xi_{Y,i,j-1/2} &\equiv \left(\xi_{Y,i,j} + \xi_{Y,i,j-1}\right)/2 \end{aligned} \tag{5.80}$$

In case of a stationary solution the wedge term is discretized as

$$H_X = \frac{1.5\bar{\rho_{i,j}} H_{i,j} - 2.0\bar{\rho_{i-1,j}} H_{i-1,j} + 0.5\bar{\rho_{i-2,j}} H_{i-2,j}}{h_X^2} \tag{5.81}$$

Assuming a non-stationary solution the squeeze term has to be discretized too. The NU2 scheme combines the H_X and H_T terms. Depending on the ratio of h_X/h_T it has two forms. Figure 5.9 illustrates it assuming a one-dimensional problem. The two schemes are

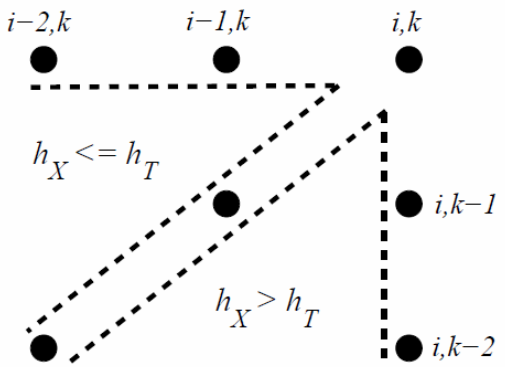

Fig. 5.9 The second order narrow upstream scheme (NU2) of a one-dimensional problem [46].

- for $h_X \leq h_T$

$$H_X + H_T = \frac{1.5\rho^{-}_{i,j}H_{i,j} - 2.0\rho^{-}_{i-1,j}H_{i-1,j} + 0.5\rho^{-}_{i-2,j}H_{i-2,j}}{h_X^{-1} - h_T^{-1}} + \frac{1.5\rho^{-}_{i,j}H_{i,j} - 2.0\rho^{k-1}_{i-1,j}H^{k-1}_{i-1,j} + 0.5\rho^{k-2}_{i-2,j}H^{k-2}_{i-2,j}}{h_T} \tag{5.82}$$

- for $h_X \geq h_T$

$$H_X + H_T = \frac{1.5\rho^{-}_{i,j}H_{i,j} - 2.0\rho^{k-1}_{i-1,j}H^{k-1}_{i-1,j} + 0.5\rho^{k-2}_{i-2,j}H^{k-2}_{i-2,j}}{h_X} + \frac{1.5\rho^{-}_{i,j}H_{i,j} - 2.0\rho^{k-1}_{i-1,j}H^{k-1}_{i-1,j} + 0.5\rho^{k-2}_{i-2,j}H^{k-2}_{i-2,j}}{h_T^{-1} - h_X^{-1}} \tag{5.83}$$

If assuming a single mesh and constant time step, the NU2 scheme would result in the use of only one of equations ((5.82) or (5.83)), however, in a multigrid algorithm both equations are used. Wijnant [10] shows the differences between the SU2 and NU2 schemes based on the values of the truncation errors. From Figure 5.10 it is apparent that the error is generally smaller for the NU2 scheme. The error vanishes at $h_T = h_X$, $h_T = 0.5h_X$ and $h_T = 2h_X$, while for the SU2 it vanishes only at $h_T = h_X$. Wijnant [10] states that the optimum choice is $h_T = 2h_X$ as "*it is the largest mesh size for which the error is dominated by higher order terms.*" An advantage of the NU2 discretization with respect to the multigrid method is the accurate representation of the characteristic components on coarser grids [10]. In the transient solver the time step will be $h_T = 0.5h_X$.

Film thickness equation

The discrete form of Equation (5.74) is

$$H_{i,j} = H_0 + \frac{X_i^2}{2} + \frac{Y_j^2}{2} - \mathcal{R}_{i,j} + \sum_{i'}\sum_{j'} K_{i,i',j,j'}P_{i',j'} \tag{5.84}$$

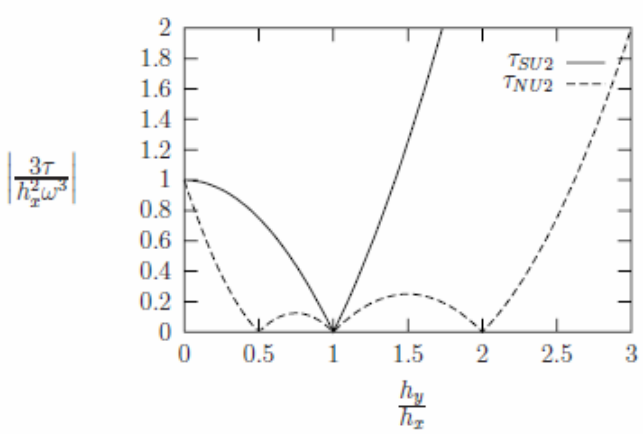

Fig. 5.10 Discretization error for SU2 and NU2 discretization [10].

where a discrete singular smooth kernel is used

$$K_{i,j} = \frac{1}{\sqrt{(X - X')^2 - (Y - Y')^2}} \tag{5.85}$$

expressed as

$$\begin{aligned} K^{hh}_{i,i',j,j'} = \frac{2}{\pi^2} \Bigg\{ & |X_p| \operatorname{arcsinh}\left(\frac{Y_p}{X_p}\right) + |Y_p| \operatorname{arcsinh}\left(\frac{X_p}{Y_p}\right) \\ & - |X_m| \operatorname{arcsinh}\left(\frac{Y_p}{X_m}\right) + |Y_p| \operatorname{arcsinh}\left(\frac{X_m}{Y_p}\right) \\ & - |X_p| \operatorname{arcsinh}\left(\frac{Y_m}{X_p}\right) + |Y_m| \operatorname{arcsinh}\left(\frac{X_p}{Y_m}\right) \\ & + |X_m| \operatorname{arcsinh}\left(\frac{Y_m}{X_m}\right) + |Y_m| \operatorname{arcsinh}\left(\frac{X_m}{Y_m}\right) \Bigg\} \end{aligned} \tag{5.86}$$

with

$$\begin{aligned} X_p &= X_i - X_{i'} + h/2 \\ X_m &= X_i - X_{i'} - h/2 \\ Y_p &= Y_j - Y_{j'} + h/2 \\ Y_m &= Y_j - Y_{j'} - h/2 \end{aligned} \tag{5.87}$$

Force balance equation

Finally, the discrete form of Equation (5.75) is

$$h^2 \sum_i \sum_j P^h_{i,j} = \frac{2\pi}{3} \tag{5.88}$$

5.5 Relaxation

The multigrid method is based on classical relaxation procedures. On each grid the same iterative relaxation process can be applied. Lubrecht [58] used the Gauss-Seidel point-wise relaxation, however, it converged only for lightly loaded cases. Venner [9] showed that in order to solve highly loaded cases the Jacobi relaxation procedure serves as a better alternative. The coefficient ξ defined in Equations (5.79) changes many orders of magnitude over the domain [12]. With varying values of ξ the nature of the problem (5.71) varies as well. In the Hertzian contact region, i.e. $X^2+Y^2 \leq 1$, the integral aspect of the problem dominates, the elastic deformations are important and the small values of ξ ($\xi << 1$) cause the Poiseuille terms to be negligible. On the other hand, outside the contact zone the values of ξ are large ($\xi >> 1$) and the flow is dominated by the Poiseuille terms. In order to design a stable solver the aspect of varying ξ has to be considered. Venner [9] defined a switch criterion based on the value of ξ. This criteria works as the following: when the value of ξ is small, the Gauss-Seidel relaxation can be applied. For large values of ξ, the Jacobi relaxation is used. The criterion is defined as:

- if $\xi > 0.3$ the Gauss-Seidel line relaxation is used,
- if $\xi \leq 0.3$ the distributive Jacobi line relaxation is used.

5.5.1 Low pressures - Gauss-Seidel line relaxation

For low values of pressure the Gauss-Seidel relaxation is a stable and efficient smoother. In the current work the point-wise relaxation of the Reynolds equation is replaced by line relaxation. At each relaxation sweep the system is scanned line by line (assuming line relaxation in X direction) and the equations of a given line j are solved simultaneously for each grid point i. After the system of equations for a given line is solved, the changes are applied simultaneously to all points of the line and a new approximation of the pressure $\bar{P}^h_{i,j}$ for each grid point i of a given line j is computed from a previous approximation $\tilde{P}^h_{i,j}$

$$\bar{P}^h_{i,j} = \tilde{P}^h_{i,j} + \omega_{gs}\delta^h_{i,j} \tag{5.89}$$

The values of the change $\delta^h_{i,j}$ are obtained as the following [12]. In the case of line relaxation a system of equations is defined for each line j for $0 < i < n_x$

$$A^j \underline{\delta}^h_j = \underline{r}^h_j \tag{5.90}$$

where A^j is a matrix of coefficients, $\underline{\delta}^h_j$ is the vector of changes and $\underline{r}^h_j$ is the vector of the current residuals. The residuals are obtained as

$$r^h_{i,j} = -\xi\frac{\bar{P}^h_{i-1,j} - 2\tilde{P}^h_{i,j} + \tilde{P}^h_{i+1,j}}{h^2} - \xi\frac{\bar{P}^h_{i,j-1} - 2\tilde{P}^h_{i,j} + \tilde{P}^h_{i,j+1}}{h^2} + \frac{1.5\tilde{H}^h_{i,j} - 2\tilde{H}^h_{i-1,j} + 0.5\tilde{H}^h_{i-2,j}}{h} \tag{5.91}$$

The coefficients $A^j_{i,k}$ of matrix A^j are defined as

$$A^j_{i,k} = \frac{\partial\left(L^h\underline{P}^h\right)_{i,j}}{\partial P_{k,j}} \tag{5.92}$$

The system of equations for the new values of the pressure should be updated together with the new values of film thickness. Since updating the values of H depends on P and involves a summation of changes the matrix A_j will be full. However, as explained in [12] it is sufficient to take into account only the terms in the summations related to the direct neighbors of a point i [12]. This results in a banded matrix, more precisely, it is sufficient to solve a hexadiagonal system with $A^j_{i,k} = 0$ for $k < i - 3$ and $k > i + 2$ [12]. The non-zero coefficients of $A^h_{i,k}$ are defined in Appendix C of [12].

5.5.2 High pressures - Jacobi distributive line relaxation

Inside the Hertzian contact zone the values of ξ are small and this reduces the Reynolds equation to the transport equation. The Gauss-Seidel line relaxation is unstable for such values of ξ. Venner and Lubrecht [12] account this instability to the accumulation of the changes in the summation in the definition of film thickness H. To avoid this issue distributive relaxation can be applied. It means that instead of updating only one unknown several of them can be updated simultaneously. Again, as for low pressure, by line relaxation good smoothing can be achieved. By the distributive Jacobi line relaxation the new values of the pressures $\bar{P}^h_{i,j}$ for each grid point i in X direction and for a given line j are obtained as

$$\bar{P}^h_{i,j} = \tilde{P}^h_{i,j} + \omega_{ja} \left(\delta^h_{i,j} - \left(\delta^h_{i-1,j} + \delta^h_{i+1,j} + \delta^h_{i,j-1} + \delta^h_{i,j+1} \right) /4 \right) \tag{5.93}$$

Similarly as in the case of the Gauss-Seidel line relaxation a system of equations for a given line j can be defined with the vector $\underline{\delta}^h_j$ of changes $\delta^h_{i,j}$ and the vector $\underline{r}^h_j$ of residuals $r^h_{i,j}$

$$A^j \underline{\delta}^h_j = \underline{r}^h_j \tag{5.94}$$

The matrix coefficients $A^j_{i,k}$ will be

$$A^j_{i,k} = \frac{\partial \left(L^h \underline{P}^h \right)_{i,j}}{\partial P_{k,j}} - \frac{1}{4} \left(\frac{\partial \left(L^h \underline{P}^h \right)_{i,j}}{\partial P_{k+1,j}} + \frac{\partial \left(L^h \underline{P}^h \right)_{i,j}}{\partial P_{k-1,j}} + \frac{\partial \left(L^h \underline{P}^h \right)_{i,j}}{\partial P_{k,j+1}} + \frac{\partial \left(L^h \underline{P}^h \right)_{i,j}}{\partial P_{k,j-1}} \right) \tag{5.95}$$

Again a banded matrix is sufficient as in the case of large values of ξ. The non-zero coefficients of $A^j_{i,k}$ are defined in Appendix C in [12].

Both relaxation schemes assume underrelaxation. The underrelaxation factor of the Gauss-Seidel scheme ω_{gs} is between the values of 0.8 and 0.2 while the Jacobi scheme ω_{ja} ranges from 0.6 to 0.1. The cavitation condition has to be considered too. After a change $\delta^h_{i,j}$ is applied the new value of pressure is checked and set to zero in case it has a negative value.

5.5.3 Relaxation of the force balance equation

The force balance equation (5.69) is relaxed by updating the value of H_0. This is done only on the coarsest grid

$$\bar{H}_0 = \tilde{H}_0 + \omega_{H_0} \left({}_w f^h - h^2 \sum_{i,j} \tilde{P}^h_{i,j} \right) \tag{5.96}$$

with the underrelaxation factor ω_{H_0} and the force balance right hand side ${}_w f^h$ which is $2\pi/3$ for a single grid. The value of the underrelaxation factor greatly determines the nature of the convergence of the force balance equation [12]. If its value is too large the residual of the force balance equation will oscillate, on the contrary, if its value is too small the convergence will be very slow. Here, the value of ω_{H_0} ranges from 0.1 to 0.001 for the non-smooth problems.

5.6 Implementation details

The following section presents some additional insights concerning the numerical model. The solution process is explained on the smooth contact stationary solver. The non-stationary solver is basically the extension of the stationary solver. At each time step the same process is repeated and the converged solution of the pressure and film thickness in time step t is used as the initial approximation in the next time step $t+1$. Tables 5.1 and 5.2 contain summaries of the input parameters (operating conditions and numerical parameters) necessary to be defined.

Tab. 5.1 Input parameters - operating conditions.

Operating conditions	
load	w [N]
reduced radius of curvature	R_x [m]
reduced Young's modulus	E_r [GPa]
pressure-viscosity coefficient	α [GPa^{-1}]
viscosity at ambient pressure	η_0 [Pas]
mean speed	u_m [m/s]
slide to roll ratio	SRR [-]
Eyring shear stress	τ_0 [MPa]
surface feature parameters	
height (amplitude)	H_d [nm]
base width (wavelength)	w_1 [µm]
top width (wavelength)	w_2 [µm]

Tab. 5.2 Numerical parameters.

Numerical parameters.	
maximum level	
starting level	
type of cycle	V-, W- or F-cycle
number of cycles	
Gauss-Seidel relaxation factor	ω_{gs}
Jacobi relaxation factor	ω_{ja}
force balance relaxation factor	ω_{H_0}
computational domain	$[x_a, x_b] \times [y_a, y_b]$
timestep	h_t

The stationary numerical model assumes the following steps:

- definition of the input parameters - see Tables 5.1 and 5.2
- initial approximation of the pressure distribution P and mutual approach H_0
  - Hertzian pressure distribution $P = \sqrt{1 - X^2 - Y^2}$
  - mutual approach $H_0 = 1.67M^{-\frac{1}{9}} - 1.897 + 0.2L/50$
- repeat for all levels k while $k > 2$
  - calculate the film thickness H
  - relax ν_1-times the pressure P
  - transfer the pressure P and residuals r
  - calculate the right hand side values f
- for level $k = 1$
  - calculate the film thickness H
  - relax ν_0-times the pressure P
  - calculate and update the mutual approach H_0
- repeat for all levels k from $k > 2$ to $k = level_{max}$
  - transfer the pressure P
  - correct the pressure P
  - calculate the film thickness H
  - relax ν_2-times the pressure P

5.7 Experiments

The results of the numerical simulations will be compared to experimentally measured film thickness which is obtained by colorimetric interferometry. More about the experimental apparatus and the method of obtaining the film thickness can be found in [140].

6 RESULTS AND DISCUSSION

The results are divided into two sections. The aim of the first part is to verify the performance of the smooth contact solver which forms the basis for the more complicated time-dependent solver. Smooth contact results are presented for both Newtonian and non-Newtonian rheology models. The values of central and minimum film thicknesses are compared with experimentally measured values for a range of operating conditions. The accuracy of the numerical solver is tested by means of comparison with published work of other authors. The second part of the chapter presents non-stationary simulations with a specific surface feature passing through the contact zone. The effect of different operating conditions and oil parameters on the roughness deformation, film thickness and pressure distribution is studied.

6.1 Smooth EHL

The current section presents film thickness and pressure profiles of a smooth EHL point contact. This smooth contact model is described by Equations (5.71)-(5.75), although in the current case the Reynolds equation is stationary, i.e. the squeeze term in (5.71) is omitted. The effect of the fluid rheology model is investigated as well, results both with a Newtonian and a non-Newtonian model are presented and compared. The multigrid method described in detail in Section 5.1 is used to solve the Reynolds equation. In the case of the stationary point contact model a FMG cycle is used. The multilevel multi-integration described in Section 5.2 is applied to obtain the elastic deformations in the film thickness equation.

6.1.1 Operating conditions

The operating conditions used in the simulations are summarized in the following tables. Table 6.2 contains the geometry and material properties of the contacting bodies (a steel ball and a glass disc), and the oil characteristics, the pressure-viscosity coefficient α and the viscosity at ambient pressure η_0.

During the stationary simulations three different loads and a range of mean velocities were assumed under pure rolling conditions. The loads and the corresponding values of the Hertzian pressure p_H and the Hertzian radius a are summarized in Table **??**. The following mean velocities u_m were assumed: 0.01, 0.02, 0.04, 0.08, 0.125, 0.2, 0.3 and 0.4 m/s. Finally, Table 6.3 contains the values of the dimensionless parameters of Hamrock and Dowson (load W (2.33), speed U (2.34) and material G (2.35)) and the Moes parameters (load M (2.39) and material L (2.40)), respectively for each load case and entrainment velocity.

Tab. 6.1 Load cases and the corresponding Hertzian pressures and Hertzian radii.

Material properties		
	steel	glass
Young's modulus E [GPa]	210	81
Poisson's ratio μ	0.3	0.208
Reduced Young's modulus E_r [GPa]		123.8
Contact geometry		
Reduced radius of curvature R_x [m]		0.0127
Oil characteristics - SR 600		
Pressure-viscosity coefficient α [GPa^{-1}]		24
Viscosity at ambient pressure η_0 [Pas]		0.3

Tab. 6.2 Material properties, geometry of the contacting bodies and oil parameters.

	case 1	case 2	case 3
load w [N]	9	27	73
Hertzian pressure p_H [GPa]	0.35	0.5	0.7
Hertzian radius a [µm]	111	161	224

Tab. 6.3 The values of the Hamrock-Dowson dimensionless parameters of load W, speed U and material G, and the Moes dimensionless parameters of load M and material L for each mean velocity u_m of the three load cases.

Load w [N]	Mean velocity u_m [m/s]	W [-]	U [-]	G [-]	M [-]	L [-]
	0.01		$3.816 \cdot 10^{-12}$		165.08	4.15
	0.02		$7.632 \cdot 10^{-12}$		98.16	4.94
case 1	0.04		$1.526 \cdot 10^{-11}$		58.37	5.87
	0.08	$4.507 \cdot 10^{-7}$	$3.053 \cdot 10^{-11}$	2971	34.70	6.98
	0.125		$4.770 \cdot 10^{-11}$		24.83	7.81
9 N	0.2		$7.632 \cdot 10^{-11}$		17.46	8.78
	0.3		$1.145 \cdot 10^{-10}$		12.88	9.72
	0.4		$1.526 \cdot 10^{-10}$		10.38	10.44
	0.01		$3.816 \cdot 10^{-12}$		495.24	4.15
	0.02		$7.632 \cdot 10^{-12}$		294.47	4.94
case 2	0.04		$1.526 \cdot 10^{-11}$		175.09	5.87
	0.08	$1.352 \cdot 10^{-6}$	$3.053 \cdot 10^{-11}$	2971	104.11	6.98
	0.125		$4.770 \cdot 10^{-11}$		74.50	7.81
27 N	0.2		$7.632 \cdot 10^{-11}$		52.37	8.78
	0.3		$1.145 \cdot 10^{-10}$		38.63	9.72
	0.4		$1.526 \cdot 10^{-10}$		31.14	10.44
	0.01		$3.816 \cdot 10^{-12}$		1338.98	4.15
	0.02		$7.632 \cdot 10^{-12}$		796.16	4.94
case 3	0.04		$1.526 \cdot 10^{-11}$		473.40	5.87
	0.08	$3.656 \cdot 10^{-6}$	$3.053 \cdot 10^{-11}$	2971	281.49	6.98
	0.125		$4.770 \cdot 10^{-11}$		201.42	7.81
73 N	0.2		$7.632 \cdot 10^{-11}$		141.58	8.78
	0.3		$1.145 \cdot 10^{-10}$		104.46	9.72
	0.4		$1.526 \cdot 10^{-10}$		84.19	10.44

6.1.2 Results - smooth point contact

Pressure and film thickness distribution

The first Figures 6.1 and 6.2 illustrate the 3-D profiles of the pressure and film thickness distributions in a moderately loaded EHL point contact assuming a load of 73 N and a mean velocity 0.4 m/s. The figures demonstrate the main characteristics of an EHL contact with the pressure spike or the side lobes of the film thickness distributions. In this case the Newtonian model was assumed with a compressible fluid (2.21) and the Roelands viscosity relation (2.20). The solution was obtained on the domain $[-4.5, 1.5] \times [-3, 3]$ with 513×513 grid points. Figure 6.3 shows the so-called pseudo-interferometry plot of the dimensionless film thickness profile obtained by the function $I(X, Y) = I_0 + I_0 \cos(2\pi H(X, Y)/\Delta H)$ with $I_0 = 0.5$ and $\Delta H = 0.06$. See [12] for more details.

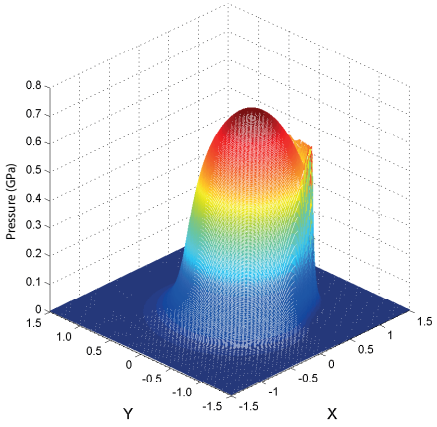

Fig. 6.1 3-D pressure profile: case 3, mean velocity 0.4 m/s.

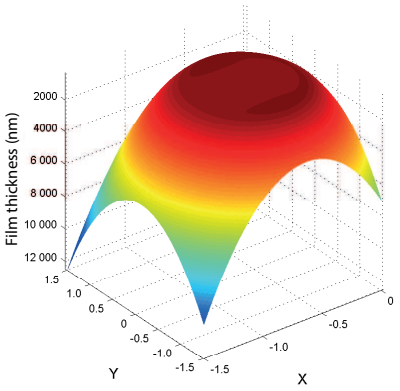

Fig. 6.2 3-D film thickness profile: case 3, mean velocity 0.4 m/s.

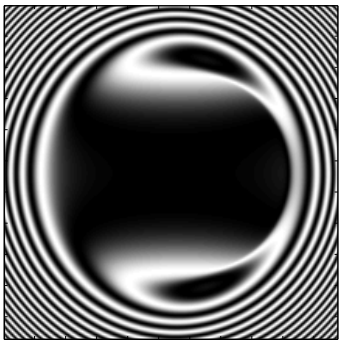

Fig. 6.3 Pseudointerferometry plot of the film thickness: case 3, mean velocity 0.4 m/s.

Figures 6.4a and 6.4b show the film thickness and pressure distributions along the center lines x=0 and y=0. These profiles demonstrate the symmetry along the y profile of the contact (Figure 6.4b) and the pressure spike and the film thickness constriction along x direction (Figure 6.4a).

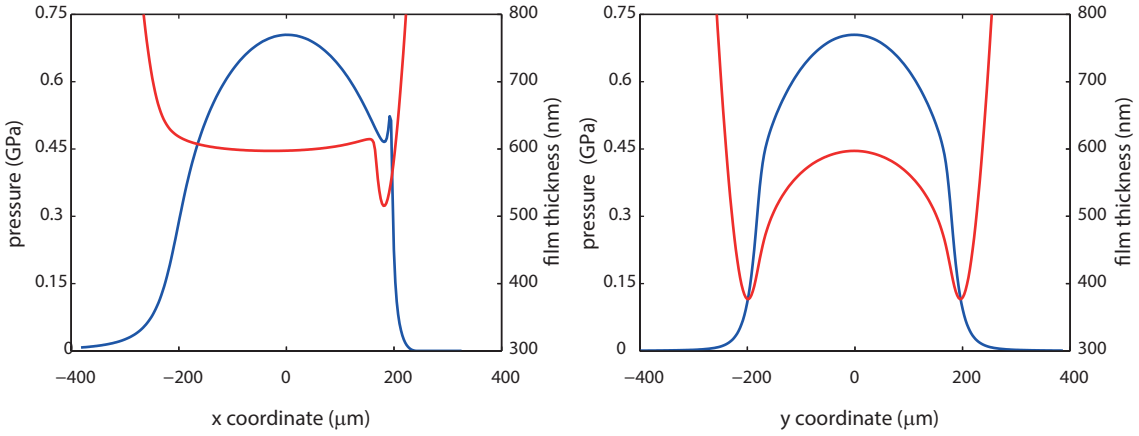

Fig. 6.4 Pressure and film thickness as a function of x at y=0: case 3, mean velocity 0.4 m/s.

The effect of the viscosity-pressure relations and the fluid compressibility is demonstrated in Figures 6.5 and 6.6. For load case 1 and mean velocity $u_m = 0.125$ m/s four different combinations of the viscosity and density relations are given. The effect of the Barus (2.19) and Roelands (2.20) viscosity relations and the lubricant compressibility (2.21) on the film thickness and pressure are studied. Both fluid properties have effect on the height of the pressure spike as well as on the variation in the film thickness.

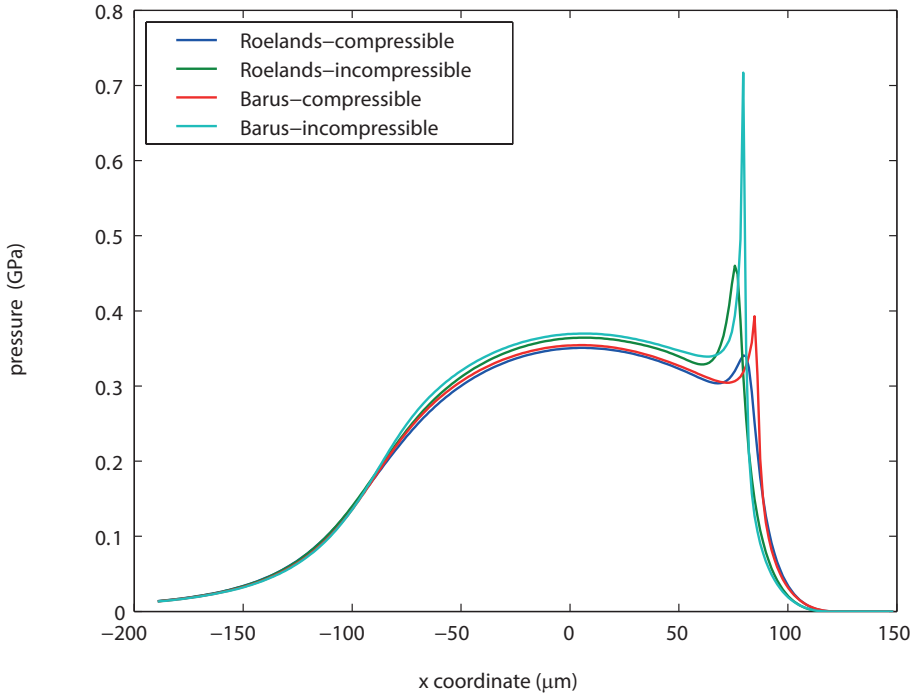

Fig. 6.5 Pressure at y=0: case 1, mean velocity 0.125 m/s.

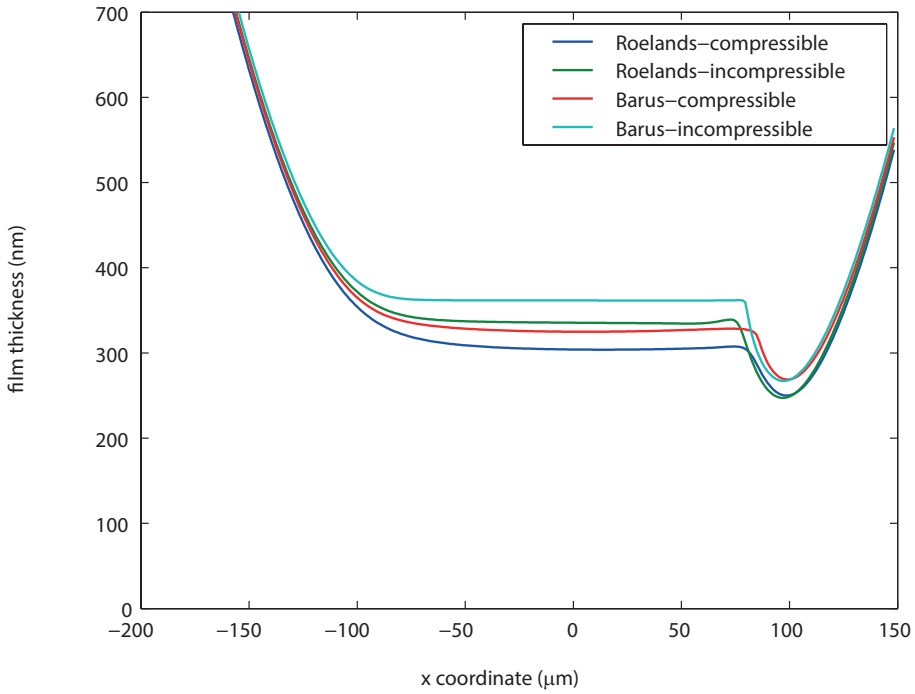

Fig. 6.6 Film thickness at y=0: case 1, mean velocity 0.125 m/s.

Rheology models

The differences between the Newtonian and non-Newtonian models are demonstrated next.

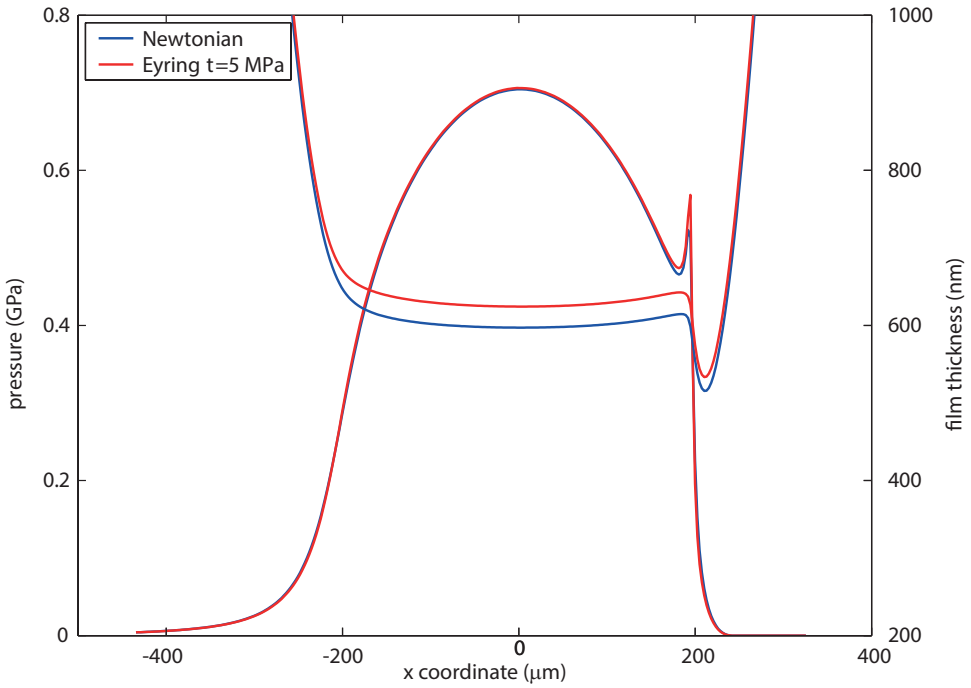

Fig. 6.7 Comparison of pressure and film thickness distributions as a function of y at x=0, case 3 with mean velocity 0.4 m/s.

Figure 6.7 shows the pressures and film thicknesses for the Newtonian (5.57)

and the Eyring model (5.66). For the Eyring model a limiting shear stress value of $\tau_0 = 5$ MPa and a slide to roll ratio (SRR) of 1 % was assumed. This slide to roll ratio is defined as

$$SRR = \frac{2\,(u_1 - u_2)}{u_1 + u_2} = \frac{u_1 - u_2}{u_m} \tag{6.1}$$

with u_1 the velocity of the ball and u_2 the velocity of the disc, i.e. for a positive SRR the disc is faster, for a negative SRR the ball is faster. The operating conditions in the simulations are the same as in Figures 6.1 - 6.3 - load case 3, mean velocity 0.4 m/s.

Comparison with experiments

Comparison between the numerically calculated central and minimum film thickness values h_c and h_{min} and the experimentally measured values are given in the current section. The values of h_c and h_{min} for the three load cases from Table **??** were numerically evaluated for each mean velocity. Moreover, approximate values of the central film thickness h_c were calculated by the Hamrock-Dowson formula (2.37). Throughout the simulations a grid with 513×513 points for load case 1, and a grid with 257×257 points for the other two load cases (2 and 3) was used. For the Eyring model the limiting shear stress $\tau_0 = 6$ MPa and the slide to roll ratio of 5% had to be defined. The Newtonian model assumed pure rolling conditions (SRR=0%). Figures 6.8-6.10 and Tables 6.4-6.6 present the results.

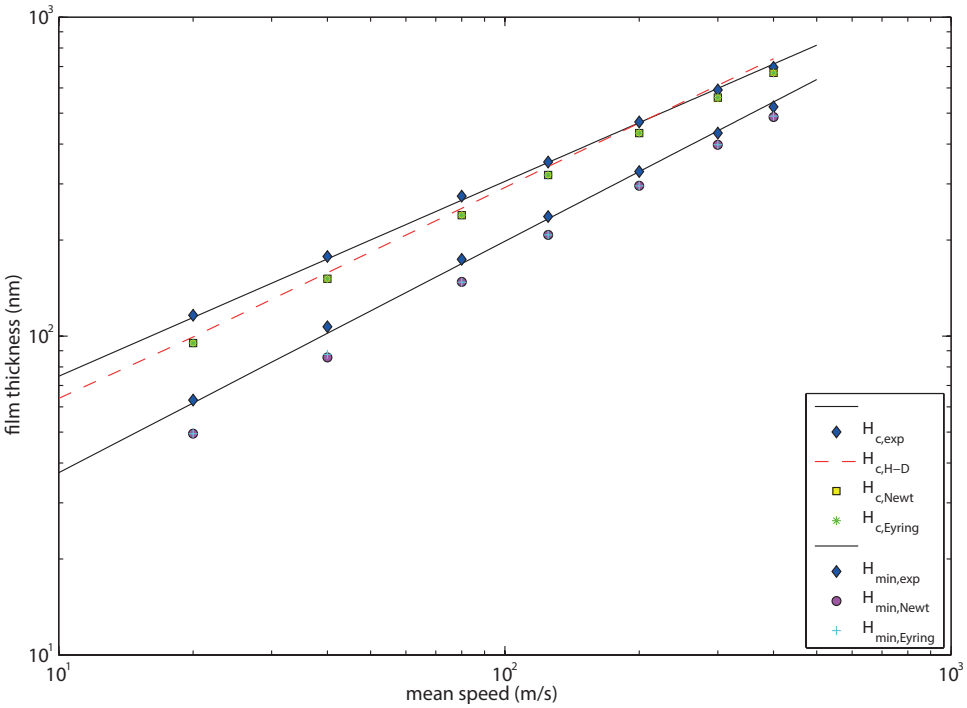

Fig. 6.8 Case 1 - load w=9 N. Comparison of the central and minimum film thickness values: experiments, Hamrock-Dowson (H-D) formula and numerical simulations with Newtonian and Eyring model. The range of mean velocities: 0.01, 0.02, 0.04, 0.08, 0.125, 0.2, 0.3 and 0.4 m/s.

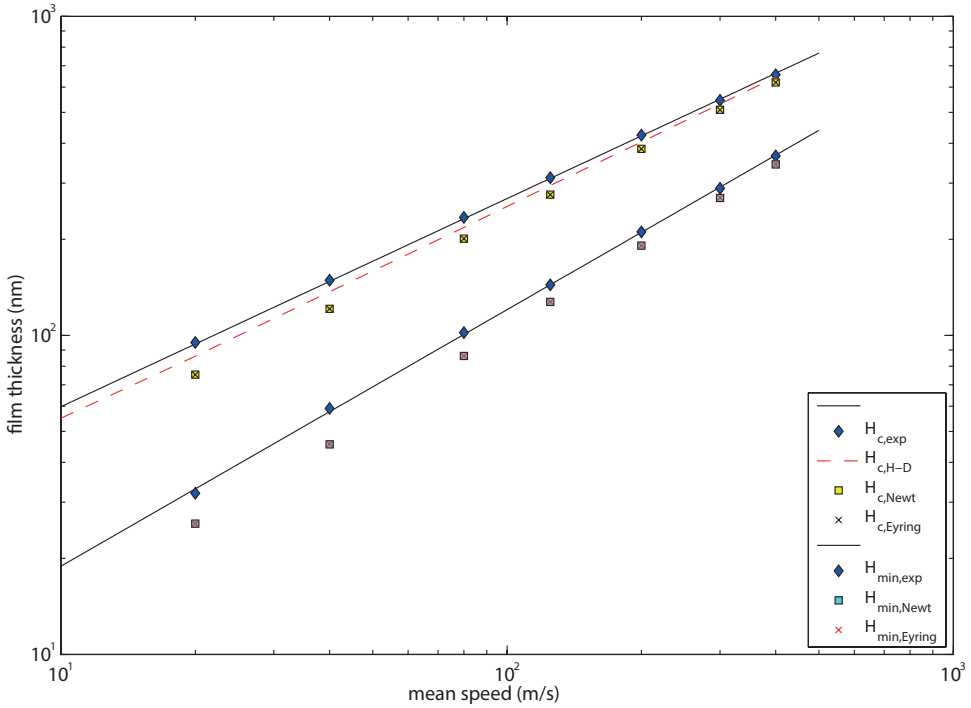

Fig. 6.9 Case 2 - load w=27 N. Comparison of the central and minimum film thickness values: experiments, Hamrock-Dowson (H-D) formula and numerical simulations with Newtonian and Eyring model. The range of mean velocities: 0.01, 0.02, 0.04, 0.08, 0.125, 0.2, 0.3 and 0.4 m/s.

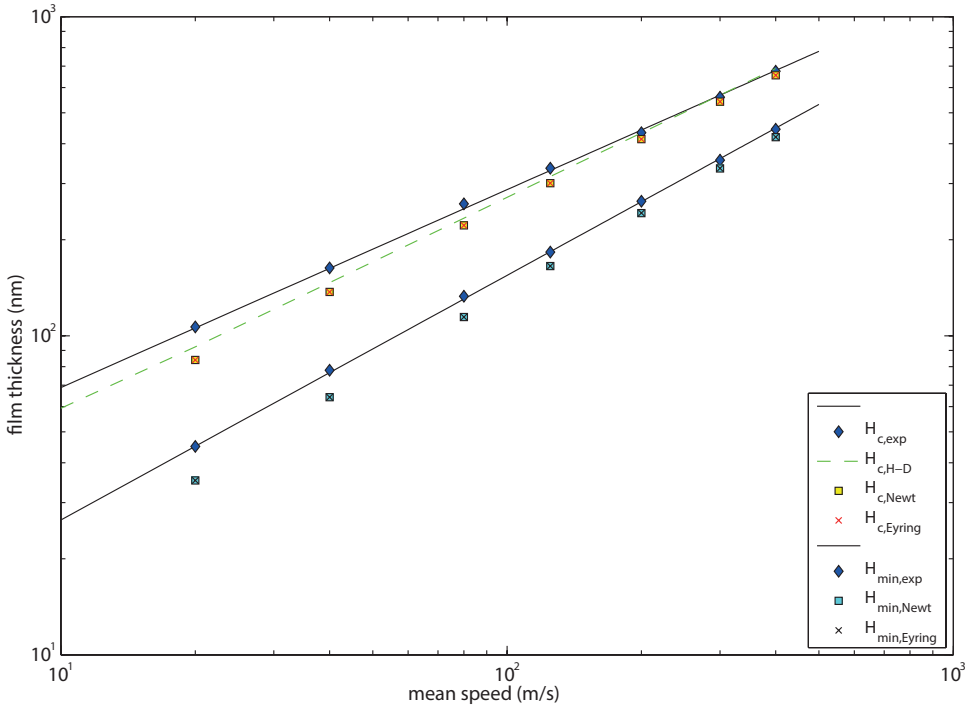

Fig. 6.10 Case 3 - load w=73 N. Comparison of the central and minimum film thickness values: experiments, Hamrock-Dowson (H-D) formula and numerical simulations with Newtonian and Eyring model. The range of mean velocities: 0.01, 0.02, 0.04, 0.08, 0.125, 0.2, 0.3 and 0.4 m/s.

Tab. 6.4 Central h_c and minimum h_{min} film thickness values for load case 1 - experiments, prediction by the Hamrock-Dowson (H-D) formula and numerical simulations with the Newtonian and Eyring fluid models.

mean velocity	Experiments		H-D prediction	Numerical simulations			
				Newtonian model		Eyring model	
(m/s)	h_c (nm)	h_{min} (nm)	h_c (nm)	h_c (nm)	h_{min} (nm)	h_c (nm)	h_{min} (nm)
0.01	72	35	63.8	59.5	28.3	59.5	28.2
0.02	116.2	63	99.3	95.1	49.4	95.1	49.4
0.04	177.6	107	158	151.3	85.8	151.3	87.7
0.08	274.6	174	251.4	239.3	147.6	239.3	147.5
0.125	351.4	237	339.8	320.0	207.8	320	207.7
0.2	469.4	328	465.3	432.9	295.8	432.9	295.8
0.3	591.4	433	611.1	559.3	398.2	559.4	398.2
0.4	696	523	740.5	668.9	486.7	669	489.3

Tab. 6.5 Central h_c and minimum h_{min} film thickness values for load case 2 - experiments, prediction by the Hamrock-Dowson (H-D) formula and numerical simulations with the Newtonian and Eyring fluid models.

mean velocity	Experiments		H-D prediction	Numerical simulations			
				Newtonian model		Eyring model	
(m/s)	h_c (nm)	h_{min} (nm)	h_c (nm)	h_c (nm)	h_{min} (nm)	h_c (nm)	h_{min} (nm)
0.01	67.2	26	59.3	50.7	19.0	50.7	19.0
0.02	106.6	45	92.3	84.0	35.2	84.0	35.2
0.04	163.2	78	146.8	137.2	64.2	137.1	64.2
0.08	259.2	133	233.6	221.8	114.5	221.8	114.5
0.125	335	183	315.7	300.9	165.4	300.9	165.4
0.2	433	264	432.3	413.4	242.4	413.3	242.5
0.3	559.7	355	567.8	541.8	334.6	541.7	334.8
0.4	674.9	444	688	655.3	419.4	655.1	419.5

Tab. 6.6 Central h_c and minimum h_{min} film thickness values for load case 3 - experiments, prediction by the Hamrock-Dowson (H-D) formula and numerical simulations with the Newtonian and Eyring fluid models.

mean velocity	Experiments		H-D prediction	Numerical simulations			
				Newtonian model		Eyring model	
(m/s)	h_c (nm)	h_{min} (nm)	h_c (nm)	h_c (nm)	h_{min} (nm)	h_c (nm)	h_{min} (nm)
0.01	58.6	19	55	44.8	12.9	44.8	12.8
0.02	95	32	86	75.3	25.7	75.3	25.7
0.04	148.8	59	137	121.1	45.5	121.1	45.6
0.08	234.2	102	218	200.9	86.2	200.9	86.2
0.125	312	144	295	276.2	127.3	276.2	127.4
0.2	424.3	211	404	384.3	191.1	384.2	191.2
0.3	545.3	289	531	509.2	269.5	509.1	269.9
0.4	655.7	365	644	620.5	343.2	620.3	343.6

6.1.3 Discussion

An accurate, stable and fast stationary contact solver of the smooth EHL problem forms the basis for the time-dependent model of rough contact problems. In order to check the performance of the current solver the convergence rate and the accuracy has to be tested and compared to previously published results and experiments.

Performance of the numerical model

A test case identical to the one in [12] is defined with the following operating conditions: load $w = 100$ N, mean speed $u_m = 0.8$ m/s, reduced Young's modulus $E_r = 226$ GPa, pressure-viscosity coefficient $\alpha = 22$ GPa^{-1}, viscosity at ambient pressure $\eta_0 = 0.04$ Pa s and the reduced radius of curvature $R_x = 0.016$ m. These input parameters correspond to Moes' parameters of load $M = 200$ and material $L = 10$. The aim is to check the performance of the current solver and to demonstrate the power of the multilevel techniques. The convergence rate is tested by studying the values of the residual norm of the Reynolds equation (2.10) and the residual of the force balance equation (2.18). These two parameters are defined as the following. The residual norm of the Reynolds equation is calculated as [12]

$$resn = h_x h_y \sum_{i=0}^{n_x} \sum_{j=0}^{n_y} |r_{i,j}| \tag{6.2}$$

with the spatial mesh size in both directions h_x and h_y, and the residuals $r_{i,j}$. The value of the residual of the force balance equation is [12]

$$r = h_x h_y \sum_{i=0}^{n_x} \sum_{j=0}^{n_y} P_{i,j} - \frac{2\pi}{3} \tag{6.3}$$

Simulations with different grids were carried out: from level 3 which equals to 65×65 grid points up to level 7 which consists of 1025×1025 grid points. For all cases a full multigrid cycle (FMG) was chosen, and the relaxation factors were kept the same throughout all calculations (the Gauss-Seidel relaxation factor $\omega_{gs} = 0.4$, the Jacobi relaxation factor $\omega_{ja} = 0.2$ and the relaxation factor of the force balance equation $\omega_{hfact} = 0.05$). Figures 6.11 and 6.12 show the dependence of the residual norm (6.2) and the absolute value of the force balance equation's residual (6.3) on the number of the FMG cycles. Five different levels were tested with 65×65, 129×129, 257×257, 513×513 and 1025×1025 grid points corresponding to levels 3, 4, 5, 6 and 7 respectively. Venner and Lubrecht pointed out that for rough contact problems the FMG cycle should be treated with care since it may give bad starting solution for the fine grid solutions [12]. In this case a starting level is defined (as mentioned in Section (5.1)) in order to speed up the convergence. This effect is demonstrated in the figures too, simulations for levels 5, 6 and 7 were done also with a solution starting on level 4.

In the case of *resn* the worst convergence rate was obtained for the level 6 solution starting on the same level 6. This confirms the observations made in [12] that the FMG cycle starting on the finest level yields a bad initial solution. The

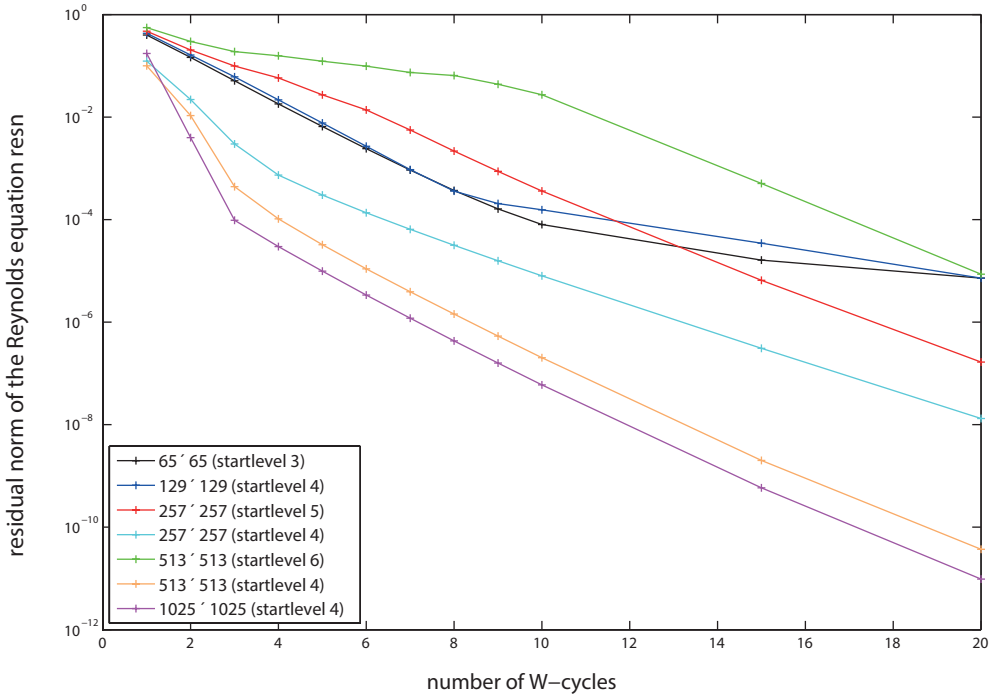

Fig. 6.11 The dependence of the residual norm of the Reynolds equation on the number of W-cycles.

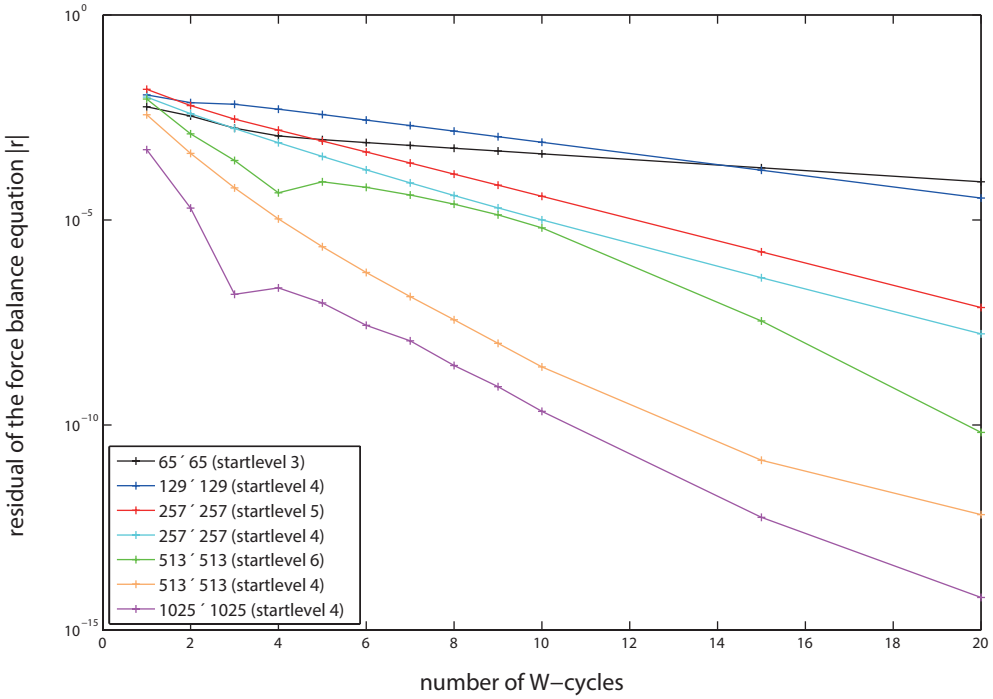

Fig. 6.12 The dependence of the force balance residual on the number of W-cycles.

best convergence rate was obtained for cases when the solution started on a coarser grid. It can be seen in the Figure 6.11 that for all levels the residual norm decreases gradually with increasing number of W-cycles, and with increasing grid points the accuracy increases and the convergence rate is faster. For example, for level 7 the $resn$ is around $\mathcal{O}(10^{-4})$ only after $3W(2,1)$-cycles. The situation is similar for the force balance residual r, although the convergence rate is less steep except for the highest levels 6 and 7. The values of r in Figure 6.12 show for all levels that even one FMG cycle results in residuals around $\mathcal{O}(10^{-2})$ or smaller.

Comparison with other works - Newtonian model

For the same test case as above the values of the dimensionless central H_c and minimum H_{min} film thickness were compared to the values calculated in [12]. The aim was to check the accuracy of the Newtonian model. Table 6.7 presents these values obtained for different levels starting from a grid with 33×33 (level 2) up to a grid with 513×513 (level 6) discrete points. The computational domain was $[-2.5; 1.5] \times [-2; 2]$ and an FMG routine was used with $3W(2,1)$ cycles. The Roelands viscosity-pressure relation and a compressible fluid was assumed. The table contains the results of Venner and Lubrecht from [12], the values obtained by the current solver and the difference between the solutions expressed in percentages. Except for the coarsest grid 2 the difference between the values ranges from 0.44% to 2.18% indicating very good agreement between the two solvers.

Tab. 6.7 Comparison of the central H_c and minimum H_{min} film thickness values with the values in [12] for different grids.

	H_c			H_{min}		
level	Venner and Lubrecht [12]	current solution	difference [%]	Venner and Lubrecht [12]	current solution	difference [%]
2	4.10e-02	3.72e-02	8.73	1.70e-02	1.57e-02	7.81
3	7.10e-02	6.99e-02	1.41	3.31e-02	3.32e-02	0.44
4	7.89e-02	7.72e-02	2.17	3.71e-02	3.67e-02	1.13
5	8.10e-02	7.92e-02	2.18	3.85e-02	3.80e-02	1.24
6	8.15e-02	7.97e-02	2.15	3.88e-02	3.83e-02	1.11

Comparison with other works - Eyring model

The accuracy of the non-Newtonian Eyring model [25] is tested too. Direct comparison can be made with the model of Jacod [30] who implemented the rheology function of the Eyring model also using the effective viscosities (5.66). The friction coefficient in its dimensionless form is used in order to provide the comparison

$$\bar{\mu} = \mu \frac{p_H}{\tau_0} = \frac{\int\int_\Omega \bar{\tau}_m dX dY}{\int\int_\Omega P dX dY} \tag{6.4}$$

The following operating conditions were given in [30]: Moes parameters of load M=500 and material L=6, slide to roll ratio SRR=0.1%, Eyring stress $\tau_0 = 4$ MPa. The Hertzian pressure was 0.789 GPa. Simulations were carried out for four different

grids, for the Roelands viscosity relation (2.20) and an incompressible fluid ($\bar{\rho} = 1$). Results from Table 3.1. in [30] were taken and compared to the results obtained with the current non-Newtonian solver. Table 6.8 summarizes the results and the differences between the two models.

Tab. 6.8 Comparison of the values of the dimensionless friction coefficient (6.4) between the results in [30] and the current solver.

dimensionless friction coefficient $\bar{\mu}$					
level	Jacod [30]		current solver		difference
	$\bar{\mu_J}$	$\lvert\bar{\mu_J}^h - \bar{\mu_J}^H\rvert$	$\bar{\mu_c}$	$\lvert\bar{\mu_c}^h - \bar{\mu_c}^H\rvert$	[%]
3	3.0607		4.1217		9.271
4	2.7562	0.3045	3.8194	0.2742	9.140
5	2.6915	0.0647	3.7426	0.0519	8.850
6	2.6758	0.0157	3.7313	0.0116	8.737

The results show a difference around 9% between the two models which can stem from different sources. It has to be stated that some of the operating conditions, such as α, η_0, R_x or E_r, were not given exactly by [30]. These parameters necessary for the calculations were chosen according to the previous work of the author [93]. The difference between the two models may also lie in the various implementation of the shear stress calculation. Both models exhibit decreasing values of the friction coefficient by a factor 4 or more when the mesh size is halved indicating that it converges with a second order accuracy [30]. The difference between the values of $\bar{\mu}$ obtained on level 3 and 4 is 10.3%, between level 4 and 5 it is 2%, and finally, between levels 5 and 6 it is around 0.5%. These values indicate that calculations on a grid with 257×257 nodes (i.e. level 5) should give sufficiently accurate results.

Comparison with experiments

In Figures 6.8-6.10 a comparison of the numerically calculated and experimentally measured film thickness values was carried out. The Newtonian and the Eyring model were both tested and the results confirm the observations that under pure rolling conditions and for smooth contact problems there is very little or almost no difference between the two rheology approaches. The Newtonian model can provide sufficiently accurate prediction and can be used for smooth contact simulations. When comparing to the measured values all three figures show that with decreasing mean speed the difference between the experiments and simulations increases. From 0.4 m/s to 0.125 m/s the differences are at maximum 11.4% for the h_c and at maximum 12.3% for the h_{min}. For lower speeds, i.e. under 0.08 m/s they vary between 12% and 25%, while the biggest difference of 32% was observed for the highest load case 3 and smallest mean speed 0.01 m/s (corresponding to M=1339 and L=4.15). Table 6.9 gives the differences in percentage for some of the simulations. The difference was calculated as $|h_{exp} - h_{num}| / h_{exp}$. The increasing difference between the numerics and experiments at low speeds was studied by [137] who pointed out that at low speeds very dense grids might help.

Tab. 6.9 Differences in [%] between the experimentally measured values of h_c and h_{min} and numerical simulations with the Newtonian model.

	h_c [nm]		
case	experiment	Newtonian model	difference [%]
load case 1, $u_m = 0.01$[m/s]	72	59.5	17.3
load case 1, $u_m = 0.4$[m/s]	696	668.9	3.9
load case 3, $u_m = 0.01$[m/s]	58.6	44.8	23.5
load case 3, $u_m = 0.4$[m/s]	655.7	620.5	5.36
	h_{min} [nm]		
case	experiment	Newtonian model	difference [%]
load case 1, $u_m = 0.01$[m/s]	35	28.3	19.1
load case 1, $u_m = 0.4$[m/s]	523	486.7	6.9
load case 3, $u_m = 0.01$[m/s]	19	12.9	32.1
load case 3, $u_m = 0.4$[m/s]	365	343.2	5.9

6.1.4 Concluding remarks

From the previous section the following conclusions can be drawn:

- the smooth EHL point contact solver designed and implemented as described in Chapter 5 was verified and compared with results of previously published works and experimentally measured film thickness values. The results indicate that the current solver is sufficiently accurate. The differences between the experiments and calculations can stem from different sources, such as the discretization order, number of iterations, grid density, the accuracy of the rheology models or the differences in the input parameters (e.g. α).
- The multigrid FMG algorithm can yield accurate results even after a few W-cycles, however, the convergence rate is sensitive to the choice of the starting level. The values of the residual norm confirm this observation. Better accuracy can be achieved by starting on a coarser grid than the finest level.
- The simulations confirmed the characteristic features of the film thickness and pressure distributions mentioned in Chapter 2.
- The choice of the viscosity and density relations is very important in the calculation. The use of the Barus relation (2.19) increases the height of the pressure spike, the assumption of the compressible fluid results in lower film thickness and reduced pressure spike.
- Under pure rolling conditions and for smooth surfaces the Newtonian model is sufficiently accurate.
- The Eyring model gives the same results with low sliding values as the Newtonian model - see Figures 6.8-6.10.
- The largest differences between the experimental and numerical values of h_c and h_{min} are obtained for the lowest examined mean velocities. Generally, the differences were larger when comparing the minimum film thickness values, the largest difference 32% was obtained for the lowest mean velocity (0.01 m/s)

and highest load (73 N) which corresponds to Moes parameter of load M=1339. With increasing mean velocity, which corresponds to decreasing parameter M (see Table 6.3), the agreement is improved.

- The accuracy of the Eyring model was compared with previously published results in [30]. The friction coefficient was calculated and compared for a given set of operating conditions. The differences between the results are around 9% which may be caused by the slightly different operating conditions used in the current simulations, but also can stem from the differences in implementation.
- The accurate implementation of the non-Newtonian fluid rheology model and the incorporation of the rheology function describing the non-Newtonian behavior is very complicated. The non-linear dependence between the shear rate and shear stress causes that the shear stress values across the film thickness have to be integrated resulting in an increased computational time. The analytical expressions of these integrals are not available and at every grid point extra integrations over the film thickness have to be done. Nevertheless, the so-called effective viscosities enable to solve the non-Newtonian model in a simplified way. The expressions of these effective viscosities can be easily calculated using a definition for the mean shear stress (in case of the Eyring model). A question arises concerning the accuracy of the Eyring model in its simplified form - whether it is able to predict the shear-thinning behavior of a lubricant in an EHL model. This issue was already addressed by several authors such as Bair [36] or Kumar [35]. Though the problem is complicated, various rheology models were proposed to solve the line contact problem. On the other hand more work has to be done in order to derive an accurate rheology model which might be used for the two-dimensional models too. For the stationary smooth contact problem the Newtonian model is satisfactory but in order to study the rough contact problems the influence of non-Newtonian effects on the EHL parameters should be investigated in more detail.

In the following part results with a surface roughness problem are presented. The effect of the non-Newtonian lubricant model on the surface roughness are investigated. The numerical model assumes the Eyring law. The reason why the Eyring model was chosen lies in the simplified derivation of its rheology function and its simplified inclusion to the Reynolds equation in terms of effective viscosities.

6.2 Non-smooth EHL results

The current part presents results of simulations with a surface feature. The geometry of the surface feature was defined in Chapter 5. Both surfaces move, therefore the problem is non-stationary and the time variable t is defined. The numerical solver of the smooth contact model is extended such that the model is solved in each time step. The first time step at $t = 0$ solves the problem with an FMG cycle in order to gain a good starting solution. For the rest of the time steps t F-cycles are applied (see Figure 5.6 in Section 5.1). Simulations with both rheology models (the Newtonian and the non-Newtonian Eyring model) were carried out, their definition is the same as for the stationary solver.

6.2.1 Operating conditions

First, the geometry of the surface feature is defined. A single transverse flat-top ridge is assumed throughout the simulations. Its implementation was described in Chapter 5. Figure 6.13 compares the shapes of the experimentally used ridge with the shape used in the numerical calculations. In the model the geometry of the ridge is defined by the following parameters: the height is $H_d = 200$ nm, the base width of the ridge $W_1 = 45$ μm and the top width $W_2 = 20$ μm.

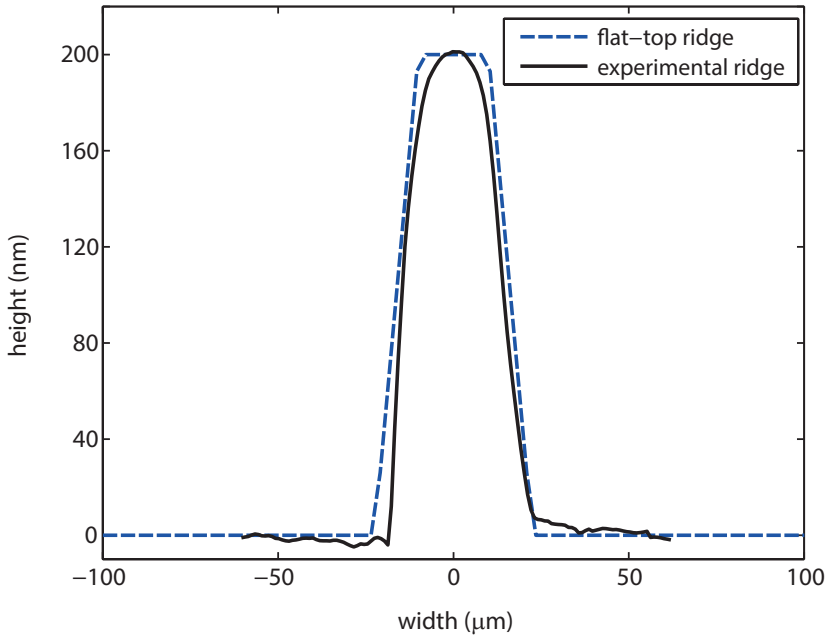

Fig. 6.13 Model of the flat top ridge and the shape of the ridge used in the experiments. Height $H_d = 200$ nm, bottom width $W_1 = 45$ μm and top width $W_2 = 20$ μm.

The rest of the input parameters (materials, contact geometry, etc.) were defined in Section 6.1 simulating the smooth contact case - see Table 6.2. If not defined otherwise, in all calculations a load of 30 N is assumed corresponding to Hertzian pressure $p_H = 0.566$ GPa. The numerical parameters required in the calculations are identical to the ones needed in the smooth solver. Additionally, the size of the time step h_t needs to be specified.

6.2.2 Time-dependent calculations

First, the passage of the ridge through the contact zone is illustrated. Figures 6.14 and 6.15 each display film thickness and pressure distributions at $y = 0$ (on the left) and interferometry plots of the film thickness: numerically calculated pseudo-interferometry plots (in the middle) and experimentally measured film thickness interferometry plots (on the right) for three different time steps and for different locations x_d of the ridge. The simulations were carried out with the non-Newtonian Eyring model for a mean velocity $u_m = 0.08$ m/s. The two calculations were done with different values of slide to roll ratio (defined in Equation (6.1)). In the first case, Figure 6.14 presents results with a positive SRR = 100%, i.e. the surface with the ridge is slower. The opposite case, i.e. when the slide to roll ratio is negative, i.e. SRR = −100%, is shown in Figure 6.15. The rest of the operating conditions can be found in the previous section.

The full numerical solutions for rolling-sliding contacts reveal the previously observed characteristics of the film thickness and pressure distributions which were already described and presented in Section 2.4.

Figure 6.14 shows the case when the surface with the ridge is three times slower than the smooth surface. Figure 6.14a shows the pressure and film thickness for the time moment when the roughness is well outside the contact zone ($x_d = -417.5$ μm) and the distributions look like the typical smooth contact problem. The next Figure 6.14b depicts the time step when the ridge is already inside the contact zone at position $x_d = -83.5$ μm. The film variation generated at the inlet traveling with the mean velocity is in front of the film variation caused by the moving steady state solution of the ridge. In the interferometry plots the complementary wave is recognizable too as a half-moon shaped restriction. The third Figure 6.14c presents the time step ($x_d = 83.5$ μm) when the complementary wave already left the contact zone and only the variations caused by the roughness are present passing through the contact unchanged.

The opposite case, i.e. when the ridge is three times faster than the smooth surface is illustrated in Figure 6.15. Again, the first Figure 6.15a shows the moment when the ridge is outside the contact zone at location $x_d = -417.5$ μmand the film thickness and pressure distributions look like the smooth contact distributions. The other two Figures 6.15b-c show time steps at locations $x_d = 83.5$ μm and $x_d = 125.25$ μmin which cases the faster moving roughness already overtook the complementary wave generated at the inlet. The distance between the two features increases as the roughness passes through the contact zone. The film thickness variation generated by the moving steady state solution leaves the contact first, while the complementary function lags behind. Again, the interferometry plots reveal the half-moon shaped restriction but this time with an opposite orientation and it is behind the ridge.

The calculations indicate that the two components can be observed separately, i.e. the roughness caused behavior can be studied independently from the complementary function. The deformation of the ridge and the effect of the different operating conditions on this deformation will be studied in the following sections but first the role of the rheology model has to be investigated.

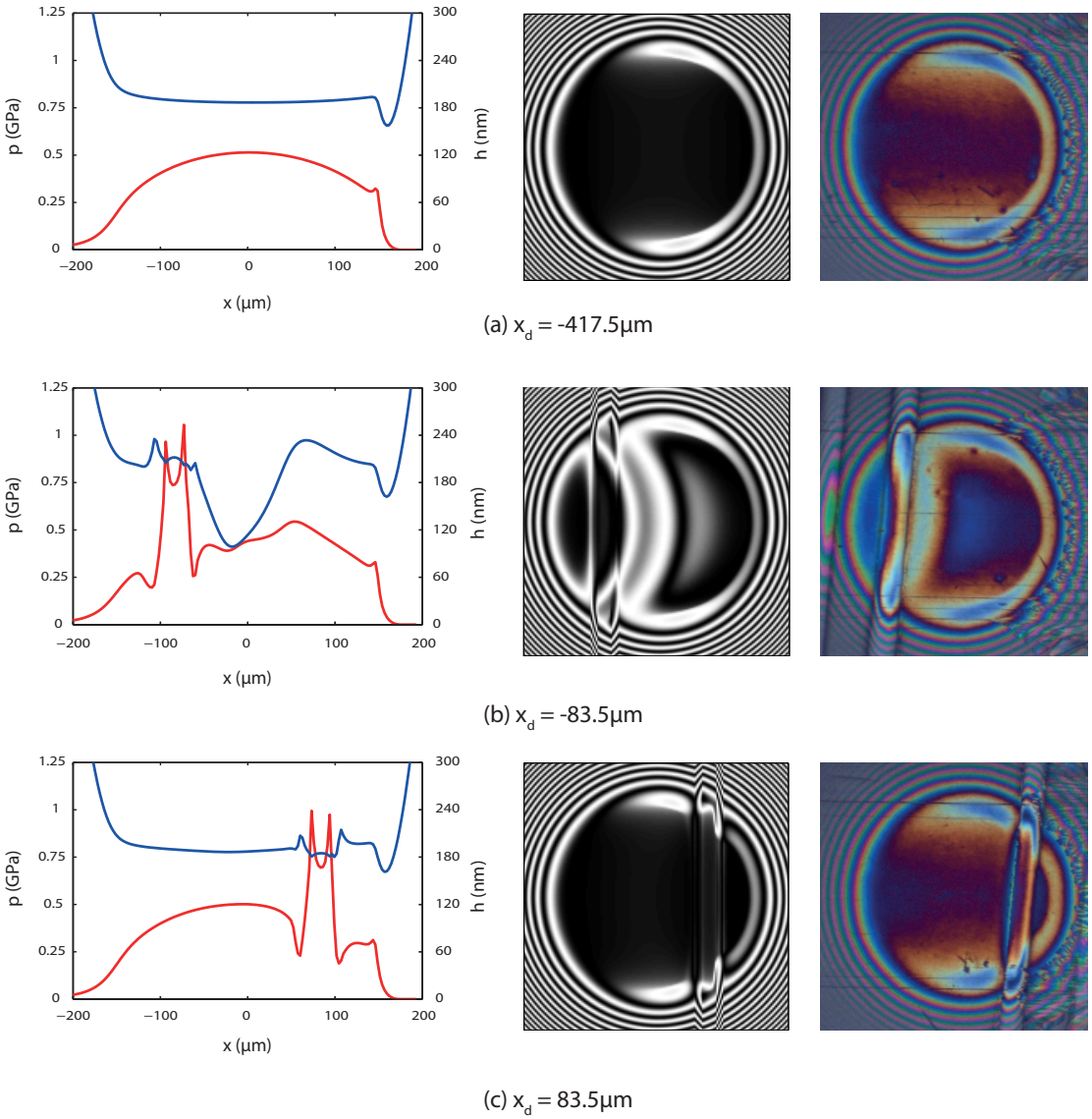

Fig. 6.14 Film thickness (blue line) and pressure (red line) distributions (left), pseudo-interferometry (center) and interferometry (right) plots of film thickness under rolling-sliding conditions in an EHL point contact with a flat-top surface roughness for three different locations of the ridge x_d. The operating conditions were: SRR = 100%, $u_m = 0.08$ m/s. From the top to the bottom: (a) $x_d = -417.5$ μm, (b) $x_d = -83.5$ μm, (c) $x_d = 83.5$ μm.

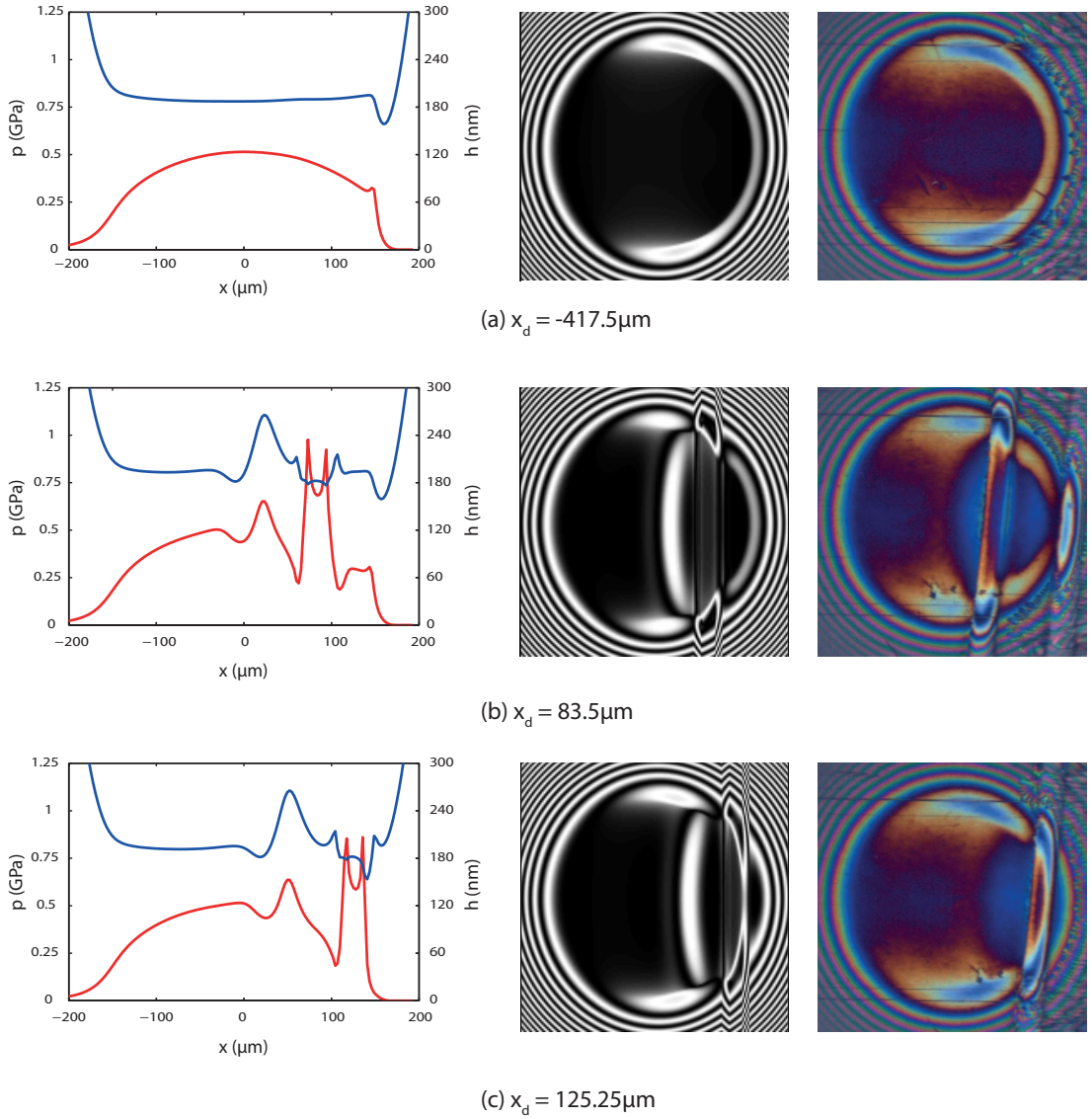

Fig. 6.15 Film thickness (blue line) and pressure (red line) distributions (left), pseudo-interferometry (center) and interferometry (right) plots of film thickness under rolling-sliding conditions in an EHL point contact with a flat-top surface roughness for three different locations of the ridge x_d. The operating conditions were: SRR $= -100\%$, $u_m = 0.08$ m/s. From the top to the bottom: (a) $x_d = -417.5$ μm, (b) $x_d = 83.5$ μm, (c) $x_d = 125.25$ μm.

6.2.3 Comparison of the fluid rheology models

For a given set of operating conditions the two rheology functions (the Newtonian (5.57) and the non-Newtonian Eyring (5.66)) are compared for pure rolling, positive (SRR = 100%) and negative (SRR = −100%) rolling-sliding conditions. The parameters of SR 600 oil are used (see Table 6.11), the mean velocity was 0.08 m/s. The second order narrow-upstream (NU2) discretization scheme implemented in these models was presented in Chapter 5.4. The second order scheme uses the values of two previous time steps $t-1$ and $t-2$. The calculations were done on a grid with 257×257 discrete points on domain $[-2.5; 1.5] \times [-2; 2]$ which is equal to a spatial mesh size $h_x = h_y = 0.015625$. The solutions were calculated with a time step half of the spatial step $h_t = 0.5h_x = 0.0078125$.

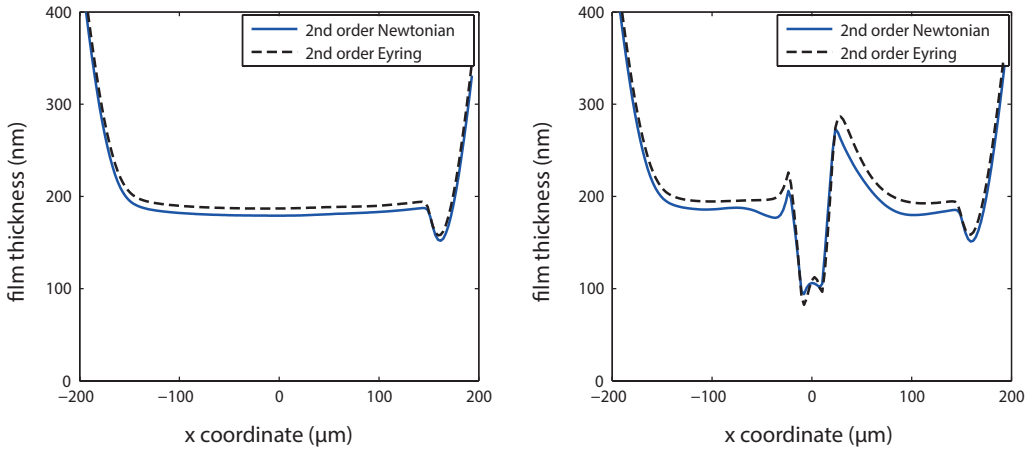

Fig. 6.16 Pure rolling SRR = 0: film thickness calculated using the second order Newtonian model and the second order Eyring model at ridge location $x_d = -225.45$ μm (on the left) and $x_d = 0$ μm (on the right).

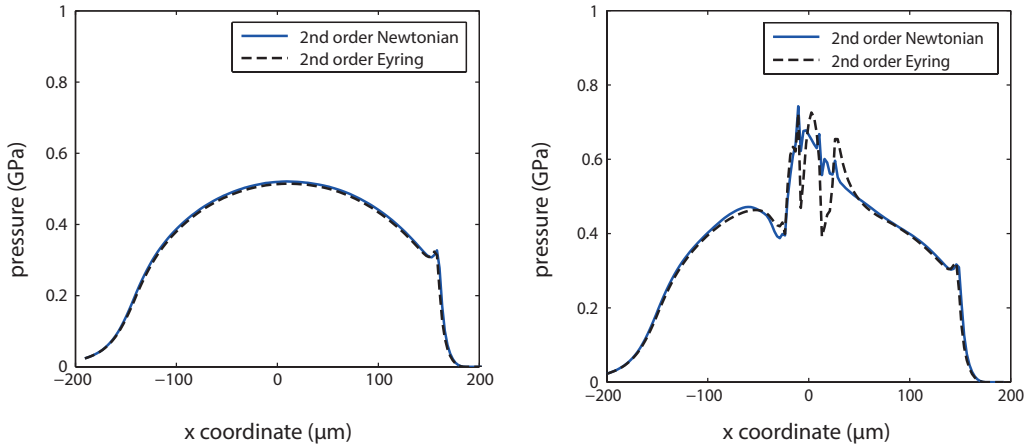

Fig. 6.17 Pure rolling SRR = 0: pressure distribution calculated using the second order Newtonian model and the second order Eyring model at ridge location $x_d = -225.45$ μm (on the left) and $x_d = 0$ μm (on the right).

Figures 6.16-6.21 show the film thickness and pressure distributions for two different time steps and compare the results of the two solvers. Figures 6.16 and 6.17 assume conditions under pure rolling, here, the non-Newtonian model was simulated with a small SRR of 5%. Figures 6.18-6.19 show the case of positive SRR, while Figures 6.20-6.21 the case of negative SRR.

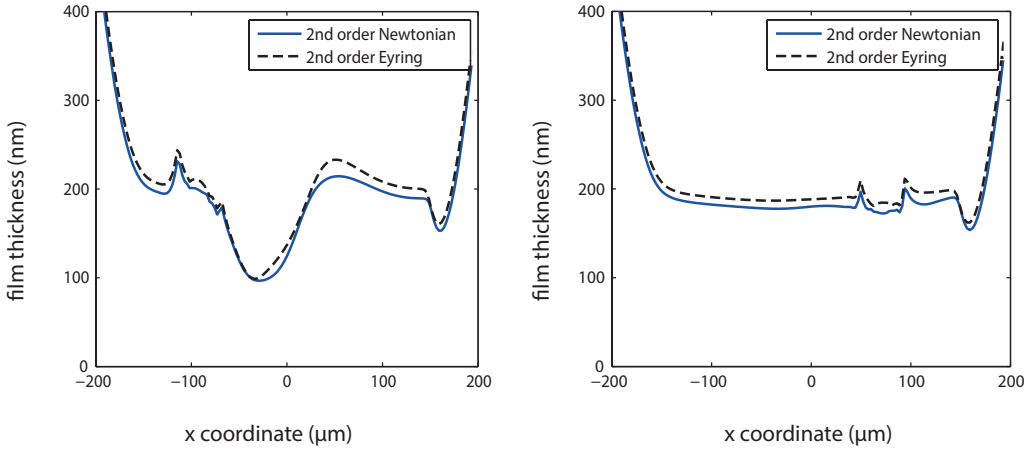

Fig. 6.18 Rolling-sliding SRR = 100%: film thickness calculated using the second order Newtonian model, and the second order Eyring model at ridge location $x_d = -100.2$ μm (on the left) and $x_d = 83.5$ μm (on the right).

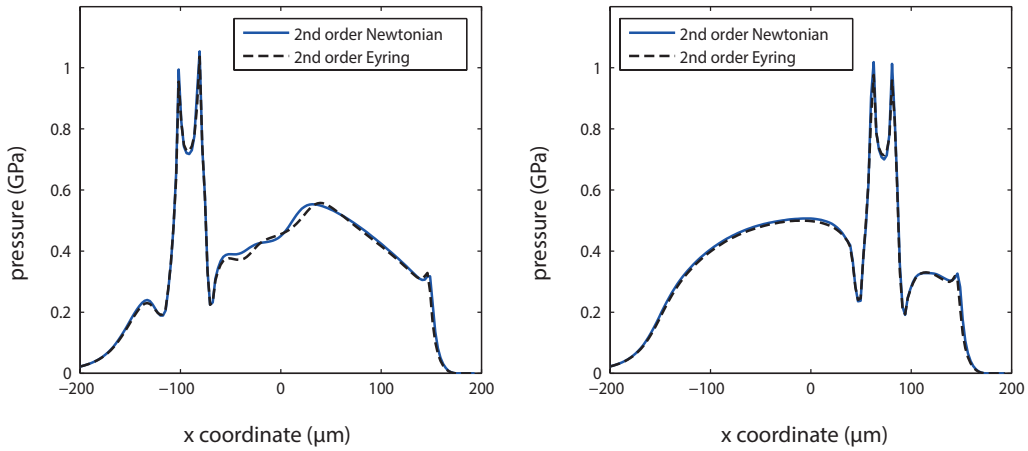

Fig. 6.19 Rolling-sliding SRR = 100%: pressure distribution calculated using the second order Newtonian model, and the second order Eyring model at ridge location $x_d = -100.2$ μm (on the left) and $x_d = 83.5$ μm (on the right).

Under pure rolling the two models predict approximately similar behavior of the ridge which confirms the fact that under pure rolling the Newtonian model is sufficiently accurate. Slightly higher central film thickness is predicted by the Eyring model but the magnitude of the deformation and the shape of the deformed ridge is the practically the same for both models. The pressure distribution is the same for both models when the surface roughness is outside the contact zone, on the other hand when the roughness is inside the contact the pressure variations are different around the ridge. The Eyring model predicts larger pressure gradients. This is shown on the right of Figure 6.17.

For positive SRR (the rough surface is slower) the Newtonian model predicts lower deformation around the ridge but higher pressure variations. For negative SRR the pressure gradients are again higher for the Newtonian model and the deformation is lower for this case as well. For both SRRs the height of the complementary function is slightly larger for the Eyring model.

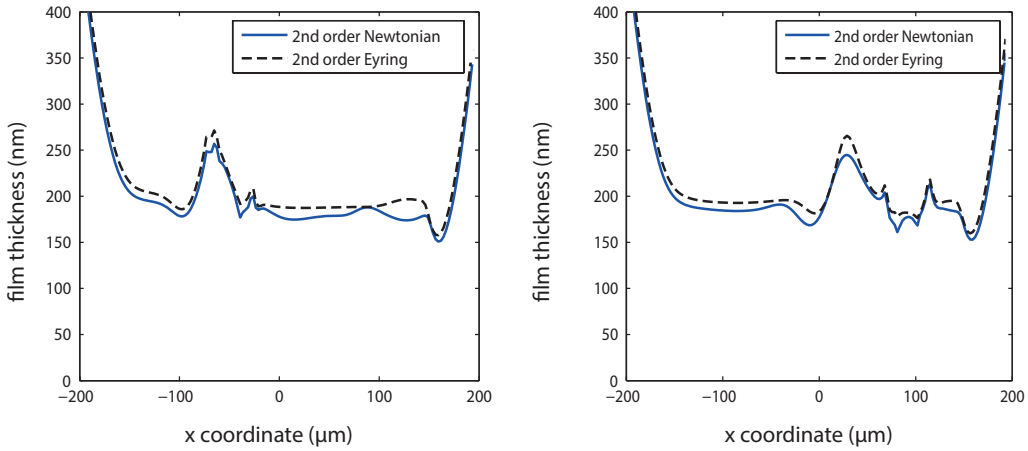

Fig. 6.20 Rolling-sliding SRR = −100% - film thickness calculated using the second order Newtonian model, and the second order Eyring model at ridge location $x_d = -83.5$ μm (on the left) and $x_d = 83.5$ μm (on the right).

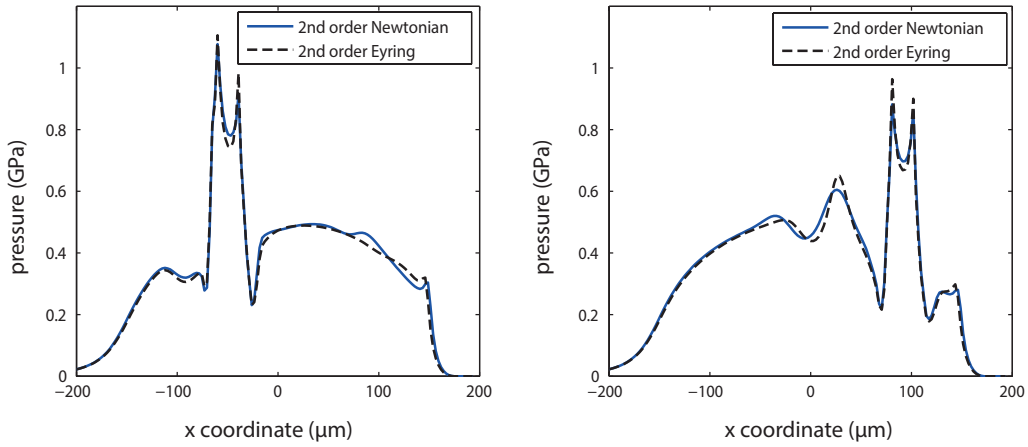

Fig. 6.21 Rolling-sliding SRR = −100% - pressure distribution calculated using the second order Newtonian model, and the second order Eyring model at ridge location $x_d = -83.5$ μm (on the left) and $x_d = 83.5$ μm (on the right).

6.2.4 Effect of mean entrainment velocity and the slide to roll ratio

Surface roughness deforms inside the contact causing film thickness and pressure variations. This characteristic behavior was shown in the previous sections. The behavior is different under pure rolling and rolling-sliding conditions. When the

velocities of both surfaces are equal, the roughness induced variations and the complementary function move together with the same mean velocity u_m. Under sliding conditions the roughness and the complementary wave do not move together. Based on the value of the SRR (positive or negative) the complementary function can gradually overtake the roughness or lag behind it which enables to study the deformed roughness profiles separately.

Tab. 6.10 The range of mean velocities used in the calculations and the corresponding Moes parameters of load and material.

mean velocity u_m (m/s)	parameter of load M	parameter of material L
0.01	698.38	3.84
0.02	412.88	4.57
0.04	245.50	5.43
0.08	145.98	6.46
0.095	128.32	6.75

The current section presents simulations and comparison with experimentally measured film thickness. The effect of different operating conditions, such as the mean velocity u_m and the SRR, on the magnitude and shape of the roughness deformation is examined. A range of mean velocities $u_m = \{0.01, 0.02, 0.04, 0.08, 0.095\}$ m/s and slide to roll ratios SRR=$\{\pm 50\%, \pm 70\%, \pm 100\%, \pm 150\%\}$ was chosen for which full simulations were carried out. The corresponding values of the dimensionless Moes parameters for each entrainment velocity are given in Table 6.10.

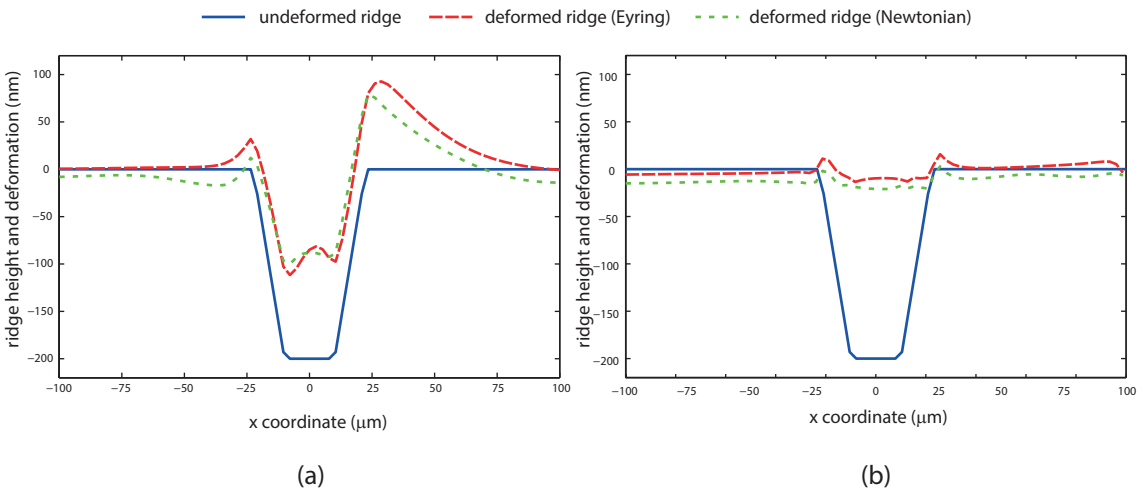

Fig. 6.22 Comparison of the undeformed (blue solid line) and deformed ridge profiles for $x_d = 0$ μm for both rheology models (Eyring (red dashed line) and Newtonial (green dashed line) model): (a) pure rolling, (b) rolling-sliding conditions (SRR = 100%). The inlet is on the left.

In order to illustrate the magnitude of the roughness deformation the original undeformed and deformed profiles of the ridge are shown in Figure 6.22. Figure 6.22a compares the profiles under pure rolling, Figure 6.22b shows the same comparison

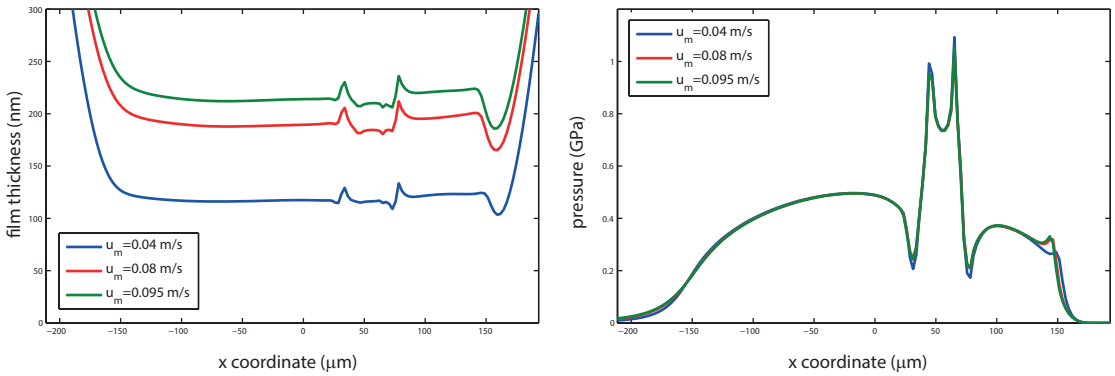

Fig. 6.23 Film thickness for SRR = 100% and for different velocities u_m = 0.04, 0.08, 0.095 m/s.

for rolling-sliding conditions (SRR=100%). The deformed profiles are shown for both Newtonian and non-Newtonian fluid models.

Figure 6.23 presents the whole contact zone with the film thickness and pressure distributions for a range of mean velocities for a given SRR and at a given time instance. The rolling direction is from the left to the right (i.e. the inlet is on the left) in the figures. While the central value of the film thickness increases with increasing mean velocity, the deformed shape of the ridge is approximately the same (left of Figure 6.23). It can be seen on the right of Figure 6.23 that the pressure distributions are practically the same. Instead of showing the whole contact zone only the film thickness around the location of the deformed ridge will be shown in the next figures.

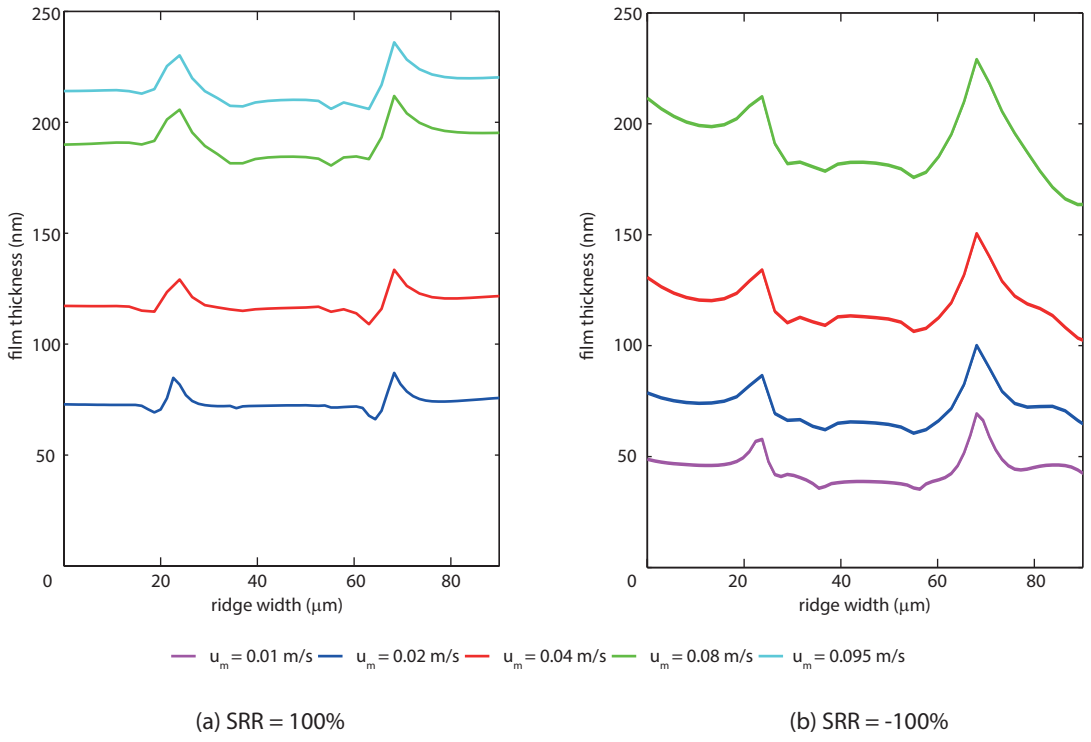

Fig. 6.24 Ridge deformation under SRR = 100% and SRR = −100% for different mean velocities u_m = 0.01, 0.02, 0.04, 0.08, 0.095 m/s. The inlet is on the left.

Deformation is studied with both positive (i.e. when the smooth surface is faster) and negative (i.e. when the smooth surface is slower) SRRs. In the case of a slower rough surface the ridge is overtaken by the complementary function which is induced at the inlet and leaves the contact zone first. After that, the ridge passes through the contact zone unchanged. For negative SRR the situation inside the contact is opposite, i.e. the ridge leaves the contact first and the complementary function lags behind the ridge.

The following simulations were carried out on a grid with 257×257 nodal points except for the lowest mean velocities. As the Moes parameters indicate, the lowest speeds (0.01 and 0.02 m/s) represent severe conditions especially for a rough surface. For these two mean velocities converged solutions were obtained only with 513×513 grid points. The relaxation factors had to be chosen with great care: the convergence of the Reynolds equation's residuals (6.2) was very sensitive to the choice of the relaxation factor ω_{H_0}, its value was chosen below 0.01. The Gauss-Seidel relaxation factor ω_{gs} ranged from 0.1 to 0.4, the Jacobi relaxation factor ω_{ja} ranged from 0.05 to 0.3. For the lowest speeds the number of F-cycles had to be increased as well (6 or more cycles).

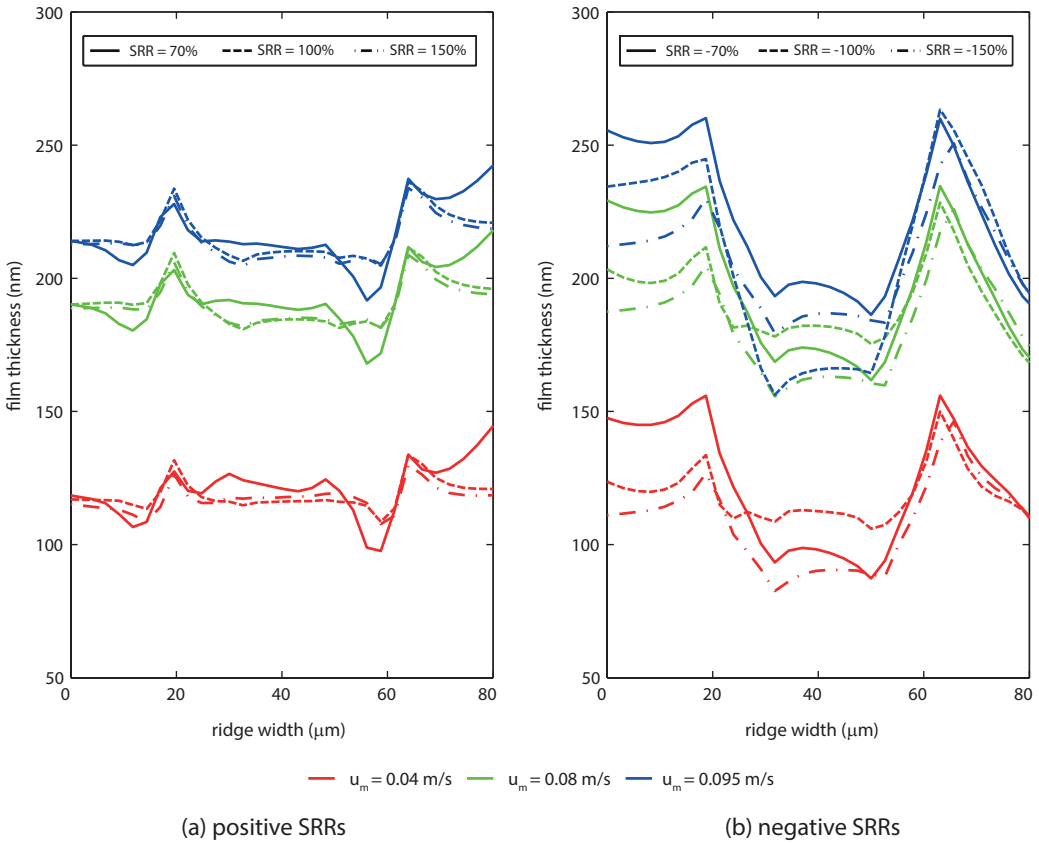

Fig. 6.25 Ridge deformation for a range of different positive (on the left) and negative (on the right) SRR and for mean velocities $u_m = 0.04, 0.08, 0.095$ m/s. The inlet is on the left.

The effect of the mean velocity is studied first. While Figure 6.24a shows the film thickness variations around the ridge for velocities 0.02, 0.04, 0.08 and 0.095 m/s for positive SRR = 100%, Figure 6.24b depicts the film thickness variations for

a negative SRR = −100% and for speeds 0.01, 0.02, 0.04 and 0.08 m/s. For both cases the ridge is heavily deformed (as was illustrated in Figure 6.22).

It can be seen that the deformed ridge profiles are very similar for a given SRR. Around the edges of the ridge, in front of the ridge and behind it, locally enhanced regions of lubricant can be seen. The shape of the deformed ridges do not vary extremely with increasing or decreasing mean velocity. The size of the deformation is slightly increasing with decreasing mean velocity (or film thickness). Similar behavior of the ridge was observed for other values of the slide to roll ratio.

Next, the effect of SRR on the deformation is presented. For a given value of mean velocity different (either positive or negative) values of the SRR were compared. Figure 6.25 shows the deformation for mean velocities 0.04, 0.08 and 0.095 m/s and SRRs ±70%, ±100% and ±150% (positive SRRs on the left, negative SRRs on the right). For positive SRR the shape of the deformed ridge and the height of the deformation at the edges are practically the same for SRR=100% (dashed line) and SRR=150% (dotted-dashed line) while for SRR=70% (solid line) the deformed shape beneath the ridge is higher and a larger film thickness constriction around the leading edge is present. When the ridge is on the faster surface minor variations in the deformed shape of the ridge can be seen for every negative SRR at a given mean speed. The size of the deformation is slightly increasing with decreasing mean speed for a given SRR.

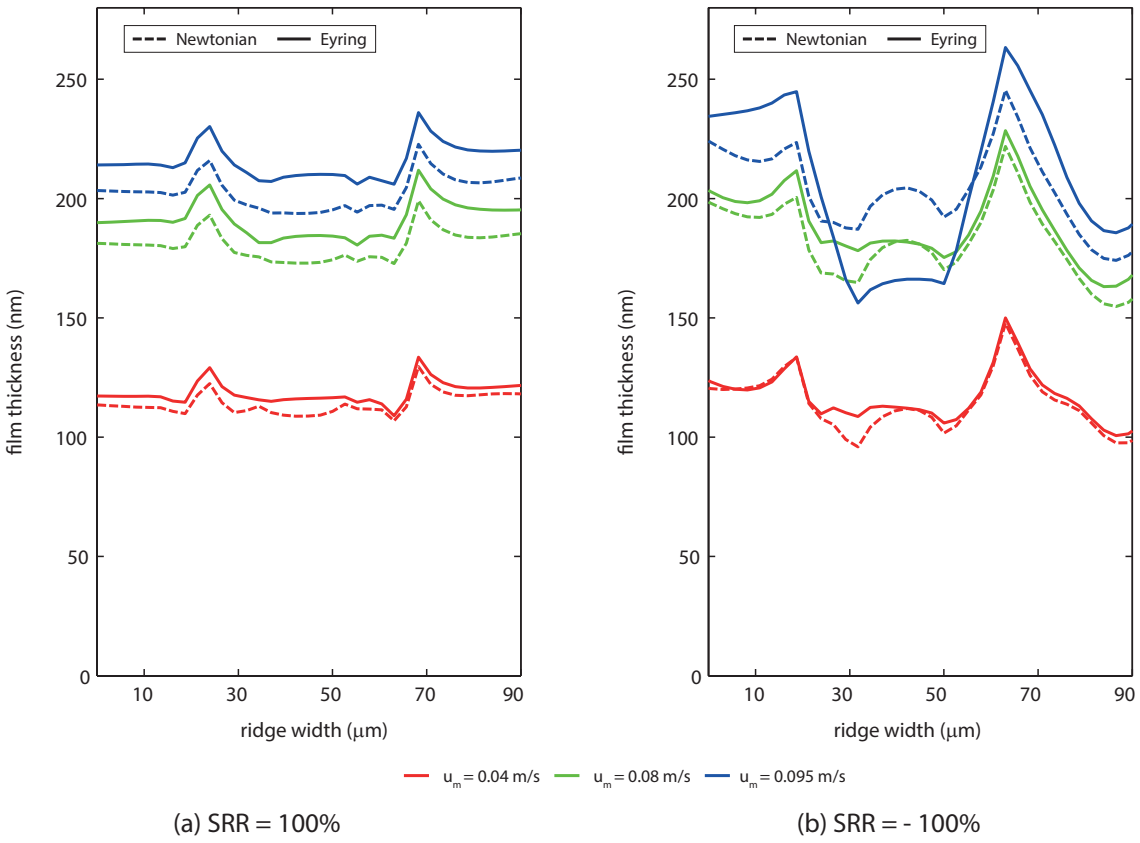

Fig. 6.26 Ridge deformation under SRR = 100% and SRR = −100% for different mean velocities $u_m = 0.04, 0.08, 0.095$ m/s with the inlet on the left. Comparison of Newtonian (dashed line) and Eyring models (solid line).

Comparison with the Newtonian model

Simulations were done with the Newtonian model for the same operating conditions and were compared to the results with the Eyring model presented in the previous section. Figure 6.26 presents the deformed ridge profiles for SRR = ±100% and for mean velocities 0.04, 0.08 and 0.095 m/s.

The agreement between the two models is better when the ridge is on the slower surface (positive SRR - Figure 6.26a). The shape and magnitude of the deformed profiles calculated by the Newtonian model (dashed line) are practically the same as with the Eyring (solid) model although the central film thickness is larger for the Newtonian model for each mean velocity (this tendency was already observed in Section 6.2.3). When the ridge moves faster through the contact area the rheology models predict different shape of the deformed ridge. With Newtonian model (dashed line) there is a noticeable deflection in the middle of the profile which is not present when the Eyring model (solid line) is used.

Comparison with experiments

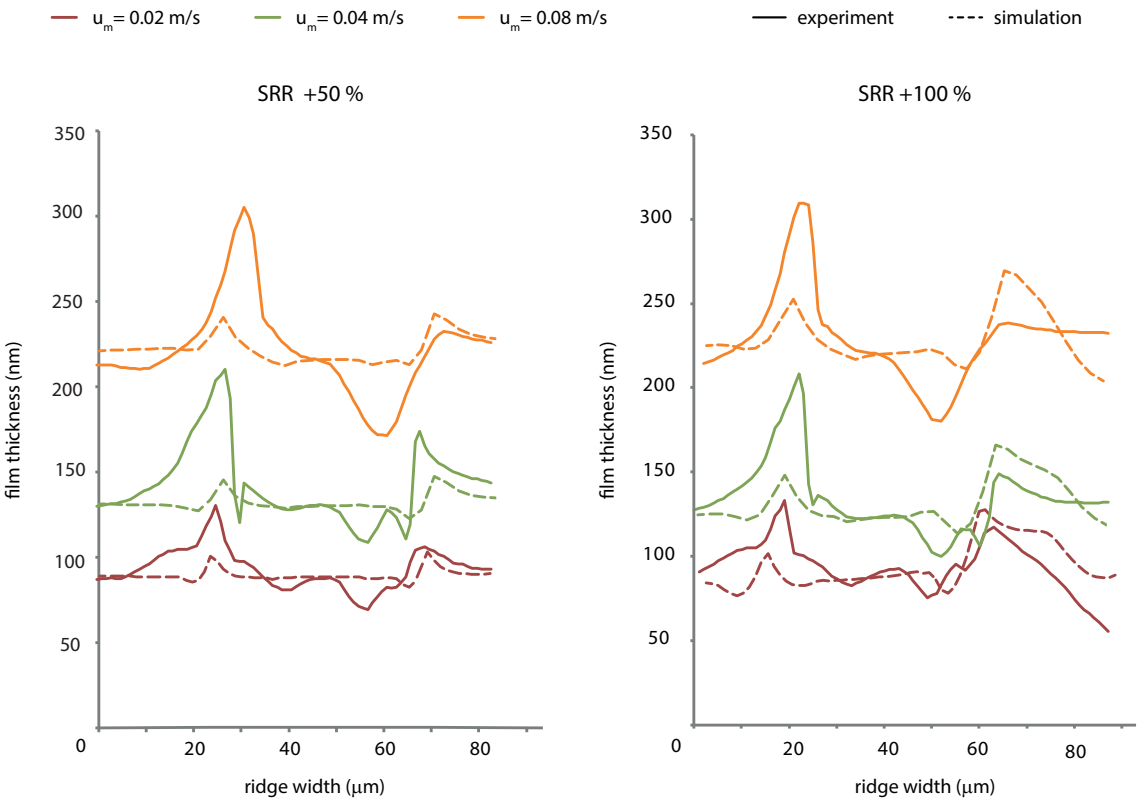

Fig. 6.27 Comparison of the experimentally measured (solid lines) and numerically simulated (dashed lines) deformed ridges for SRR = 50% and SRR = 100% for three mean velocities u_m=0.02, u_m=0.04 and u_m=0.08 m/s.

Comparison with experimentally measured film thickness values was done for the presented range of operating conditions. The Eyring model was assumed in the simulations since when the contacts operate under rolling-sliding conditions the lubricant exhibits non-Newtonian behavior. Each figure presents comparison of the

experimental and simulated deformed ridge for a given SRR and a range of mean velocities. In each figure the inlet is on the left, the solid lines mark the experimental results and the dashed lines stand for the numerical simulations. Figures 6.27 and 6.28 compare the deformed profiles of the ridge when it is placed on the slower surface (positive SRR), Figure 6.29 compares the deformed ridges for negative SRR, i.e. a faster roughness.

For positive SRR the experimental measurements show that the deformed ridge is independent of the SRR and a change in the mean velocity influences the deformation only slightly. The experimentally measured film thickness values show an increased amount of lubricant accumulated at the trailing edge of the ridge with increasing mean velocity. Simulations showed that the deformation is only slightly dependent on the SRR, moreover it can be seen that the mean velocity has an influence on the deformed shape. Comparing the two sets of results one can see a difference in the prediction of the size of the deformation right behind the ridge at the trailing edge where the experiments predict higher values of entrapped lubricant. Visible constriction beneath the ridge was observed by the experiments which was not present in the simulations. The simulations predict higher amount of lubricant entrapped at the trailing edge than in front of the ridge.

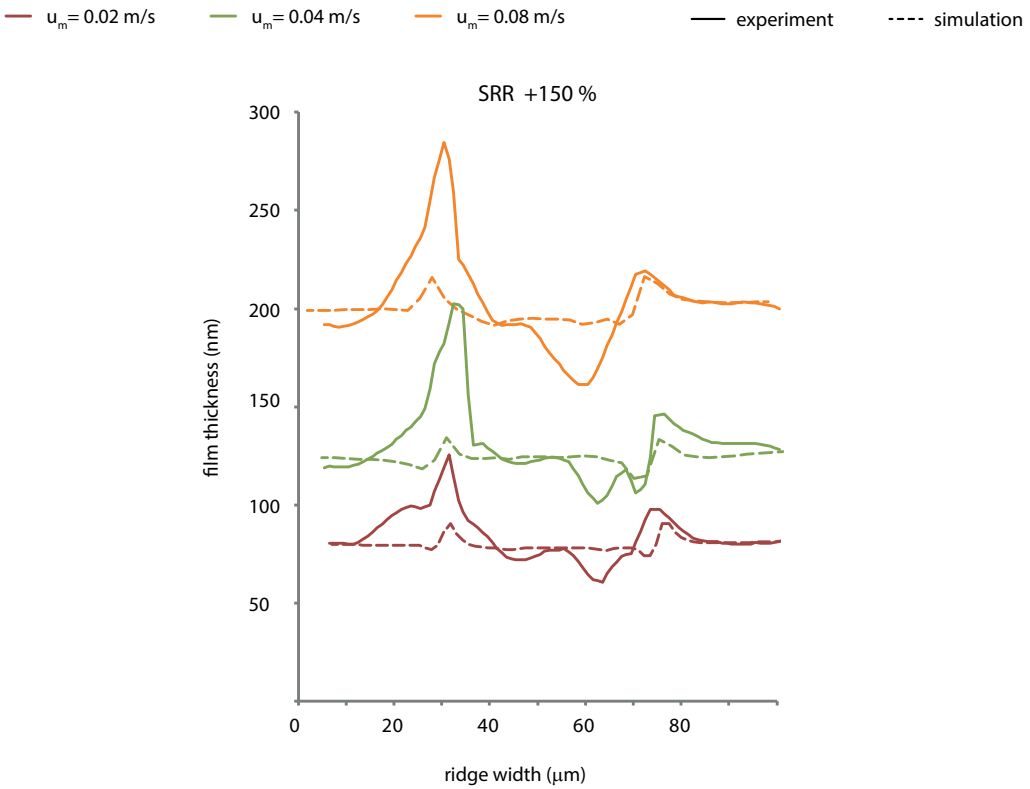

Fig. 6.28 Comparison of the experimentally measured (solid lines) and numerically simulated (dashed lines) deformed ridges for SRR = 150% for three mean velocities u_m=0.02, u_m=0.04 and u_m=0.08 m/s.

Figures with negative SRR show fair agreement between the experiments and simulations for SRR $= -100\%$ and SRR $= -150\%$. For lower values of SRR, e.g. SRR $= -50\%$, the separation of the deformed profile from the complementary function was not as straightforward as for higher values of sliding which caused

that it was not possible to study the deformed shape separately. Therefore these cases were omitted in the current work. The results in Figure 6.29 indicate that the deformation is independent of the sliding speed SRR. The closest agreement between the simulations and experiments was found for the lowest mean velocities. For mean velocity $u_m = 0.08$ m/s the results are different for every SRR.

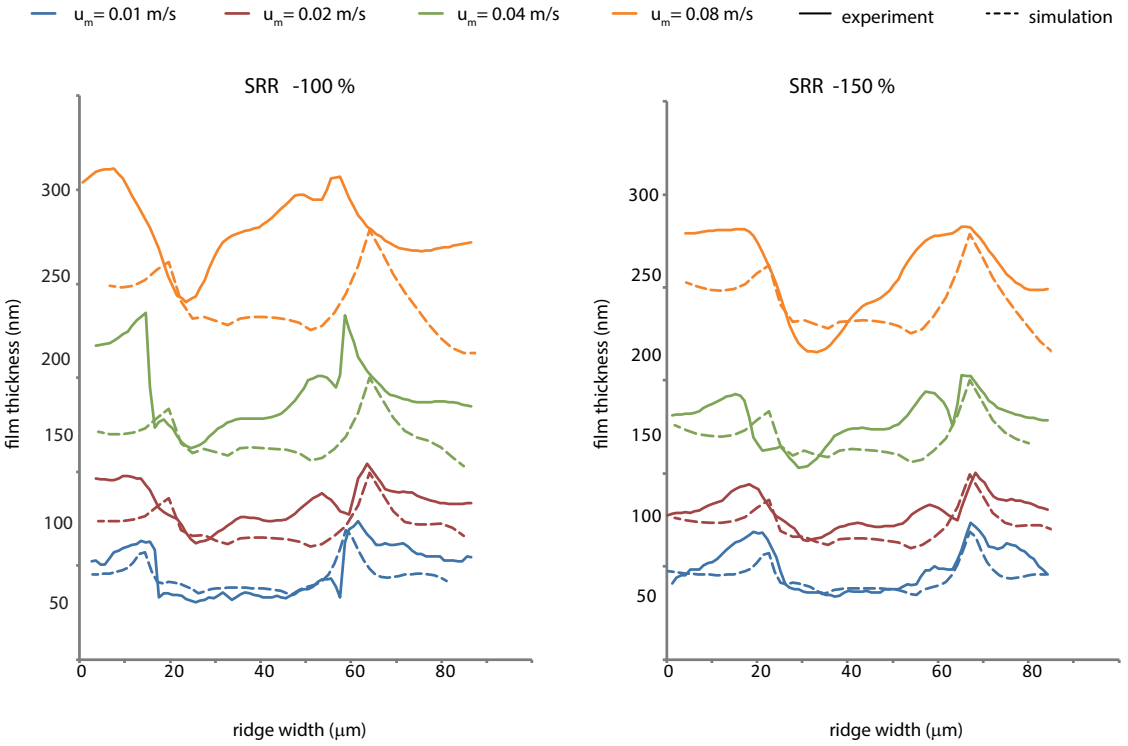

Fig. 6.29 Comparison of the experimentally measured (solid lines) and numerically simulated (dashed lines) deformed ridges for SRR $= -100\%$ and SRR $= -150\%$ for four mean velocities u_m=0.01, u_m=0.02, u_m=0.04 and u_m=0.08 m/s.

6.2.5 Effect of oil parameters

The current section compares the deformed ridge for three different lubricants. First is a mineral base oil, SR 600, the second is synthetic base oil, polyalpha olefin, PAO 100, and the third fluid is a simple hydrocarbon, glycerol. Their parameters are given in Table 6.11. The effect of different lubricant properties on the deformation is studied.

Tab. 6.11 The parameters of the oils assumed in the calculations: SR 600, PAO 100 and glycerol.

Oil	SR 600	PAO 100	glycerol
pressure-viscosity coefficient α (GPa^{-1})	24	20	5
viscosity at ambient pressure η_0 (Pa s)	0.22	1.8	0.46
Eyring stress τ_0 (MPa)	5	0.1	2.5

A steel ball - glass disc configuration was used, the material and geometry properties of the contacting bodies were given in Table 6.2. The load was 55 N which corresponds to Hertzian pressure 0.63 GPa and Hertzian radius 204 μm. In the

experiments a step-like flat-top ridge was used, i.e. its base and top widths were equally 40 μm. The height of the roughness was 190 nm. The same values were assumed in the numerical model. Simulations with the non-Newtonian model were carried out for three different mean velocities which correspond to the smooth central film thickness values of 150, 250 and 350 nm. The values of mean velocities for each lubricant are different, Table 6.12 summarizes their values. The slide to roll ratio was 120% in each calculation.

Tab. 6.12 Central film thickness values and corresponding mean velocities for the three lubricants: SR 600, PAO 100 and glycerol.

	SR 600	PAO 100	glycerol
h_c (nm)	u_m (m/s)		
150	0.064	0.0115	0.1
250	0.133	0.026	0.215
350	0.2145	0.048	0.37

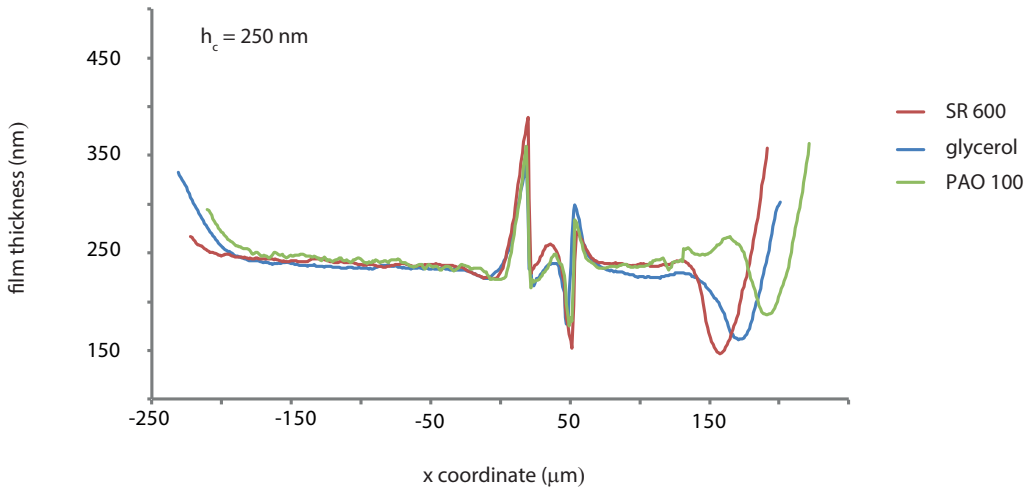

Fig. 6.30 Experimentally measured film thickness values for three different oils: SR600, glycerol and PAO 100 for $h_c = 250$ nm.

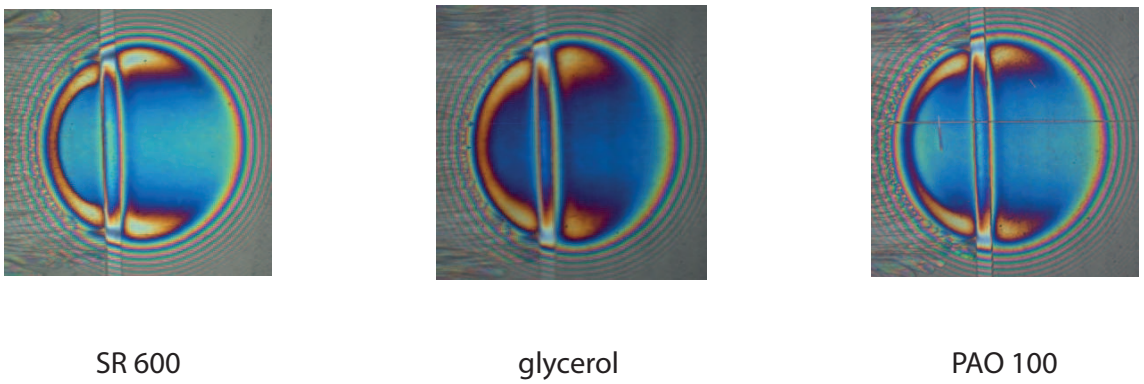

Fig. 6.31 Experimentally measured film thickness values for three different oils: SR600, glycerol and PAO 100 for $h_c = 250$ nm.

Example of experimentally measured film thickness for the three different oils is shown in Figures 6.30-6.31 which show the deformed ridge for central film thickness 250 nm and the interferometry plots. The deformation is the same for all the three different oils.

The film thickness and pressure distributions of the whole contact zone obtained by simulations are shown in Figure 6.32 for the second mean speed, i.e. for the case when the central film thickness is 250 nm. Detail of the deformed shape of the ridge is given in Figure 6.33.

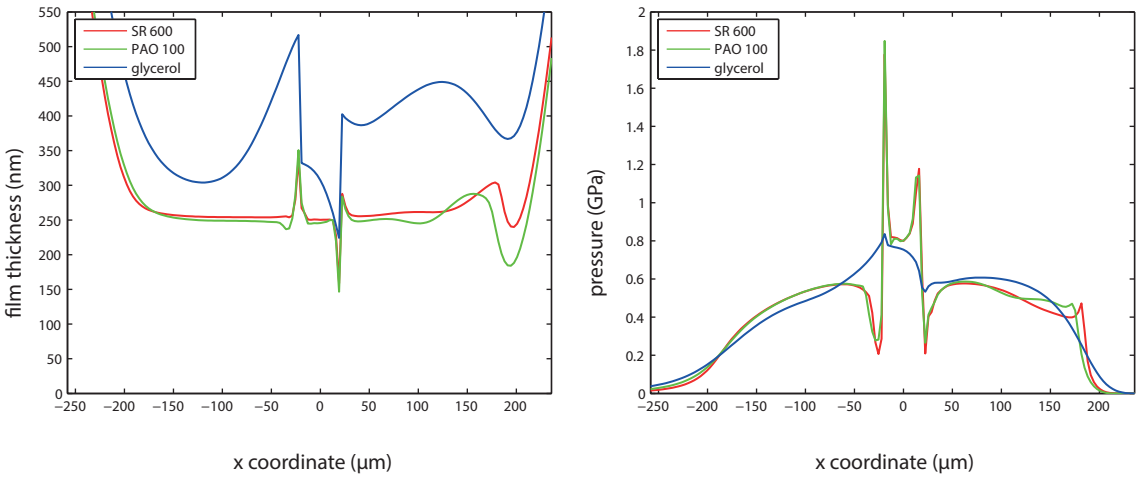

Fig. 6.32 Pressure and film thickness for three different types of lubricants. Mean velocity u_m was set in order to get central smooth film thickness $h_c = 250$ nm.

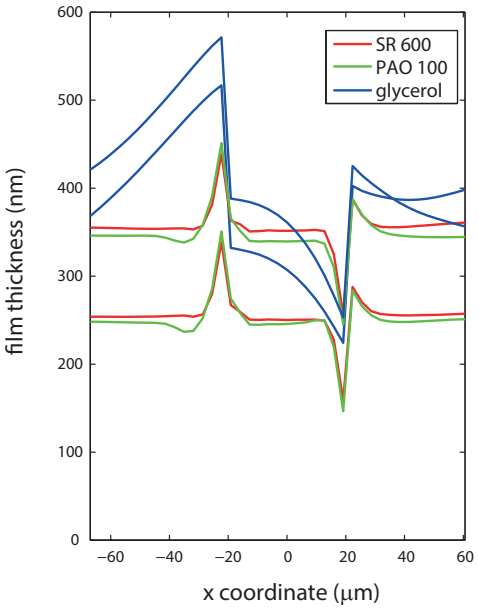

Fig. 6.33 Roughness deformation for three different types of lubricants - for central smooth film thickness values 250 and 350 nm.

The figures reveal some interesting features of the ridge behavior. While the pressure and film thickness distributions are practically the same for the SR 600

and PAO 100 lubricants, the results with glycerol show completely different behavior. Both the pressure and the film thickness distributions deviate. At the trailing edge of the ridge large amount of lubricant is present and a constriction is present underneath the ridge. Consequently, the pressure distribution for glycerol deviates from the other two lubricants as well. The SR 600 and PAO 100 exhibit large gradients around the edges of the ridge while they are absent in the case of the glycerol. The maximum pressure is predicted for the glycerol at the center of the ridge and its value is approximately 0.8 GPa. In the other two cases the maximum pressure values are approximately 1.15 GPa and located around the ridge edges.

Figure 6.33 shows all the deformed ridge profiles for the different mean velocities and the three central film thickness values. The simulation with the PAO 100 oil for 150 nm thickness did not yield a converged solution. Simulations with the SR 600 and PAO 100 lubricants predicted very similar deformed ridge profiles for every value of the mean velocity, however, completely different deformation behavior and magnitude was obtained for the glycerol compared to the other two oils.

By examining the oil parameters, the radically different behavior could be explained by some of the lubricant properties given in Table 6.11. In order to reveal the reason for the differences the effect of the pressure-viscosity parameter α and the Eyring stress τ_0 on the ridge deformation were investigated in next section.

Effect of the pressure-viscosity coefficient α

The effect of the pressure-viscosity coefficient α on the roughness deformation is studied now. A range of different values of α were tested and calculated for a case with $w = 30$ N, $\eta_0 = 0.22$ Pas, mean speed $u_m = 0.08$ m/s, SRR=100% and $\tau_0 = 1$ MPa. The non-Newtonian model was used in the simulations.

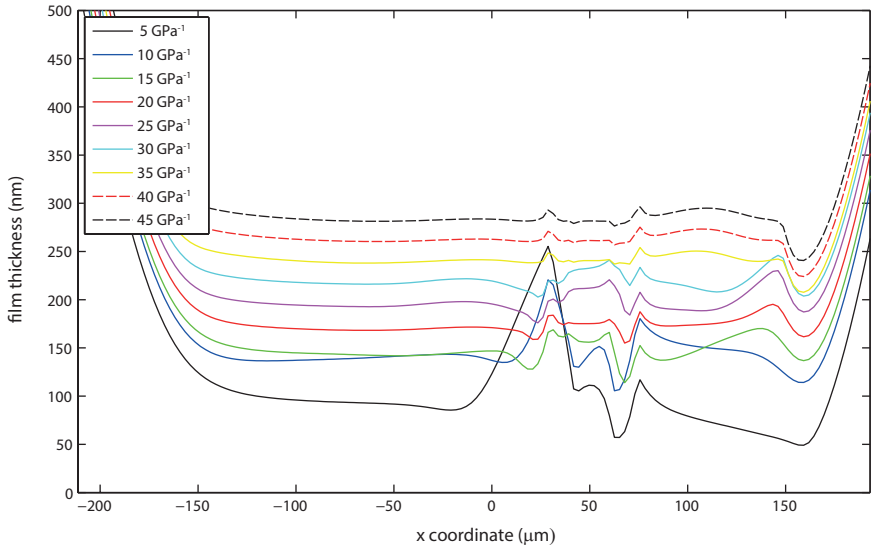

Fig. 6.34 Film thickness for different values of α.

Figures 6.34 and 6.35 show film thickness and pressure distributions, Figure 6.36 enlarges the detail of the deformed ridge. It can be seen in the figures that for low values of α, i.e. 5 and 10 GPa^{-1}, the pressure and film thickness distributions are

very different compared to the distributions of higher α values. The deformation is larger at the trailing edge of the ridge, a backward tilting shape is observed. Increasing the value of α the height of the film reduces compared to the film thickness under the ridge. The pressure gradients at the edges of the ridge are not developed as for higher values, the pressure variations have a forward tilting shape around the ridge which is again lost as α is increased. With increasing α the central film thickness increases as well, on the other hand the pressure spikes around the ridge edges do not increase with increasing α.

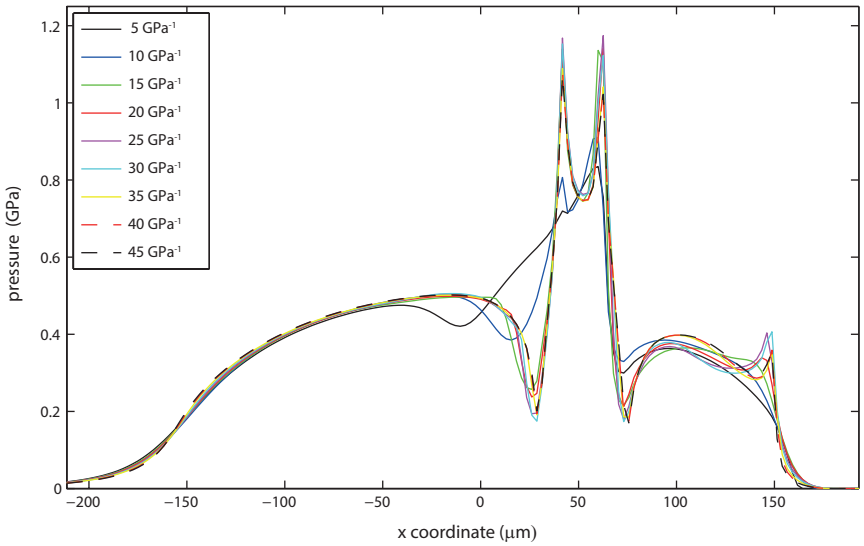

Fig. 6.35 Pressure for different values of α.

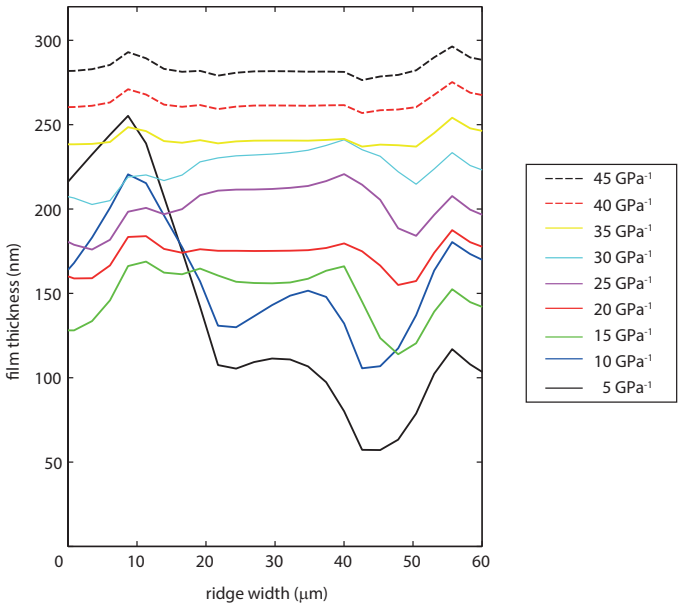

Fig. 6.36 Deformation for different values of α.

Effect of Eyring stress τ_0

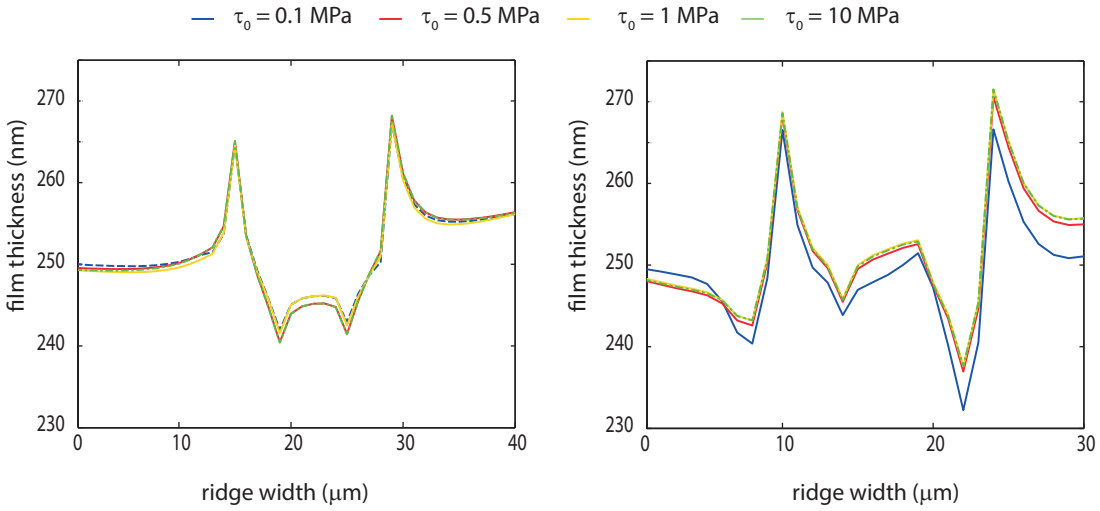

Fig. 6.37 Detail of ridge deformation for a range of τ_0 values for two different lubricants: (a) SR 600, (b) PAO 100.

Figure 6.37 shows deformed ridges for a range of Eyring stresses $\tau_0 = \{0.1,\ 0.5,\ 1,\ 10\}$ MPa. Both SR600 (Figure 6.37a) and PAO 100 (Figure 6.37b) oils were simulated for the same operating conditions as in section 6.2.5 and for such mean velocities so that central film thickness was $h_c = 250$ nm. For both lubricants and all the stress values the deformed ridges show the same behavior. Only for the lowest value of the Eyring stress 0.1 MPa the value of the mean speed had to be increased to get a central film thickness of 250 nm.

Effect of compressibility

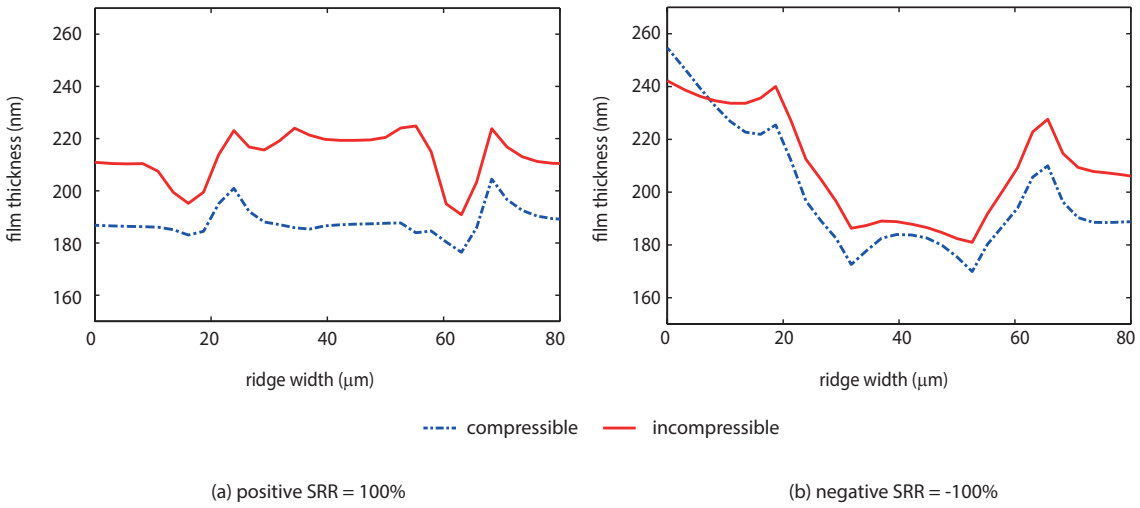

Fig. 6.38 Effect of compressibility - detail of the ridge deformation for $u_m = 0.08$ m/s: (a) SRR $= 100\%$, (b) SRR $= -100\%$.

The effect of the fluid compressibility is shown in Figure 6.38. In Section 6.1 pressure and film thickness distributions were already compared for a stationary smooth contact indicating that the assumption of a compressible fluid decreases the height of the pressure spike and decreases the film thickness. The deformation of the ridge was compared for SRR=100% and 0.08 m/s for a compressible and incompressible fluid. Neglecting the Dowson-Higginson relation (2.21) and assuming the density to be $\bar{\rho} = 1$ in the calculations causes the film thickness to increase. Figures 6.38a and 6.38b show the detail of the ridge.

6.3 Discussion

6.3.1 Accuracy of the solver and limitations of the numerical solution

The accuracy of the numerical solution of any continuous problem depends on many factors such as the choice of the numerical method, the discretization order, etc. The current system of discrete Equations (5.77)-(5.88) is solved by the multilevel techniques which were presented in Section 2.6.3 and described in Section 5.1 and 5.2. The effectiveness of the method was already demonstrated in many works [108]-[111]. The method enables to reduce the number of operations for N discrete points from $\mathcal{O}(N^3)$ to $\mathcal{O}(N \ln N)$ and reduce the calculation speed.

The accuracy of the smooth EHL contact solver, i.e. the stationary case, was already discussed in Section 6.1.3. The time-dependent solver is more complicated due to the presence of the moving surface roughness. The convergence of the iterative method is slower, more relaxation sweeps at each time step are required to achieve the same accuracy as in the stationary case. A second order discretization of the Reynolds equation (5.77) is necessary in order to obtain an accurate approximation.

The solver assumed a pre-defined number of cycles (number of iterations) for each time step. Venner and coworkers [12] showed on a number of simulations that it is sufficient to use this pre-defined amount of iterations to obtain an error below acceptable level. However, the disadvantage of this approach is that the same number of cycles have to be applied to every time step, i.e. regardless of the location of the ridge (whether it is inside or outside the contact). Apparently, the solver needs more cycles when the roughness is inside the contact zone in order to obtain converged solution (the values of the Reynolds equation's residuals smaller than $\mathcal{O}(10^{-4})$), and therefore the pre-defined number of cycles has to respect this aspect. This fact results in longer computing time since the same number of iterations is applied to time steps when the ridge is outside the contact even though in these time steps the number of cycles could be reduced.

An opposite approach was tested in which the order of residuals is defined and the number of cycles at each time steps depends on this value. The solver moves to the next time step after the residuals are reach the pre-defined value (in current case its value was usually defined as $\mathcal{O}(10^{-4})$ or below). The advantage of this approach is that when the roughness is outside the contact zone, the iterative process is very fast, requiring only one F-cycle per time step. However, when the feature is inside the Hertzian contact zone, the solution process can slow down or even oscillate. Due

to this feature of the approach the current model did solve the model problem with the first approach.

The choice of mesh density proved to be significant. It was shown for the smooth contact solver that the difference between the level 5 (257×257) and level 6 (513×513) numerical errors is less than 1% (see the comparison of the friction coefficient in Section 6.1.3). The current solver, however, worked with a surface feature type with sharp edges which caused instability especially at low speeds. Comparison with experiments indicated that for this type of roughness a grid with 257×257 discrete points might not be sufficient with decreasing value of the mean velocity. The lowest mean velocities were simulated with 513×513 grid points. However, a simulation assuming a grid with 513×513 points and for time steps half the value of the spatial step results in very large calculation times equivalent to $\mathcal{O}(10)$ hours in which case the idea of a "fast solver" can be already discarded. The ideal choice of the time step was discussed by e.g. Wijnant [10] or Venner [138] who recommended a time step half the spatial step in the simulations. The current solver respects this fact, and additional simulations with $\Delta T = 0.25\Delta X$ or $\Delta T = \Delta X$ proved their observations.

The solver especially with the current surface feature is very sensitive to the choice of the relaxation factors. The relaxation factors of the Gauss-Seidel and the Jacobi relaxation schemes were chosen in the range from 0.05 to 0.4. The value of the force balance relaxation factor was even lower, it ranged from 0.001 to 0.01. To summarize the accuracy, the current solver is able to gain results with accuracy below $\mathcal{O}(10^{-4})$.

Another source causing instability is the model of the surface feature which affects the relaxation process causing large pressure gradients around its edges or negative film thickness values (i.e. even though the solution converged, the film thickness values were below zero inside the contact zone, this behavior was typical for low mean velocities). Previous works, e.g. [81]-[83], used harmonic functions in the numerical models in order to avoid instability.

The incorporation of the non-Newtonian fluid rheology model into the EHL solver can limit the range of simulations as well. It was pointed out by many authors that an exact derivation and implementation of the rheology function is crucial. For example, the exact calculation of the shear stress with the Eyring sinh law could extremely increase the calculation times due to the additional integrations required to get the stress distributions. The simplified implementation of the non-Newtonian fluid model, e.g. [30] or [43] is very popular in the point contact models but can cause differences between the simulations and experiments. The current work assumed this simplified perturbation approach briefly presented in Section 5.3.

Comparison with previous work

Among others, the aim of the current thesis was to develop an efficient and stable EHL solver. A previously published work at the Institute of Machine and Industrial Design was done by [136] in which full numerical simulations of a smooth EHL point contact and of an over-rolling dent were given. The major differences between the previous and current solver are in the discretization scheme and the fluid rheology model. The previous work assumed Newtonian fluid behavior. Another important difference is in the discretization order of the wedge and squeeze terms of the

Reynolds equation (5.71). These terms were discretized with the first order backward scheme in the previous solver, while the current model uses a combined second order NU2 discretization scheme. Although, the current work presents results with a single transverse flat-top ridge, the model of the surface feature can be replaced in the film thickness calculation routine by any other artificial roughness model (such as a dent, bump, or a waviness). The over-rolling of a dent can be simulated with the solver which is demonstrated in the following figure. The pressure and film thickness distributions at $X_d = 0$ are shown in Figure 6.39 for SRR=100% (the surface with the dent is three times slower than the smooth surface), $u_m = 0.15$ m/s, $w = 50$ N, $E_r = 123.8$ GPa and the properties of SR 600 oil are considered (see Table 6.11). These operating conditions correspond to the following Moes parameters: M=162.12 and L=7.28. The simulation was done with the Newtonian fluid model. The model of the dent is described as in [136], the depth of dent is 0.8 μm, its diameter is 25 μm.

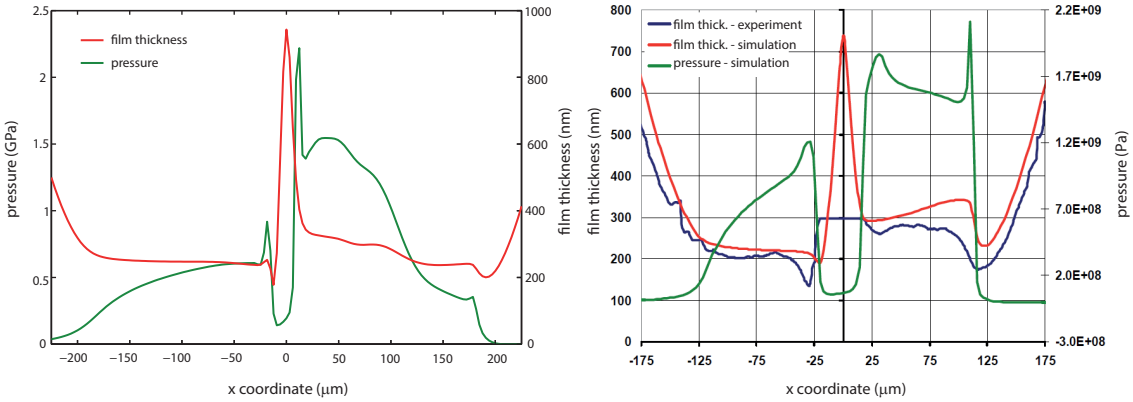

Fig. 6.39 Simulation with a dent - pressure and film thickness distributions at $X_d = 0$, SRR = 100%: (a) results with the current solver, (b) results of Urbanec [136]

The left part of Figure 6.39 demonstrates the pressure and film thickness distributions which exhibit characteristic behavior previously observed by many authors, e.g. [9], [80]. Additional amount of the lubricant is trapped in front of the dent and moves through the contact zone with the mean velocity. The pressure is increased at the edges of the dent, while a larger pressure gradient is present at the leading edge. The geometry of the dent is described by a harmonic function and so for this type of model higher values of relaxation factors (compared to the flat-top ridge) can be applied. On the right of Figure 6.39 solution from [136] is shown. Direct comparison with Urbanec [136] was not possible due to the lack of some of the input data (dent size) for simulation in [136]. Although the operating conditions were different (M=126 and L=21) the pressure and film thickness distributions exhibit similar behavior under SRR=100%, such as the larger pressure gradient around the leading edge of the dent, or the constriction of the film thickness at the trailing edge

of the dent. The presented results (Figure 6.39(a)) indicate that the current solver can handle different types of surface features with sufficient accuracy.

6.3.2 Comparison with other publications

It is possible to check the accuracy of the numerical solver by means of comparison with previously published works. The current model with the flat-top transverse ridge is compared to the results of [99] where an almost identical surface feature was tested. Simulations were carried out for the same operating conditions (see Table 1 in the reference [99]) with the Newtonian model under pure rolling, and with the Eyring model for slide to roll ratios 100% and -100%. Throughout the simulations a grid with 257×257 points was assumed. Figures 6.40-6.42 compare the present model (red solid line) with the results in [99] (black lines).

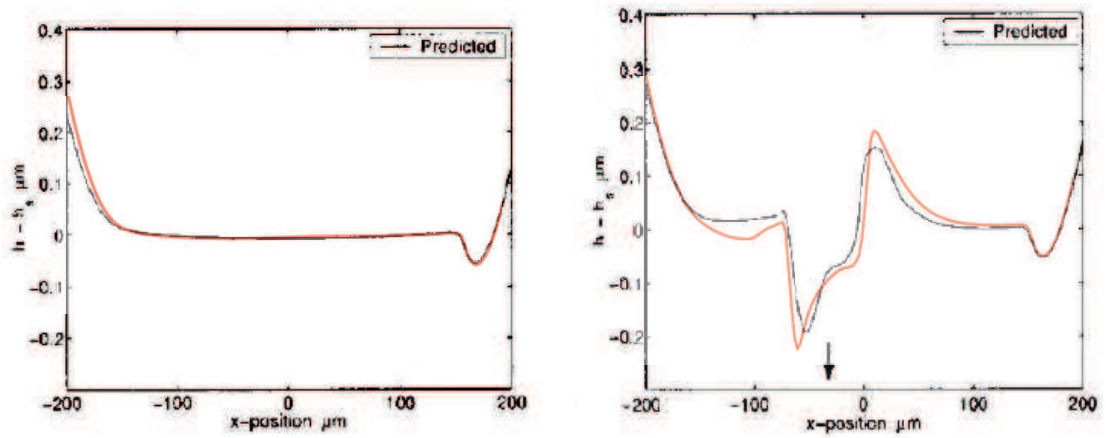

(a) $t = 0$ s (b) $t = 6/500$ s

Fig. 6.40 The deformed ridge profile under pure rolling condition: comparison of film thickness results of the current Newtonian model (red solid line) with results in [99] (black solid line).

Under pure rolling the agreement is excellent - see Figure 6.40. The Newtonian model predicted almost identical ridge deformation. When the rough surface was faster than the smooth surface, i.e. SRR=-100% (Figure 6.41) the current model for the first location (Figure 6.41a) predicted a more heavily deformed ridge profile under the ridge which magnitude was closer to the Newtonian prediction of [99]. The magnitudes of the lubricant entrapment at the leading edge and the constriction at the trailing edge were in agreement with [99]. The second location which was compared (Figure 6.41b) on the other hand underestimated the entrapped lubricant at the leading edge and the overall shape of the deformed ridge is more closely to the Newtonian than the Eyring result of [99].

For the case of positive sliding SRR=100% (Figure 6.42) fair agreement was obtained for the first location (see Figure 6.42a). At the second location (Figure 6.42b) the deformed ridge profile predicted by the current solver looks more like the Newtonian prediction of [99] again.

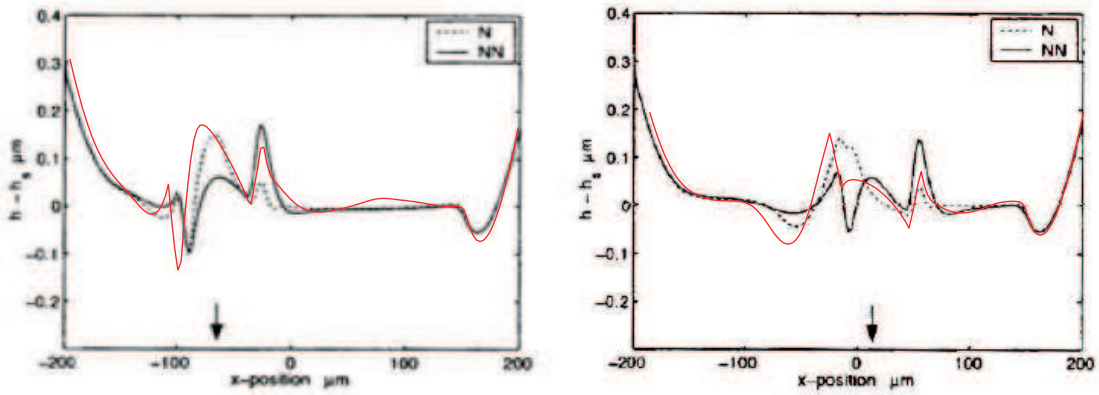

Fig. 6.41 The deformed ridge profile under SRR = −100%: comparison of film thickness results of the current Eyring model (red solid line) with results in [99] (black solid and dashed lines).

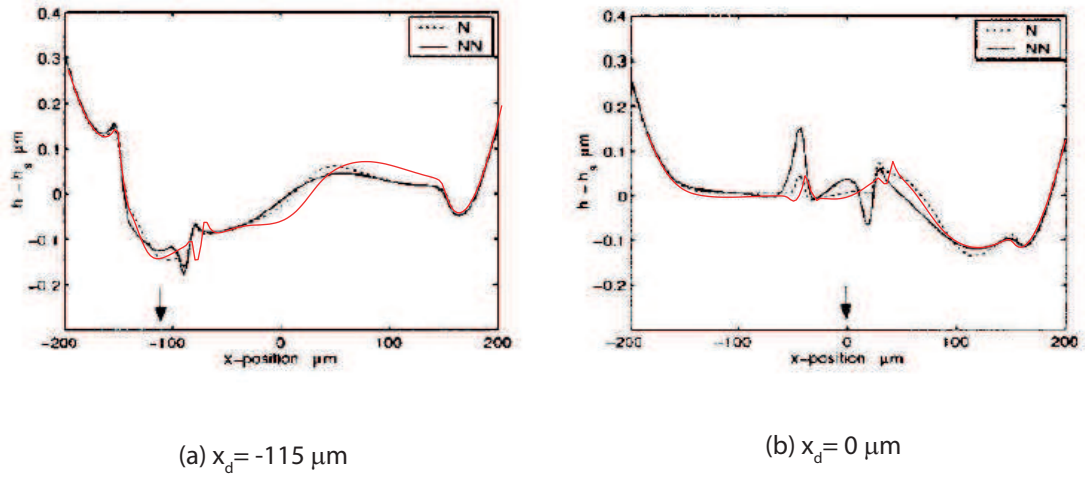

Fig. 6.42 The deformed ridge profile under SRR = 100%: comparison of film thickness results of the current Eyring model (red solid line) with the results in [99] (black solid and dashed lines).

6.3.3 The role of the surface roughness model

Accurate description of the surface roughness is very important in the numerical models. In the majority of theoretical works real roughness shapes are replaced by artificial models which can be described by e.g. harmonic functions. This effort stems from the fact that these models ensure converged solutions for a wide range of operating conditions due to the smooth edges of the roughness.

In Section 2.4 a summary of the different roughness types was given where these types were classified as global or local, or their combination. The current work focuses on a single transverse feature. Previous works dealing with this type of roughness are e.g. [81] where the shape of the transverse ridge was given as

$$R\left(X,Y,T\right)=A\times10^{-10\left(\frac{X-X_d}{W}\right)^2}\cos\left(2\pi\frac{X-X_d}{W}\right) \tag{6.5}$$

where the amplitude A, and the wavelength W of the ridge have to be defined. X_d

denotes the position of the ridge which is given as $X_d = X_0 + u_1 T$ assuming that the surface with ridge moves with velocity u_1. Comparison of this exact type of ridge with experiments showed good agreement, see e.g. [81] and [87]. The largest differences were obtained around the edges of the feature which may be caused by the sharper edges of the experimental ridge or by other factors such as the discretization scheme, fluid rheology or thermal effects.

The current work assumed the model of a transversely orientated ridge with a flat top which approximates the geometry of the ridge used in experiments, see Figure 6.13. Equation (6.5) can not be used to approximate the geometry because the top length of the ridge is non-existent in this model. The following description of the geometry was proposed with H_d the height of the ridge (equivalent to the amplitude) and the base and top lengths of the ridge W_1 and W_2 respectively. The geometry is again expressed depending on the ridge location X_d:

$$R(X,Y,T) = \begin{cases} H_d \frac{X - X_d + \frac{W_1}{2}}{(W_1 - W_2)/2} & \text{if} \quad (X - X_d) < -W_2/2 \\ H_d & \text{if} \quad (X - X_d) < W_2/2 \\ H_d \frac{X_d + \frac{W_2}{2} - X}{(W_1 - W_2)/2} & \text{if} \quad (X - X_d) \leq W_1/2 \\ 0 & \text{otherwise} \end{cases} \tag{6.6}$$

This geometry is implemented in the solver using linear interpolation, similar geometry of the ridge was used e.g. by Felix-Quiñonez [99].

It is clear from the description of the function (see Figure 6.5) that the edges of the ridge are sharp. This can cause instability inside the contact zone and lead to large pressure gradients. Simulations with the current geometry were carried out for a wide range of operating conditions (see Table 6.10), however, for low mean velocities (corresponding to a Moes parameter of load larger than $M > 400$) the calculations converged only with grids with 513×513 nodal points or did not converge at all. In some cases (such as negative SRR) the solver was able to converge for low mean velocities (i.e. 0.01 and 0.02 m/s) with 257x257 grid points using very low relaxation factors but the film thickness dropped below zero resulting in "negative" film thickness values. These difficulties were accounted for the sharp edges of the ridge.

An alternative geometry of the ridge with smoother transition around the edges was designed which could more accurately approximate the ridge used in the experiments from Section 6.2.5. The proposed function in its dimensionless form is the following

$$R(X,Y,T) = H_d \left[\frac{\arctan\left((X - X_d + 0.5W_1)\, S\right)}{\pi} - \frac{\arctan\left((X - X_d - 0.5W_1)\, S\right)}{\pi} \right] \tag{6.7}$$

where H_d is the height of the ridge, W_1 the base width and parameter S defining the smoothness at the edges of the ridge. The choice of the value of S in the simulations was arbitrary. With increasing value of S the shape of the ridge model described by Equation (6.7) approaches the geometry of the flat-top ridge.

The effect of the ridge geometry on the deformation and the pressure distribution is investigated in the following. Five different geometries were chosen: one with the

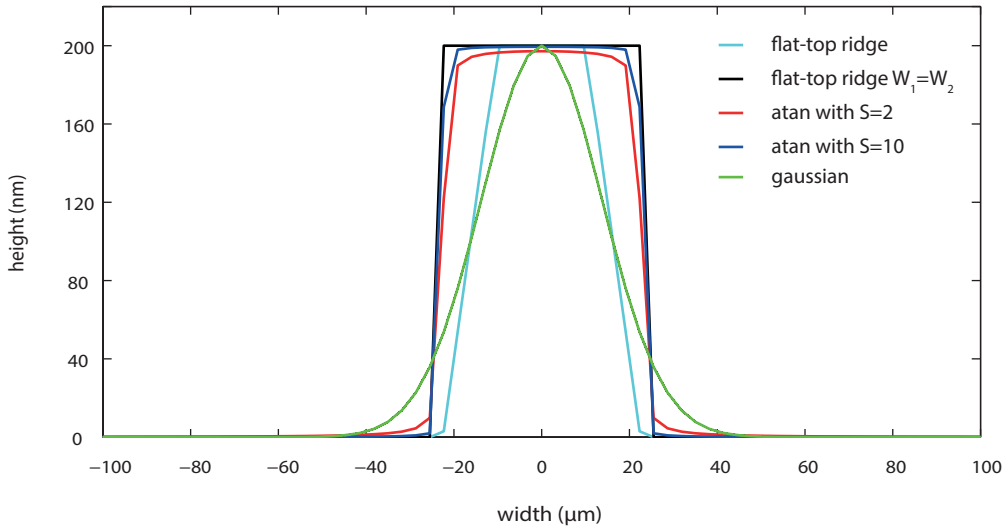

Fig. 6.43 Comparison of ridge geometries - the flat-top ridge used in the simulations with $W_1 \neq W_2$ and $W_1 = W_2$, the ridge defined by (6.7) with $S = 2$ and $S = 10$ and the Gaussian ridge.

flat-top profile with different base and top widths, another flat-top geometry with equal base and top widths $W_1 = W_2$, two cases defined by Equation (6.7) with $S = 2$ and $S = 10$ and a ridge described by the Gaussian function see e.g. [85]. Figure 6.43 compares the geometries of the five different cases.

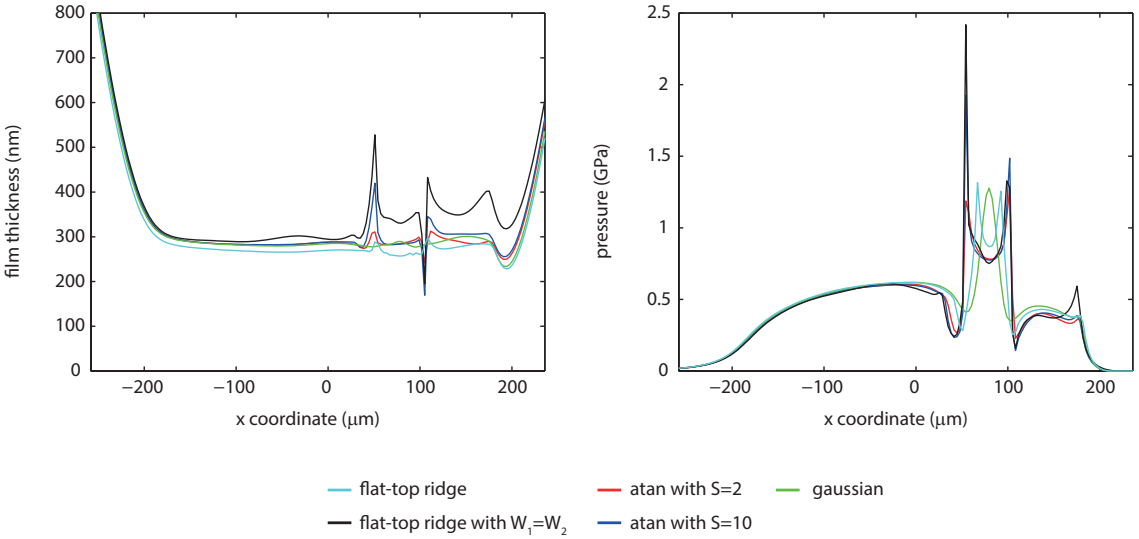

Fig. 6.44 Film thickness (left) and pressure (right) distributions for five different ridge geometries.

Film thickness and pressure distributions were calculated for the proposed geometries and can be seen in Figure 6.44. The operating conditions were the following: $u_m = 0.08$ m/s, $p_h = 0.566$ GPa, $SRR = 100\%$ and parameters of SR 600 oil (Table 6.10). Detail of the deformed ridge profiles is shown in Figure 6.45.

Results indicate that the choice of W_1 and W_2 in the flat-top ridge geometry (6.6), as well as the choice of the parameter S in the arctan model (6.7) have major influence on the pressure distribution and the deformation of the ridge. When the base and top widths of the flat-top ridge are equal the ridge is more deformed than

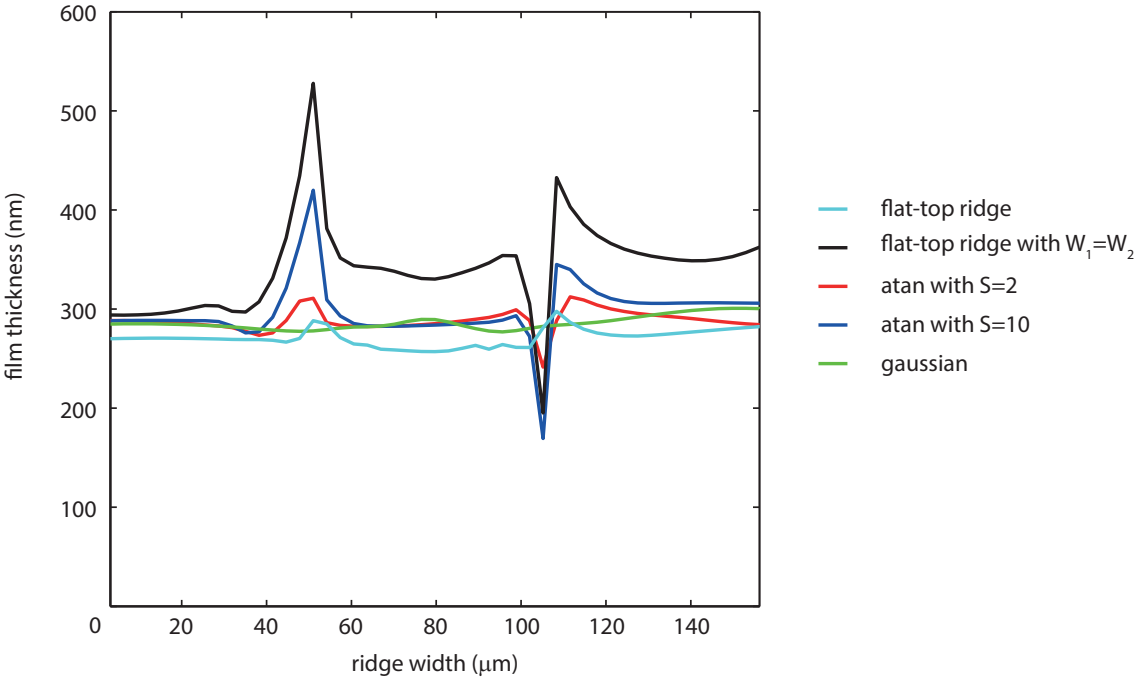

Fig. 6.45 Detail of the deformed ridge for five different geometries: flat-top ridge with $W_1 \neq W_2$ and $W_1 = W_2$ (Eqn.(6.6)), atan ridge with $S = 2$ and $S = 10$(Eqn.(6.7)) and Gaussian ridge.

with a shorter top width. The shape of the deformation is not symmetric around the edges of the ridge. At the leading edge a constriction is visible while at the trailing edge much larger deformation is predicted resulting in a peak. Even more visible differences can be seen in the pressure distributions. When the flat-top ridge has a step-like shape the pressure spike at the trailing edge is two times higher than the spike at the flat-top ridge with shorter top width. Comparing the ridges modeled by the arctan function it can be seen that with increasing S the shape of the deformed ridge changes. Magnitudes of the peak at the trailing edge and the constriction at the leading edge increase with increasing S. On the other hand, the pressure distributions are in closer agreement for the two values S. For $S = 10$ the pressure spikes around the edges of the ridge are only slightly higher. The Gaussian description of the ridge proved to be inaccurate to approximate the experimental flat-top ridge and the predicted distribution is closer to a distribution predicted by a bump (see e.g. [9]) than a ridge. The differences are more distinct for the pressure where its shape approaches the pressure distribution predicted again by a bump [9], [85]. Detailed comparisons of the undeformed and deformed profiles of the ridges are given in Figure 6.46. When the ridge used in the experiments has a step-like geometry with equal base and top widths the numerical model described by the arc tan function serves as a more advantageous option. The edges of the ridge are more smooth yielding better convergence of the residuals and ensuring higher stability of the numerical solution than the flat-top model with equal base and top widths. Furthermore, the arctan model predicts more moderate pressure spikes around the edges of the ridges. It should be noted that the choice of the parameter S in Equation (6.7) was arbitrary (S=2 and S=10) and therefore further work should be done in order to determine the method of choosing parameter S.

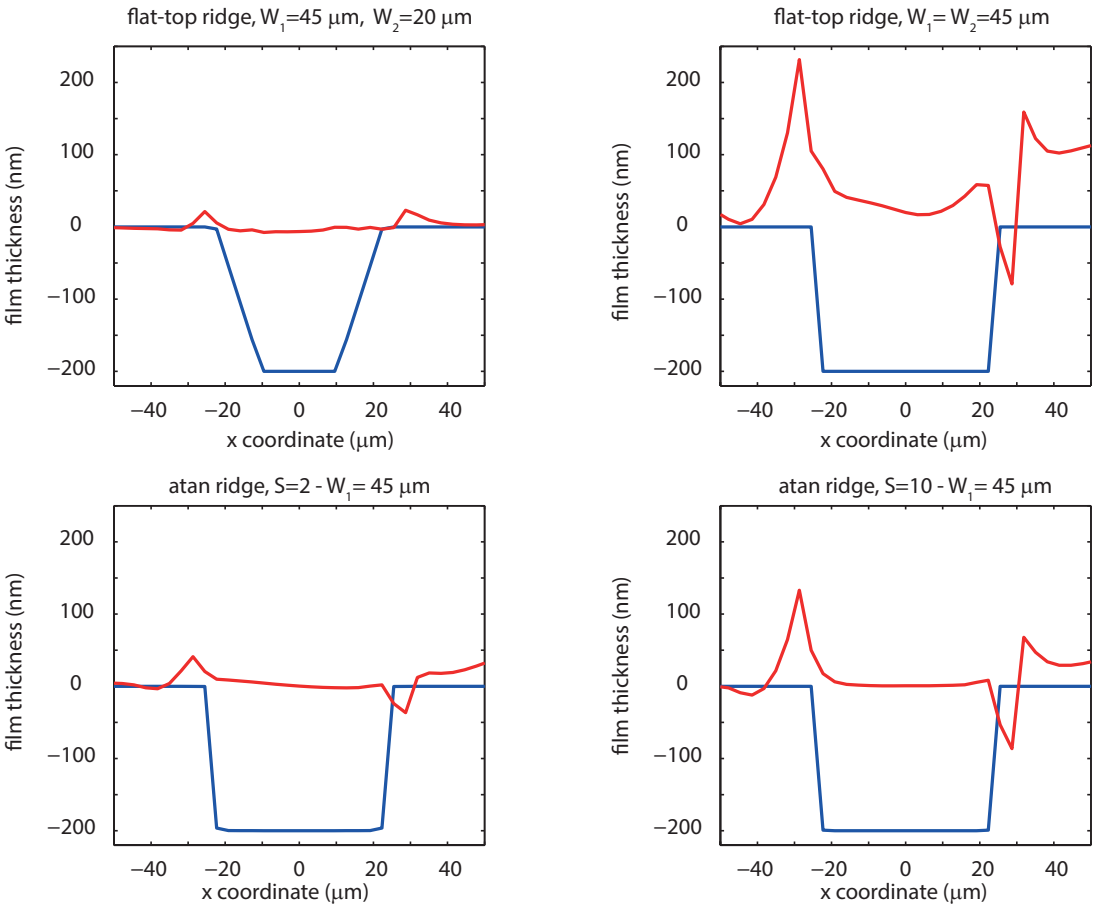

Fig. 6.46 Detail of the undeformed (blue line) and deformed (red line) ridge geometry for four different models of geometry.

In [99] an almost identical flat-top ridge (with different values of the height and widths) was studied. The authors compared the effect of the geometry on the deformation. Figure 6.47 compares the original ridge with the modified ones: one with half of the original height, one with double of the original base width and a Gaussian shaped ridge used by Greenwood [85]. The different shapes were compared under pure rolling and rolling-sliding conditions.

Under pure rolling (on the left in Figure 6.47) a forward-tilting shape is characteristic for the ridge. This shape was demonstrated with the current model too, see e.g. Figure 6.13. The deformed shape of the ridge consists of a locally enhanced region of film thickness in front of the ridge and a constriction appearing underneath the ridge at its inlet side [99]. Felix-Quiñonez concluded that the flat-top geometry of the ridge is responsible for this constriction. With the Gaussian ridge the constriction affects directly the height of the entrapped lubricant which is smaller in that case. When the length of the base width is doubled a wider flat region underneath the ridge is developed. A larger base width, however, does not affect the height of the entrapped lubricant in front of the ridge. With decreasing ridge height the amplitude of the film variations reduces as well.

Under rolling-sliding the lubricant entrapment has the greatest impact on the deformation. The deformations were larger for a faster moving rough surface (positive SRR in [99]), see the middle of Figure 6.47. This is because the faster moving

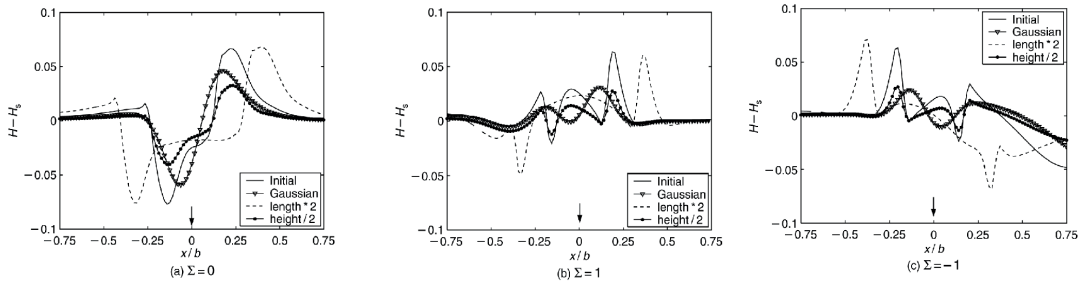

Fig. 6.47 Effect of the ridge geometry on film thickness in the high pressure zone studied in [99].

ridge has to undergo larger deformation to overcome the extra amount of entrapped lubricant when passing through the inlet [99]. When the rough surface is slower (negative SRR) the deformation is lower since the ridge undergoes flattening when it is located comparatively deeper inside the contact [99], see the right part of Figure 6.47.

6.3.4 The role of the non-Newtonian fluid model and lubricant properties

The use of the non-Newtonian fluid model in the numerical simulations was justified by several works in the last decades (e.g. [26], [29], [32], [33] or [42]). The calculation of traction curves under sliding conditions failed to explain the experimentally measured non-linear shapes with the Newtonian model [30]. This fact proved the need of a different rheology model than the Newtonian which would assume the non-linear dependence between the shear rate and shear stress. On the other hand, the Newtonian model works well under the assumption of smooth surfaces [100].

Under rolling-sliding conditions the differences between the Newtonian and non-Newtonian models are noticeable. Examples of full numerical simulations with both models are given e.g. by [99] where the passage of a single roughness feature through the contact was studied. In the work the agreement between the experiments and numerics was better with the non-Newtonian model. Major difference between the two models appeared in the deformed shape of the ridge. Specifically, when the rough surface moved faster the ridge was able to overtake the slower moving lubricant with the Newtonian model at a point closer to the inlet causing a relatively more deformed ridge than in the experiments [99]. For opposite slide to roll ratio the Newtonian model was unable to reproduce the locally enhanced region of lubricant behind the ridge [99]. The Poiseuille terms of the Reynolds equation were believed to be responsible for the differences in the two models. While for the Newtonian model these terms are small and the Reynolds equation is reduced to the transport equation, the non-Newtonian model prevents these terms from disappearing. Felix-Quiñonez [99] observed that the ridge is deformed for the non-Newtonian model gradually as it passed through the contact. It was shown by simulations that with increasing value of τ_0 the non-Newtonian behavior approaches the Newtonian one. The authors conclude that the dominating contributing factor to the good agreement between the experiments and numerical simulations is the reduction of the local effective viscosity given by the non-Newtonian behavior of the lubricant.

The Newtonian lubricant yields a more deformed ridge, while the reduced viscosities of the non-Newtonian results might explain the local entrapment of lubricant in front of or behind the ridge (depending on the SRR) [99]. Another examples of full simulations with a non-Newtonian model were given in Section 2.5.

Results in Section 6.2.5 compared the different properties of the lubricants and their effect on the ridge deformation. Experimental results showed that independently of the values of these properties (α, η_0 and τ_0) practically the same deformation is obtained for given operating conditions (i.e. Hertzian pressure p_H, mean velocity u_m and SRR). Simulations, however, showed different behavior for glycerol. The other two oils confirmed the experimental results, although differences between the magnitude of the deformation around the edges can be seen. Figure 6.37 showed that the value of the Eyring stress τ_0 does not have a significant influence on the deformation or the pressure distribution. Previous studies indicated that with increasing τ_0 the conditions inside the contact approach the distributions predicted by Newtonian model [93]. On the other hand, results with different values of α indicate that its value has a significant effect on the pressure and film thickness distributions.

Effect of the pressure-viscosity coefficient α

The differences in the pressure and film thickness distributions for different values of α can be traced back to the use of the pressure-viscosity relation (2.20), the effective viscosties (5.66) and the Poisseuile terms in the Reynolds equation (5.54) in combination with the relaxation schemes applied in the numerical solution.

The pressure-viscosity coefficient α is present in the Roelands relation which influences the value of $\xi_{i,j}$ (5.79) in the pressure terms of Reynolds equation. The value of ξ determines which relaxation scheme is to be applied. Venner and Lubrecht [12] showed for a Newtonian lubricant that inside the contact zone where the viscosities are high the pressure terms are almost negligible and the Reynolds equation reduces to the so called transport equation. After the values of ξ reach a certain limiting value the conditions inside the contact require to use a more stable relaxation scheme, in this case the Jacobi distributive line relaxation. It was shown in [12] that for the majority of contact problems this limiting value (switch parameter) should be 0.3. The same criterion was used by Jacod [30] or Chapkov [46] in their works with the Eyring model and for surface roughness models. In Section 6.2.5 the same criterion was applied for all simulations. It has to be noted that for a non-Newtonian lubricant the values of the viscosities are not as high as in the Newtonian case, and the pressure terms might not disappear from the Reynolds equation. Figures 6.34 and 6.35 showed that for the lowest values of α the pressure did not develop into high gradients around the edges of the ridge, and the shape of the ridge deformation was unexpected with larger values.

Analysis of the values of ξ is necessary in order to verify the criterion for the switch between the relaxation schemes. Two conditions in the numerical solution have to be checked:

- the value of the so-called switch criterion ξ_{lim} which determines the type of relaxation scheme to be applied (the Gauss-Seidel line relaxation for low pressures and the Jacobi distributive line relaxation for the high pressure area)

- the range of $\xi_{x,i\pm1/2,j}$ and $\xi_{y,i,j\pm1/2}$ in the pressure terms of the Reynolds equation which' values are to be compared with the switch criterion.

For low α the viscosity η predicted by the Roelands relation for a pressure lets say in the middle of the contact (e.g. the Hertzian pressure can be assumed) results in higher values of $\xi_{x,y}$ inside the contact and did not drop below 0.3. This causes that only the less stable Gauss-Seidel relaxation scheme (5.89)-(5.92) is used in the high pressure area resulting in the presented pressure and film thickness distributions 6.34-6.36. The values of ξ are higher for a lower α and this indicates that the switch value of ξ_{lim} should be increased. Simulations showed that the exact value of the parameter depends on the operating conditions in the contact and should be determined independently for each case.

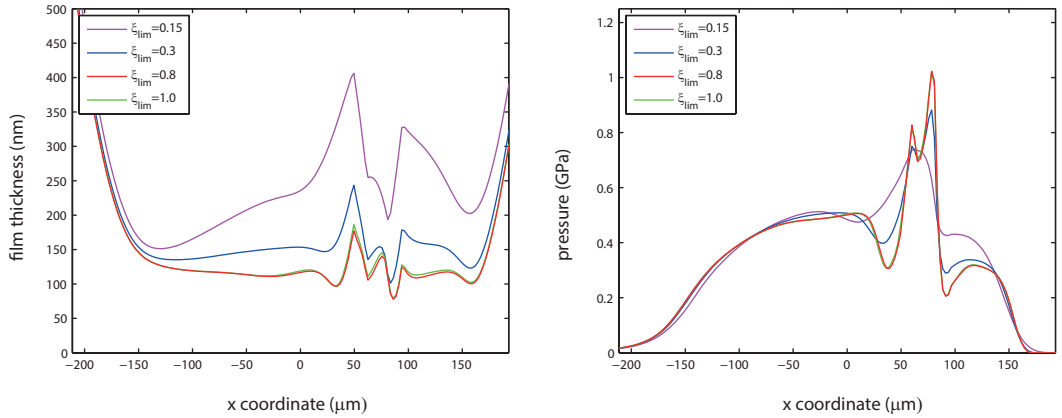

Fig. 6.48 Film thickness (left) and pressure (right) distributions for α=10 GPa^{-1}, SRR=100%, w=30N, u_m=0.8m/s and for different values of ξ_{lim}=0.15, 0.3, 0.8, 1.0.

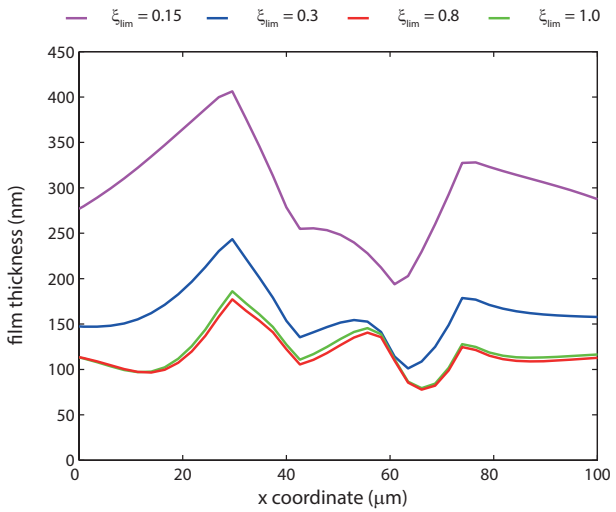

Fig. 6.49 Detail of the deformed ridge for α=10 GPa^{-1}, SRR=100%, w=30N, u_m=0.8m/s and for different values of ξ_{lim}=0.15, 0.3, 0.8, 1.0.

Figures 6.48-6.49 show comparisons of the same operating conditions for $\alpha = 10$ GPa^{-1} as in Section 6.2.5 but with different values of the criterion ξ_{lim}. The genuine value from Section 6.2.5 is 0.3, the higher values which were tested were 0.8 and

1.0, and for comparison results with 0.15 are displayed too. The results show that the higher the value of ξ_{lim} the better agreement with the higher α values (e.g. $\alpha = 15$ or 20 GPa^{-1}) results can be obtained. The same conclusion can be drawn for the pressure values which show that increasing the limit criterion improves the ability of the pressure to generate the pressure gradients around the edges of the roughness. Testing a range of criterion values ξ_{lim} for $\alpha = 5$ GPa^{-1} did not yield similar results. The chosen range of ξ_{lim} did not improve the results as in the case of $\alpha = 10$ GPa^{-1}.

The second condition which has to be checked is the range of $\xi_{x,y}$ values which are to be compared with ξ_{lim}. In [12] the following condition was defined for the EHL problem: the Gauss-Seidel line relaxation is used when

$$|\xi_{i,j+1}|, |\xi_{i,j-1}|, |\xi_{i+1,j}|, |\xi_{i-1,j}| > \xi_{lim} \tag{6.8}$$

Otherwise, the Jacobi distributive line relaxation is applied. The above mentioned formula was used for the smooth contact problems. Jacod [30] used similar criterion for the stationary rough contact problem with both non-Newtonian Eyring and the limiting shear stress models (holding for the Gauss-Seidel line relaxation)

$$\min(\xi_x, \xi_y) > \xi_{lim} \tag{6.9}$$

Chapkov [46] solving the transient EHL problem modified the condition for the Gauss-Seidel line relaxation to

$$|\xi_{i,j+1}|, |\xi_{i,j-1}| > \xi_{lim} \tag{6.10}$$

Chapkov explained this change by the anistropic character of the Poiseuille terms for which holds that $|\xi_x| < |\xi_y|$. In some cases $|\xi_x| << |\xi_y|$ causing instability inside the contact zone and therefore the change in the switch criterion is necessary. The current solver assumed criterion (6.10) which yielded convergent solutions, unlike criteria (6.8)-(6.9).

6.3.5 Summary of results

The most important results of Section 6.2 are highlighted now.

Differences between pure rolling and rolling-sliding conditions

- Under pure rolling conditions the Newtonian and non-Newtonian models yielded almost identical pressure and film thickness distributions for the surface roughness model.
- Under rolling-sliding conditions the ridge is deformed more heavily. The ridge almost flattened out for positive SRR, for negative SRR the deformation was smaller. The solution is the combination of a moving steady solution and a complementary function as observed before by many authors ([9], [80] or [85], etc.). The larger the SRR the higher separation of the two components occurs.
- In the case of rolling-sliding the fluid rheology function does play an important role, e.g. the Newtonian model predicts larger pressure variations around the ridge.

Effect of the operating conditions

The effect of the mean velocity u_m and SRR on the roughness deformation was studied for a range of operating conditions (see Table 6.10) with the Eyring model. The results revealed the following:

- the deformed shape of the ridge does not vary significantly with varying values of the mean velocity.
- For a given value of the SRR the magnitude of the deformation and the shape of the deformed ridge does not vary notably with increasing or decreasing mean velocity.
- For positive SRR the results were in agreement for high values of SRR (100% and 150%) while small deviations can be seen for SRR=70% for which a constriction around the leading edge of the ridge is present. Similar trend can be observed for negative SRRs. Under the ridge the deformation of the ridge varies with the SRR. Differences can be seen in the height of the film thickness at the trailing edge while at the leading edge the height of the film thickness is approximately the same.
- Comparing the results of the two rheology models it can be observed that for positive SRR the predicted ridge profiles are very similar but the Newtonian model predicts lower values of film thickness for a given mean speed. The situation is different for negative SRR in which case an increased amount of film thickness (bump) can be observed under the ridge.
- Comparison with the experimentally measured film thickness values showed differences compared to the calculations, better agreement was found primarily with simulations with the lowest mean velocities.
- The comparison was closer to measurements for negative values of SRR (i.e. when the surface with the ridge was faster). With increasing mean speeds the agreement decreased.
- When the ridge was slower the numerical model did not give a converged solution for the lowest speeds, this problem could not be overcome even with more grid points.

Newtonian versus non-Newtonian models

- Under pure rolling the Newtonian model can be used for both smooth contact problems and for roughness simulations. Both rheology models predicted for the roughness model same magnitude of ridge deformation.
- When the velocities of the contacting surfaces differ and sliding is present it is necessary to assume non-Newtonian lubricant behavior.

Effect of the surface roughness geometry

- The geometry model of the ridge influences mostly the areas around the edges of the ridge, i.e. the amount of the entrapped lubricant right before or behind the ridge (depending on the sign of SRR) and the microconstriction of film thickness.

- A new geometry described by an arctan function was tested. A parameter responsible for the smoothness of this function was chosen arbitrary. More analysis should be done in order to choose this parameter properly.
- When the base and top widths of the flat-top ridge equal, the pressure gradients around the edges are an order of magnitude higher than with a smaller top width. The ridge deforms more heavily as well.

Effect of the non-Newtonian lubricant properties

- Three oils with different lubricant properties (α, η_0, τ_0) were compared. The results revealed some interesting features, the deformation of the ridge was the same for two lubricants (SR 600 and PAO 100), but very different for glycerol. The deformed shape of the ridge did not vary for any of the oils with varying mean velocity.
- The large difference in the behavior of the ridge with glycerol could be caused by the low value of the pressure viscosity coefficient α and the effects it causes in the numerical solution. The value of α used in the Roelands relation among others influences the values of $\xi_{x,y}$ which determine (based on some pre-defined criterion ξ_{lim}) which relaxation scheme is used in the numerical solution. Analysis of the viscosity values and pressure terms of the Reynolds equation in Section 6.3.4 imply that the complexity of the non-Newtonian model may require to expand the grid points where the Jacobi relaxation scheme is used. Therefore, the values of $\xi_{i,j}$ in the pressure terms of the Reynolds equation for low α indicate that the switch criterion ξ_{lim} should be increased. The exact value of the criterion may vary with the value of α and operating conditions.
- Experiments showed the same behavior for the glycerol confirming that the differences found in the numerical simulations can be accounted for the relations used in the mathematical model or implementation details of the numerical solver.
- With varying value of the Eyring shear stress no difference was observed in the ridge deformation for any of the tested oils (SR 600 or PAO 100).
- Studying the effect of lubricant compressibility revealed similar features as in the case of a smooth EHL contact, the assumption of an incompressible fluid increases the film thickness but does not effect significantly the deformation magnitude.
- It has to be emphasized that more work has to be done in order to improve the accuracy of the solver. More precise model of the roughness feature might remove the limitations and gain on the accuracy of the solution. The implementation of the non-Newtonian fluid model has to be improved as well. The current rheology model might be replaced by a different rheology approach, however, detailed analysis and derivation of the two-dimensional rheology functions is necessary in order to design a model which can give solutions in acceptable computing times.

7 CONCLUSIONS

The current dissertation presents results of numerical simulations of a single flat-top transverse ridge under rolling-sliding conditions assuming non-Newtonian lubricant model. Modern numerical techniques enable to solve a wide range of lubrication problems such as the passage of different surface features through the contact zone. The aim of the numerical models is to serve as a stable tool in order to predict the EHL parameters or to be able to compare it with experiments.

The current work contains summary of the literature review in the area of numerical simulations of different artificial surface roughness models (e.g. ridges, waviness or dents). The importance of fluid rheology is pointed out and different rheology models are described. The mathematical model describing the EHL point contact model is presented too. A detailed description of the numerical method applied in the current solution is given. The discrete equations and implementation details of the current numerical model are presented as well. The second half of the dissertation presents results obtained for the stationary and time-dependent solver for a wide range of operating conditions.

The main goal of the dissertation was to study the deformation of a roughness feature and the effect of different operating conditions and lubricant parameters on the magnitude of this deformation. The results obtained by numerical calculations were compared to experimentally measured film thickness values. Partial aim of the work was to develop a stable and fast numerical solver able to predict film thickness and pressure distributions for a wide range of operating conditions. The accuracy of the solver was compared to previously published works and solvers. The results presented in the work can form the basis for further studies and comparisons with experiments.

The dissertation contains original work and results observing the behavior of an artificial roughness feature inside the contact zone. Direct comparison with experiments was given which presented the behavior of the roughness feature under a range of operating conditions (mean velocities and slide to roll ratios). The effect of these operating conditions on the deformed ridge profile was studied. Furthermore, results of numerical simulations for different oils are given in the thesis. The effect of the non-Newtonian parameters, such as the Eyring stress, pressure-viscosity coefficient or the ambient viscosity, on the deformation behavior was observed. These simulations were compared to experimentally evaluated film thickness where the results indicated the importance of different modeling aspects: the geometry of the roughness feature in the mathematical model or the optimization of numerical parameters in the numerical model.

REFERENCES

[1] STACHOWIAK G., BATCHELOR A.: *Engineering Tribology.* 3rd Edition, 2005, ISBN 978-0750678360.

[2] REYNOLDS, O.: On the Theory of Lubrication and its Application to Mr. Beauchamp Tower's Experiments, including an Experimental Determination of the Viscosity of Olive Oil. *Philosophical Transactions of the Royal Society of London*, 1886, p. 157-234.

[3] TOWER, B.: First report on friction experiments (friction of lubricated bearings). *Proc. Instn mech. Engrs*, Nov. 1883, p. 632-659.

[4] MARTIN, H.M.: Lubrication of Gear Teeth. *Engineering*, 1916, 102, p. 119-121.

[5] GÜMBEL, L.: Über Geschmierte Arbeitsräder. *Z. ges. Turbinenwesen*, 1916, 13, p. 357.

[6] GRUBIN, A.N.: Fundementals of the hydrodynamic theory of lubrication of heavily loaded cylindrical surfaces. *Central Scientific Research Institute for Technology and Mechanical Engineering*, 1949, Book no 30, Moscow, D.S.I.R. transactions, p. 115-166.

[7] PETRUSEVICH, A.I.: Fundamental conclusions from the contact hydrodynamic theory of lubrication. *Izv. Alad. Nauk SSR (OTN)*, 1951, 3, p. 209-223.

[8] GOHAR, R.: *Elastohydrodymanics.* 2nd Ed., World Scientific Publishing Company, 2002, p. 446, ISBN 978-1860941702.

[9] VENNER, C. H.: *Multilevel solution of the EHL line and point contact problems.* Ph.D. Thesis, University Enschede, The Netherlands, 1991.

[10] WIJNANT, Y.H. : *Contact Dynamics in the field of Elastohydrodynamic Lubrication.* Ph.D. Thesis, University Enschede, The Netherlands, 1998.

[11] HERTZ, H.: Über die Berührung Fester Elasticher Körper. *J. reine und angew. Math*, 1881,92, p. 156-171.

[12] VENNER, C.H., LUBRECHT, A.A. *Multilevel Methods in Lubrication.* Amsterdam, Elsevier Science B.V., 2000.

[13] BARUS, C.: Isothermals, Isopiestics and Isometrics relative to Viscosity. *Am. J. of Science*, 1893, 45, p. 87-96.

[14] ROELANDS, C.J.A.: *Correlational Aspects of the Viscosity-Temperature-Pressure Relationship of Lubricating Oils.* Ph.D. Thesis, Technical University Delft, Delft, The Netherlands, 1966.

[15] HABCHI, W. : *A Full-System Finite Element Approach to Elastohydrodynamic Lubrication Problems: Application to Ultra-Low-Viscosity Fluids.* Ph.D. Thesis, LaMCoS, INSA Lyon, France, 2008.

[16] FERRY, J. D.: *Viscoelastic Properties of Polymers.* John Wiley & Sons Inc., New York, 1961.

[17] YASUTOMI, S., BAIR, S., WINER, W.O.: An Application of a Free-Volume Model to Lubricant Rheology, (1) Dependence of Viscosity on Temperature and Pressure. *ASME J. of Tribology*, 1984, vol. 106, p. 291–312.

[18] DOOLITTLE, A. K.: Studies in Newtonian Flow II, The Dependence ofthe Viscosity of Liquids on Free-Space. *J. Appl. Phys.*, 1951, vol. 22, p. 1471–1475.

[19] DOWSON, D., HIGGINSON, G.R.: Elastohydrodynamic Lubrication, The Fundamentals of Roller and Gear Lubrication. *Pergamon Press*, Oxford, Great Britain, 1966.

[20] HIRSCHFELDER, J. O., CURTISS, C. F., BIRD, R. B.: *Molecular Theory of Gases and Liquids*, Wiley, New York, 1954.

[21] HOOGENBOOM, D. L., WEBB, W., DIXON, J. D.: Viscosity of Several Liquid Hydrocarbons as a Function of Temperature, Pressure and Free Volume. *J. Chem. Phys.*, 1967, vol. 46, no. 7, p. 2586–2598.

[22] LEE, R.T.: *Transient and rheological effects in elastohydrodynamic and microelastohydrodynamic lubrication.* Ph.D. Thesis, The Ohio State University, USA, 1989.

[23] JOHNSON, K.L., TEVAARWERK, J.L.: Shear behaviour of elastohydrodynamic oil films. *Proc. Roy. Soc. London*, 1977, series A, vol. 356(12), p. 215-236.

[24] MAXWELL, J.: *A treatise on electricity and magnetism.* Clarendon Press, 1873.

[25] EYRING, H.: Viscosity, Plasticity and Diffusion as Examples of Absolute Reaction Rates. *The Journal of chemical physics*, 1936, vol. 4, p. 283-291.

[26] KHONSARI, M.M., HUA, D.Y.: Generalized non-Newtonian elastohydrodynamic lubrication. *Tribology International*, 1993, p. 405-411.

[27] SLOETJES, J.W.: *Micro-elastohydrodynamic lubrication in concentrated sliding contacts.* Ph.D. Thesis, University of Twente, Enschede, The Netherlands, 2006. ISBN 90-365-2419-9.

[28] EVANS, C.R., JOHNSON, K.L.: The rheological properties of elastohydrodynamic lubricants. *Proc. Instn. Mech. Engrs.*, 1986, vol. 200, no. C5, p. 303-312.

[29] BAIR, S., WINER, W.O.:A rheological model for elastohydrodynamic contacts based on primary laboratory data. *Trans. ASME, J. Lubr. Tech.*, 1979, vol. 101, p. 258-265.

[30] JACOD, B.: *Friction in elasto-hydrodynamic lubrication.* Ph.D. Thesis, Universtiy of Twente, The Netherlands, 2002. ISBN: 90-365-1782-6.

[31] GECIM, B., WINER, W.O.: Lubricant limiting shear stress effect on EHD film thickness. *Trans. ASME, J. Lubr. Tech.*, 1980, vol. 102, 213-220.

[32] WANG, H., HUA, D.Y., ZHANG, H.H.: A full numerical EHL solution for the line contacts under pure rolling conditions with a non-Newtonian rheological model. *Trans. ASME, Journal of Tribology*, 1988, vol. 114, p. 583-586.

[33] LEE, R.T., HAMROCK, B.J.: A circular non-Newtonian model: Part 1 - used in elasto-hydrodynamic lubrication. *Trans. ASME - Journal of Tribology*, 1990, vol. 112, p. 486-495.

[34] ELSHARKAWY, A., HAMROCK, B.J.: Subsurface stresses in micro-EHL line contacts. *Trans. ASME - Journal of Tribology*, 1991, vol. 113, p. 645-657.

[35] KUMAR, P., KHONSARI, M.M.: On the role of the lubricant rheology and piezo-viscous properties in line and point contact EHL. *Tribology International*, 2009, vol. 42, p. 1522-1530.

[36] BAIR, S., QURESHI, F.: The generalized Newtonian fluid model and elasto-hydrodynamic film thickness. *Trans ASME - Journal of Tribology*, 2003, vol. 125, p. 70-75.

[37] YASUDA, K., ARMSTRONG, R.C., COHEN, R.E.: Shear flow properties of concentrated solutions of linear and star branched polystyrenes. *Rheol Acta*, 1981, vol. 20, p. 163-178.

[38] ROTEM, Z.: Non-Newtonian flow in annuli. *ASME J. Appl. Mech.*, 1962, no. 33, p. 421-424.

[39] IIVONEN, H.T., HAMROCK, B.J.: A non-Newtonian fluid model incorporated into elastohydrodynamic lubrication of rectangular contacts. *Wear*, 1991, vol. 143, p. 297-305.

[40] HSIAO, H.S., HAMROCK, B.J.: A complete solution for thermal - elastohydrodynamic lubrication of line contacts using a circular non-Newtonian fluid model. *Trans. ASME - Journal of Tribology*, 1992, vol. 114, p. 540-552.

[41] SUI, P.C., SADEGHI, F.: Non-Newtonian thermal elastohydrodynamic lubrication. *Trans. ASME - Journal of Tribology*, 1991, vol. 113, p. 390-397.

[42] KIM, K.H., SADEGHI, F.: Non-Newtonian Elastohydrodynamic Lubrication of Point Contact. *Journal of Tribology*, 1991, vol. 113, p. 703-711.

[43] EHRET, P., DOWSON, D. TAYLOR, C.M.: On the lubricant transport conditions in elastohydrodynamic conjunctions. *Proc. Roy. Soc., London, series A*, 1998, vol. 454, p. 763-787.

[44] HOLT, C.A., EVANS, H.P., SNIDLE, R.W.: Solution of the non-Newtonian elastohydrodynamic problem for circular contacts based on a flow continuity method. *Proc. Instn. Mech. Engrs. - Part J*, 1996, vol. 210, p. 247-258.

[45] GREENWOOD, J.A.: Two-dimensional flow of a non-Newtonian lubricant. *Proc. Instn. Mech. Engrs. - Part J*, 2000, vol. 214, p. 29-41.

[46] CHAPKOV, A.: *Etude des Contacts ElastoHydroDyanmiques Lubrifiés avec un Fluide Non-Newtonien.* Ph.D. Thesis, INSA, Lyon, France, 2006.

[47] CHARLES, P., ELFASSI, M., LUBRECHT, A.A.: 'Double-Newtonian' rheological model for the two-dimensional Reynolds equation. *Proc. Instn. Mech. Engrs. - Part J*, 2011, vol. 225, p. 335-346.

[48] BAIR, S., KHONSARI, M.M.: Reynolds equations for common generalized Newtonian models and approximate Reynolds-Carreau equation. *Proc. Instn. Mech. Engrs. - Part J*, 2006, vol. 220, p. 365-374.

[49] DOWSON, D., HIGGINSON, G.R.: A Numerical Solution to the Elastohydrodynamic Problem. *J. of Mech. Eng. Sci.,* 1959, vol. 1, p. 6-15.

[50] CAMERON, A., GOHAR, R.: Theoretical and Experimental Studies of the Oil Film in Lubricated Point Contact. *Proc. R. Soc. London*, 1966, Ser. A, vol. 291, p. 520-536.

[51] WEDEVEN, L.D., EVANS, D., CAMERON, A.: Optical Analysis of Ball Bearing Starvation. *ASME J. Lubr. Technol.,*, 1971, vol. 93, p. 349-363.

[52] CHENG, H.S.: A Numerical Solution of the Elastohydrodynamic Film Thickness in an Elliptical Contact. *ASME J. Lubr. Technol.*, 1970, vol. 92, p. 155-162.

[53] RANGER, A.P., ETTLES, C.M., and CAMERON, A.: The Solution of the Point Contact Elastohydrodynamic Problem. *Proc. R. Soc. London, Ser.A.*, 1974, vol. 346, p. 227-244.

[54] HAMROCK, B.J., DOWSON, D.: Isothermal Elastohydrodynamic Lubrication of Point contacts, part I, Theoretical Formulation. *ASME Journal of Tribology*, 1976, vol. 98, p. 223-228.

[55] HAMROCK, B.J., DOWSON, D.: Isothermal Elastohydrodynamic Lubrication of Point contacts, part III, Fully Flooded Results. *ASME Journal of Tribology*, 1977, vol. 99, p. 264-275.

[56] HOUPERT, L.G. and HAMROCK, B.J.: Fast Approach for Calculating of Film Thicknesses and Pressures in Elastohydrodynamically Lubricated Contacts at High Loads. *J. Tribol.*, 1986, vol.108, no. 3, p. 411-420.

[57] LUBRECHT, A.A., TEN NAPEL, W.E., BOSMA, R.: Multigrid, An Alternative Method for Solution of Two-Dimensional Elastohydrodynamically Lubricated Point Contact Calculations. *ASME J. Tribology*, 1987, vol. 109, p. 437-443.

[58] LUBRECHT, A.A.: *The numerical solution of the elastohydrodynamically lubricated line and point contact problem, using multigrid techniques.* Ph.D. Thesis, University Enschede, The Netherlands, 1987.

[59] MOES, H., BOSMA,R.: Design Charts for Optimum Bearing Configuration I The Full Journal Bearing. *ASME Journal of Tribology*,1971, vol. 93, p. 302-306.

[60] VENNER, C.H., ten NAPEL, W.E.: Multilevel solution of the elastohydrodynamically lubricated circular contact problem. Part I: theory and numerical algorithm. *Wear* 1992, vol. 152, p. 351-367.

[61] VENNER, C.H., ten NAPEL, W.E.: Multilevel solution of the elastohydrodynamically lubricated circular contact problem. Part II: smooth surface results. *Wear* 1992, vol. 152, p. 369-381.

[62] VENNER, C.H., ten NAPEL, W.E.: Numerical calculations of the pressure spike in elastohydrodynamic lubrication. *Lubrication Science*, 1990, vol. 2, p. 321-335.

[63] NIJENBANNING, G., VENNER, C.H., MOES, H.: Film Thickness in Elastohydrodynamically Lubricated Elliptic Contacts. *Wear*, 1994, vol. 176, p. 217-229.

[64] VENNER, C.H., BOS, J.: Effects of lubricant compressibility on the film thickness in EHL line and circular contacts. *Wear*, 1994, vol. 173, p. 151-165.

[65] LEE, H.: *A numerical solution to the elastohydrodynamic problem incorporating a non-Newtonian rheological model.* Ph.D. Thesis, Georgia Institute of Technology, USA, 1991.

[66] JOHNSON, K.L.: Non-Newtonian effects in elastohydrodynamic lubrication. *In Dowson D. et al. Thin Films in Tribology*, 1993, p. 15-26.

[67] TZENG, S.T., SAIBEL, E.: Surface roughness effects on slider bearing lubrication. *ASLE Transactions*, 1967, vol. 10, p. 334–338.

[68] CHRISTENSEN, H.: Stochastic models for hydrodynamic lubrication of rough surfaces. *Proceedings of the Institution of Mechanical Engineers. Part 1*, 1970, vol. 184, p. 1013–1026.

[69] ELROD, H.G.: A general theory for laminar lubrication with Reynolds roughness. *ASME Journal of Tribology*, 1979, vol. 101, p. 104-112.

[70] PATIR, N., CHENG, H.S.: An average flow model for determining effects of three-dimensional roughness on partial hydrodynamic lubrication. *Journal of Lubrication Technology*, 1978, vol. 100, p. 12–17.

[71] PATIR, N., CHENG, H.S.: Effect of surface orientation on the central film thickness in EHD contacts. *In Dowson D. et al. Proceedings of 5th Leeds-Lyon Symposium, Leeds*, 1978, p. 15-21.

[72] MAJUMDAR, B.C., HAMROCK, B.J.: Effect of Surface Roughness on Elastohydrodynamic Line Contact. *Journal of Lubrication Technology*, 1982, vol. 104, p. 401-409.

[73] JENG, Y.R., HAMROCK, B.J.: The effect of surface roughness on elastohydrodynamicallly lubricated point contact. *ASLE Transactions*, 1987, vol. 30, no. 4, p. 531-538.

[74] ZHU, D., CHENG, H.S.: Effect of surface roughness on the point contact EHL. *Transactions of ASME - Journal of Tribology*, 1988, vol. 110, p. 32-37.

[75] SADEGHI, F., SUI, P.C.: Compressible Elastohydrodynamic Lubrication of Rough Surfaces. *Transactions of ASME - Journal of Tribology*, 1989, vol. 111, p. 56-62.

[76] LEE, R.T., Hamrock, B.J.: A circular non-Newtonian fluid model: Part 2 - Used in microelastohydrodynamic lubrication. *Presented at the 1989 ASME/STLE tribology conference, Fort Lauderdale, U.S.A., ASME Preprint 80-Tribology-10*, 1989.

[77] CHANG, L., CUSANO, C., CONRY, T.F.: Effects of lubricant rheology and kinematic conditions on micro-elastohydrodynamic lubrication. *ASME Journal of Tribology*, 1989, vol. 111, p. 344-351.

[78] OH, K.P.: The numerical solution of dynamically loaded elastohydrodynamic contact as a nonlinear complementarity problem. *ASME Journal of Tribology*, 1985, vol. 106, p. 88-95.

[79] AI, X.: *Numerical analysis of elastohydrodynamically lubricated line and point contacts with rough surfaces by using semi-system and multigrid methods. (Volumes I and II).* Ph.D. Thesis, Northwestern University, Evanston, Illionis, USA, 1993.

[80] AI, X., CHENG, H.S.: The influence of moving dent on point EHL contacts. *Tribology Transactions*, 1994, vol. 37, no. 2, p. 323-335.

[81] VENNER, C.H., LUBRECHT, A.A.: Numerical simulation of a transverse ridge in a circular EHL contact under rolling/sliding. *Journal of Tribology - Transactions of the ASME*. 1994, vol. 116, no. 4, p. 751-761.

[82] VENNER, C.H., LUBRECHT, A.A.: Numerical simulation of a waviness in a circular EHL contact, under rolling/sliding. *Tribology Series*, 1995, vol. 30, p. 259-272.

[83] VENNER, C.H., LUBRECHT, A.A.: Numerical Analysis of the Influence of the Waviness in the Film Thickness of a Circular EHL Contact. *Journal of Tribology - Transactions of the ASME*, 1996, vol. 118, no. 1, p. 153-161.

[84] EHRET, P., DOWSON, D., TAYLOR, C.M.: Time-dependent solutions with waviness and asperities in EHL point contacts. *Tribology Series*, 1997, vol. 32, p. 313-324.

[85] GREENWOOD, J.A., MORALES-ESPEJEL, G.E.: The behaviour of transverse roughness in EHL contacts. *Proceedings of the Institution of Mechanical Engineers Part J - Journal of Engineering Tribology*, 1994, vol. 208, p. 121-132.

[86] LUBRECHT, A.A.: Influence of local and global features in EHL contacts. *In Dowson D. et al. Elastohydrodynamics '96, Tribological Series*, 1997, vol. 32, p. 17-25.

[87] KANETA, M.: Effects of Surface Roughness in Elastohydrodynamic Lubrication. *JSME International Journal*, 1992, vol. 35, no. 4, p. 535-546.

[88] LUBRECHT, A.A., VENNER, C.H.: Elastohydrodynamic lubrication of rough surfaces. *Proceedings of the Institution of Mechanical Engineers Part J - Journal of Engineering Tribology*, 1999, vol. 213, no. J5., p. 397-404.

[89] VENNER, C.H., COUHIER, F., LUBRECHT, A.A., GREENWOOD, J.A.: Amplitude Reduction of Waviness in Transient EHL Line Contacts. *Tribology Series*, 1997, vol. 32, p. 103-112. ¨

[90] VENNER, C.H., LUBRECHT, A.A.: Amplitude reduction of non-isotropic harmonic patterns in circular EHL contacts, under pure rolling. *Lubrication at the Frontier: The Role of the Interface and Surface Layers in the Thin Film and Boundary Regime*, in: Tribology Series, 1999, vol. 36, p. 151-162.

[91] VENNER, C.H., LUBRECHT, A.A.: An engineering tool for the quantitative prediction of general roughness deformation in EHL contacts based on harmonic waviness attenuation. *Proceedings of the Institution of Mechanical Engineers Part J-Journal of Engineering Tribology*, 2005, vol. 219, no. J5, p. 303-312.

[92] HOOKE, C.J., VENNER, C.H.: Surface roughness attenuation in line and point contacts. *Proceedings of the Institution of Mechanical Engineers Part J-Journal of Engineering Tribology*, 2000, vol. 214, no. J5, p. 439-444.

[93] JACOD, B., LUGT, P.M., TRIPP, J.H., VENNER, C.H.: Amplitude reduction of waviness in elastohydrodynamic lubrication using an Eyring fluid model. *Proceedings of the Institution of Mechanical Engineers Part J - Journal of Engineering Tribology*, 2000, vol. 214, no. J4, p. 343-350.

[94] CHAPKOV, A.D., VENNER, C.H., LUBRECHT, A.A.: Roughness amplitude reduction under non-Newtonian EHD lubrication conditions. *Journal of Tribology-Transactions of the ASME*, 2006, vol. 128, no. 4, p. 753-760.

[95] HOOKE, C.J.: The effects of roughness in EHL contacts. *Tribology and Interface Engineering Series. Elsevier*, 2005, vol. 48, p. 31-46.

[96] HOOKE, C.J.: The behaviour of low-amplitude surface roughness under line contacts: non-Newtonian fluids. *Proceedings of the Institution of Mechanical Engineers Part J - Journal of Engineering Tribology*, 2000, vol. 214, no. J3, p. 253-265.

[97] HOOKE, C.J.: Engineering analysis of the rough elastohydrodynamically lubricated contacts. *Proceedings of the Institution of Mechanical Engineers, Part J: Journal of Engineering Tribology*, 2009, vol. 223, no. 3, p. 517-528.

[98] HU, Y.Z., ZHU, D.: A Full Numerical Solution to the Mixed Lubrication in Point C Contacts. *Journal of Tribology - Transactions of the ASME*, 2000, vol. 122, p. 1–9.

[99] FELIX-QUINONEZ, A. ,EHRET, P., SUMMERS, J. L.: Numerical analysis of experimental observations of a single transverse ridge passing through an elastohydrodynamic lubrication point contact under rolling/sliding conditions. *Proceedings of the Institution of Mechanical Engineers Part J-Journal of Engineering Tribology*, 2004, vol. 218, no. J2, p. 109-123.

[100] GREENWOOD, J.A.: Transverse roughness in elastohydrodynamic lubrication. *Proceedings of the Institution of Mechanical Engineers Part J-Journal of Engineering Tribology*, 1999, vol. 213, p. 383-396.

[101] WANG, J., et al.: Occurrence of microelastohydrodynamic lubrication in simple sliding motion with transverse roughness. *Proceedings of the Institution of Mechanical Engineers, Part J: Journal of Engineering Tribology*, 2006, vol. 220, no. 3, p. 273-285.

[102] LIU, Y. et al.: Effects of differential scheme and viscosity model on rough-surface point-contact isothermal EHL. *Journal of Tribology*, 2009, vol. 131, no. 4, 044501.

[103] ERTEL, A.M.: Hydrodynamic lubrication based on new principles. *Akad. Nauk SSSR Prikadnaya Mathematica i Mekhanika,* 1939, vol. 3, no.2, p.41-52.

[104] EVANS, H.P., SNIDLE, R.W.: Inverse solution of Reynolds' equation of lubrication under point-contact elastohydrodynamic conditions. *ASME J. of Tribology*, 1981, vol. 103, p. 539-546.

[105] CHITTENDEN, R.J., DOWSON, D., DUNN, J.F., TAYLOR, C.M.: Theoretical Analysis of the Isothermal Elastohydrodyunamic Lubrication of Concentrated Contacts: Part II. *Proc. R. Soc. London, Ser.A*, 1985, vol. 397, p. 245-269.

[106] HAMROCK, B.J., JACOBSON, B.O.: Elastohydrodynamic lubrication of line contacts. *ASLE transactions*, 1984, vol. 27, no. 4, p. 275-287.

[107] OKAMURA, H.: A contribution to the numerical analysis of isothermal elastohydrodynamic lubrication. *Proc. 9th Leeds-Lyon Symp. on Tribology, Leeds*, 1982, p. 313-320.

[108] BRANDT, A., LIVNE, O.E.: *Multigrid Techniques: 1984 Guide with applications to fluid dynamics.* SIAM, 2011.

[109] BRANDT, A., and LUBRECHT, A.A.: Multilevel Matrix Multiplication and Fast Solution of Integral Equations. *J. of Comp. Phys.,*, 1990, 90, 2, p. 348-370.

[110] BRIGGS, W.L.: *A Multigrid Tutorial.* 1987, SIAM, Philadelphia, Pennsylvania, ISBN 0-89871-221-1.

[111] WESSELING, P.: *An introduction to multigrid methods*. 1991, John Wiley & Sons, New York. ISBN: 0-471-930830.

[112] PICCIGALLO, B.: A fast method for the numerical solution of thermal-elastohydrodynamic lubrication problems. *Wear*, 1996, vol.193, p. 56-65.

[113] LU, H., BERZINS, M., GOODYER, C.E., JIMACK, P.K.: High-order discontinuous Galerkin method for elastohydrodynamic lubrication line contact problems. *Communications in numerical methods in engineering*, 2005, vol. 21, p. 643–650.

[114] FATU, A., HAJJAM, M., BONNEAU, D.: A New Model of Thermoelastohydrodynamic Lubrication in Dynamically Loaded Journal Bearings. *Journal of Tribology Transactions of ASME*, 2006, vol. 128, p. 85-95.

[115] HAJJAM, M., Bonneau, D.: A transient finite element cavitation algorithm with application to radial lip seals. *Tribology International*, 2007, vol. 40, p. 1258–1269.

[116] HABCHI, W., DEMIRCI, I., EYHERAMENDY, D., MORALES-ESPEJEL, G., VERGNE, P.: A finite element approach of thin film lubrication in circular EHD contacts. *Tribology International,* 2007, vol. 40, p. 1466–1473.

[117] HABCHI, W., EYHERAMENDY, D., VERGNE, P., MORALES-ESPEJEL, G.: A Full-System Approach of the Elastohydrodynamic Line/Point Contact Problem. *Journal of Tribology,* 2008, vol.130.

[118] SCHMIDT, T., ANDRÉ, M., POLL, G.: A transient 2D-finite-element approach for the simulation of mixed lubrication effects of reciprocating hydraulic rod seals. *Tribology International*, 2010, vol. 43, p. 1775–1785.

[119] PATANKAR, S. V., *Numerical Heat Transfer and Fluid Flow.* Hemisphere Publishing, Washington, 1980.

[120] ČERMÁK, J.: A non-symmetric discretization formula for the numerical solution of elasto-hydrodynamic lubrication circular contact problem. *Tribology International,* 1998, vol. 31, No. 12, p. 761–765.

[121] LU, C.J., CHIOU, S.S.: On the interface diffusion coefficient for solving Reynolds equation by control volume method. *Tribology International*, 2003, vol. 36, p. 929–933.

[122] ALMQVIST, T.; LARSSON, R. : The Navier-Stokes approach for thermal EHL line contact solutions. *Tribology International*, 2002, vol. 35, p. 163-170.

[123] ALMQVIST, T., ALMQVIST, A., LARSSON, R. : A comparison between computational fluid dynamic and Reynolds approaches for simulating transient EHL line contacts. *Tribology International*, 2004, vol. 37, p. 61–69.

[124] HARTINGER, M., DUMONT, M.L., IOANNIDES, S., GOSMAN, S., SPIKES, H.: CFD Modeling of a Thermal and Shear - Thinning Elastohydrodynamic Line Contact. *Journal of Tribology*, 2008, vol.130, 041503.

[125] POLONSKY, I.A., KEER, L.M.: A numerical method for solving rough contact problems based on the multi-level multi-summation and conjugate gradient techniques. *Wear*, 1999, vol. 231, p. 206–219.

[126] HU, Y.Z., BARBER, G.C., ZHU, D.: Numerical Analysis for the Elastic Contact of Real Rough Surfaces. *Tribology Transactions*, 1999, vol. 42, no. 3, p. 443–452.

[127] COLIN, F., LUBRECHT, A.A.: Comparison of FFT-MLMI for Elastic Deformation Calculations. *Journal of Tribology - Transactions of the ASME*, 2001, vol. 123, p. 884–887.

[128] POLONSKY, I.A., KEER, L.M.: Fast Methods for Solving Rough Contact Problems: A Comparative Study. *Journal of Tribology - Transactions of the ASME*, 2000, vol. 122, p. 36-41.

[129] POLONSKY, I.A., KEER, L.M.: A Fast and Accurate Method for Numerical Analysis of Elastic Layered Contacts. *Journal of Tribology - Transactions of ASME*, 2000, vol. 122, p. 30–35.

[130] HU, Y.Z., BARBER, G.C., ZHU, D., AI, X.: A study on an FFT-based approach for fast estimation of pressure distribution in point EHL contacts of rough surfaces. *Tribology Transactions*, 2001, vol. 44, no. 1, p. 59–69.

[131] LIU, Y., CHEN, W.W., ZHU, D., LIU, S., WANG, Q.J.: An elastohydrodynamic lubrication model for coated surfaces in point contacts. *Journal of Tribology - Transactions of the ASME*, 2007, vol. 129, p. 509–516.

[132] RICHE, I., VILLECHAISE, B.: Use of the FFT to Determine the Subsurface Stresses Locally in Multilayered Elastic Solids Caused by a TEHL Loading. *Journal of Tribology - Transactions of the ASME*, 2006, vol. 128, p. 59–66.

[133] CHOO, Y.J., KOO, Y.P., KIM, T.W.: A new FFT technique for the analysis of contact pressure and subsurface stress in a semi-infinite solid. *KSME International Journal*, 2000, vol. 14, no. 3, p. 331–337.

[134] HOLMES, M.J.A., EVANS, H.P., HUGHES, T. G., SNIDLE, R.W.: Transient elastohydrodynamic point contact analysis using a new coupled differential deflection method, Part 1: theory and validation. *Proceedings of the Institution of Mechanical Engineers, Part J: Journal of Engineering Tribology*, 2003, vol. 217, p. 289-303.

[135] HOLMES, M.J.A., EVANS, H.P., HUGHES, T. G., SNIDLE, R.W.: Transient elastohydrodynamic point contact analysis using a new coupled differential deflection method, Part 2: results. *Proceedings of the Institution of Mechanical Engineers, Part J: Journal of Engineering Tribology*, 2003, vol. 217, p. 305–321.

[136] URBANEC, L.: *Numerická simulace elastohydrodynamicky mazaného kruhového kontaktu nehladkých povrchů.* Ph.D. Thesis, Brno: Vysoké učení technické v Brně, Fakulta strojního inženýrství, 2007. p. 81.

[137] VENNER, C. H. EHL film thickness computations at low speeds: risk of artificial trends as a result of poor accuracy and implications for mixed lubrication modelling. *Proceedings of the Institution of Mechanical Engineers, Part J: Journal of Engineering Tribology*, 2005, vol. 219, no. 4, p. 285-290.

[138] VENNER, C. H.; MORALES-ESPEJEL, G. E.: Amplitude reduction of small-amplitude waviness in transient elastohydrodynamically lubricated line contacts. *Proceedings of the Institution of Mechanical Engineers, Part J: Journal of Engineering Tribology*, 1999, vol. 213, no. 6, p. 487-504.

[139] GOODYER, C.H.: *Adaptive Numerical Methods for Elastohydrodynamic Lubrication.* Ph.D. Thesis, Leeds: The University of Leeds, School of Computing, 2001. p. 179.

[140] ŠPERKA, P.: *In-situ studium zmeny topografie trecích povrchu v elastohydrodynamickém kontaktu.* Ph.D. Thesis, Brno: Vysoké učení technické v Brně, Fakulta strojního inženýrství, 2011. p. 143.

LIST OF FIGURES

LIST OF TABLES

LIST OF SYMBOLS, PHYSICAL CONSTANTS AND ABBREVIATIONS

a	Hertzian radius (m)
A	amplitude of roughness (m)
A_d	deformed amplitude of the roughness
A_i	initial amplitude of the roughness
A^j	matrix of coefficients for line j
b	contact width (m)
C	value representing the effect of compressibility
E_r	Young's modulus of elasticity (GPa)
E'	ecvivalent modulus of elasticity (GPa)
ERR	difference norm
f	right hand side vector
F	force field
G	shear modulus (Pa)
G	dimensionless parameter of material
G_1	
G_2	integration variables
G_3	
h	film thickness (µm)
h	mesh size
H	coarse mesh size
H	dimensionless film thickness
H_{min}	dimensionless minimum film thickness
H_c	dimensionless central film thickness
h_c	central film thickness (m)
H_c^M	dimensionless Moes central film thickness
h_{min}	minimum film thickness (m)

h_T	time step
H_d	height of the flat-top ridge
H_X	discrete wedge term
H_T	discrete squeeze term
h_0	mutual approach
H_0	dimensionless mutual approach
i	index
I_h^H	restriction operator
I_H^h	interpolation operator
j	index
k	ellipticity ratio
K	kernel
k	level
K^{hh}	discrete kernel
L	dimensionless Moes parameter of material
L	inlet pressure sweep
$\mathcal{L}$	continuous differential operator
M	dimensionless Moes parameter of load
M_1	1-D Moes parameter of load
M_2	2-D Moes parameter of load
n	normal vector
n	index
N	index
n_x	number of grid points in x direction
n_y	number of grid points in y direction
p	pressure (Pa)
P	dimensionless pressure
P	Greenwood's parameter of pressure

p_0	constant
p_h	Hertzian pressure (Pa)
q	constant
Q_X	discrete Poiseuille term in X direction
Q_Y	discrete Poiseuille term in Y direction
Q	attenuation parameter
r	wavelength ratio
$\mathcal{R}$	roughness function
R_{x1}	radius of curvature of body 1 in x direction (m)
R_{x2}	radius of curvature of body 2 in x direction (m)
R_{y1}	radius of curvature of body 1 in y direction (m)
R_{y2}	radius of curvature of body 2 in y direction (m)
R_x	reduced radius of curvature in x direction (m)
R_y	reduced radius of curvature in y direction(m)
r	vector of residuals
S	surface
S	slide to roll ratio
S	Greenwood's parameter of speed
SRR	slide to roll ratio
t	time (s)
T	dimensionless time
U	velocity vector
u	velocity in x direction
U	dimensionless parameter of speed
u_m	mean velocity (m/s)
u_1	velocity of surface 1 in x direction
u_2	velocity of surface 2 in x direction
u	unknown vector

v	velocity in y direction
v	vector of numerical error
v_1	velocity of surface 1 in y direction
v_2	velocity of surface 2 in y direction
V	volume
w	velocity in z direction
w	load (N)
W	dimensionless parameter of load
W	wavelength (m)
W_1	base width of the flat-top ridge (m)
W_2	top width of the flat-top ridge (m)
WU	working unit
x	coordinate
X	dimensionless coordinate
x_a	boundary condition in x direction
x_b	boundary condition in x direction
x_d	position of the ridge (m)
X_a	dimensionless boundary condition in x direction
X_b	dimensionless boundary condition in x direction
X_d	position of the ridge
y	coordinate
Y	dimensionless coordinate
y_a	boundary condition in y direction
y_b	boundary condition in y direction
Y_a	dimensionless boundary condition in y direction
Y_b	dimensionless boundary condition in y direction
z	coordinate
z	coefficient

Greek symbols

α	pressure viscosity coefficient (Pa^{-1})
γ	shear stress porportionality coefficient
$\dot{\gamma}$	shear rate
$\underline{\delta}_j^h$	vector of changes of line j
δr	low amplitude roughness
δP	pressure perturbation
δw	deformation
δh	residual roughness
δ	deformation (m)
δh_c	decay of the complementary wave
η	viscosity (Pa s)
η_0	viscosity at ambient pressure (Pa s)
$\bar{\eta}_0$	dimensionless viscosity
η_x	effective viscosity
η_y	effective viscosity
λ	wavelength
λ_x	wavelength in the x direction
λ_y	wavelenght in the y direction
$\bar{\lambda}$	coefficient
μ	friction coefficient
μ_1	viscosity at low shear rate
μ_2	second Newtonian viscosity
ν	Poisson's ratio
ξ_X	variable
ξ_Y	variable
ρ	density ($\mathrm{kg/m}^3$)
$\bar{\rho}$	dimensionless density

ρ_0	atmospheric density
τ_x	shear stress in x direction (Pa)
τ_y	shear stress in y direction (Pa)
τ_e	mean shear stress (Pa)
τ	shear stress (Pa)
$\bar{\tau}_m$	dimensionless mean shear stress
τ_0	Eyring shear stess (Pa)
τ_L	limiting shear stress (Pa)
τ_{L0}	constant (Pa)
Ω	domain
ω_{gs}	Gauss-Seidel relaxation factor
ω_{ja}	Jacobi relaxation factor
ω_{H_0}	force balance equation's relaxation factor
∇_i	dimensionless parameter defining the effects of operating conditions, $i = 1, 2$

Abbreviations

CFD	computational fluid dynamics
CGCC	coarse grid correction cycle
EHL	elastohydrodynamics
FFT	fast Fourier transform
FMG	full multigrid
G-S	Gauss-Seidel iteration method
MG	multigrid
FEM	finite element method
FVM	finite volume method
MLMI	multi-level multi-integration
N-R	Newton-Raphson method
N-S	Navier-Stokes equations